Long Term Evolution of Neptune's Atmosphere

MSc Thesis

Andrea Zorzi

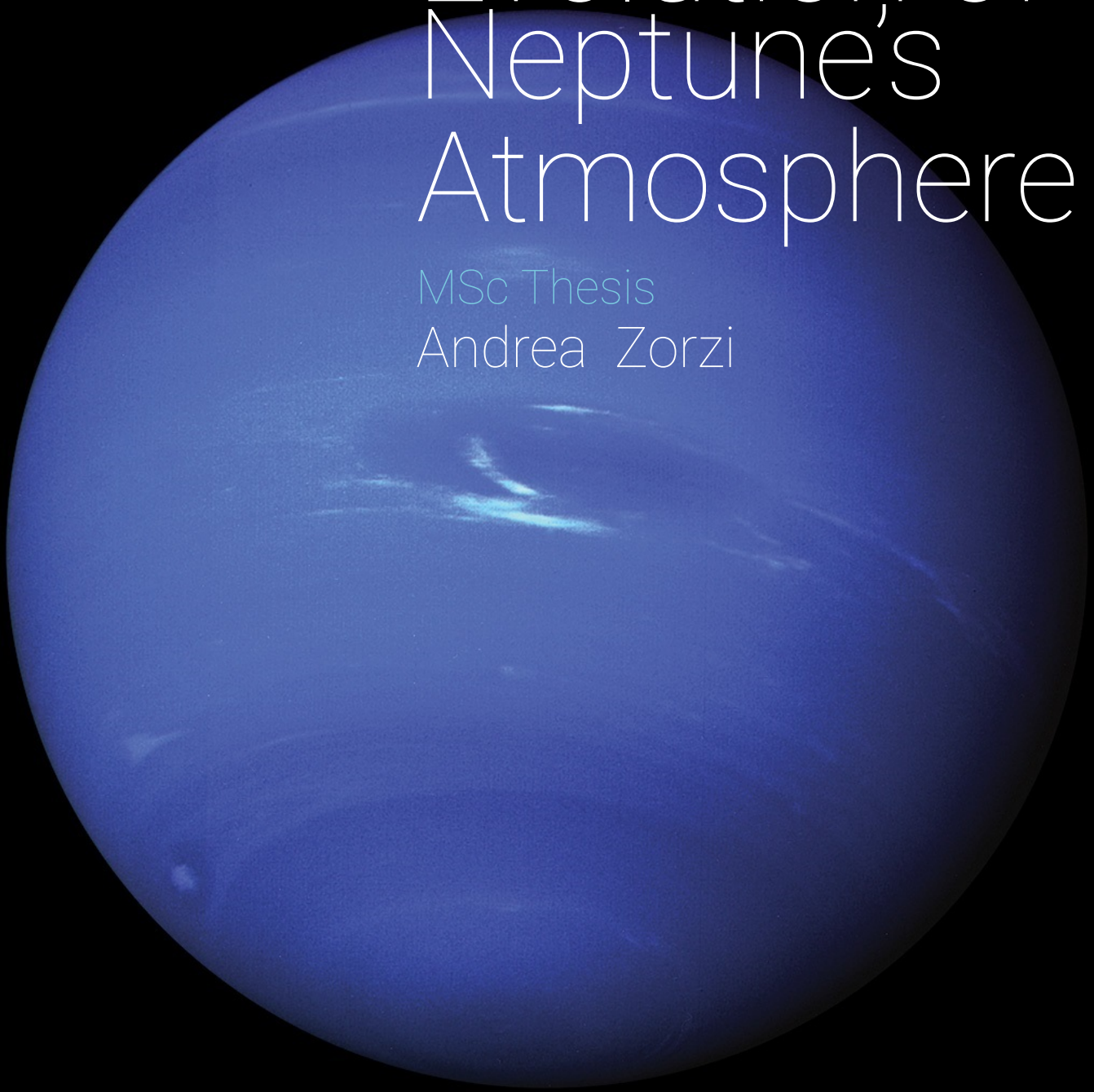

Aerospace Engineering Department

TU Delft Delft University of Technology

Front cover image: Neptune imaged by *Voyager 2* in 1989. Credit: NASA/JPL.

Long Term Evolution of Neptune's Atmosphere

MSc Thesis

by

Andrea Zorzi

to obtain the degree of Master of Science
at the Delft University of Technology,
to be defended publicly on Monday September 23, 2019 at 14.00.

Student number:	4749898	
Project duration:	December 3, 2018 – September 5, 2019	
Thesis committee:	Prof. dr. ir. L. L. A. Vermeersen,	TU Delft, chair
	Prof. dr. I. de Pater,	TU Delft, supervisor
	Dr. D. M. Stam,	TU Delft
	Dr. J. P. Veefkind,	TU Delft

An electronic version of this thesis is available at `http://repository.tudelft.nl/`.

TU Delft

Preface

When I first started working on my MSc thesis, I was convinced of the fact that this would have been one of the most important end points for my studies, as well as for my life. After having spent years to study science other people had produced, I was called to be the main actor, to explore topics few people worked on and to find something new, effectively producing science myself. In finishing to write this work, I felt an opposite sensation. Rather than an ending, I see this as a new starting point.

Working on my thesis brought me to live a real adventure. It allowed me to move to one of the top university in the world for life sciences, UC Berkeley, to join an elite group of Astronomy and Planetary Sciences students supervised by the smartest professors in the field. My six months in California will be one of the best memories of my academic path.

Not only this was a great experience, that allowed me to make connections with other students and see how the world is on the opposite side from home, but it gave me something more valuable. It shed light on my interests and future plans. It gave me the possibility to discover the beauty of doing research, to know the intriguing world of planetary sciences, and definitely convinced me to extend my academic path, eager to give my contribution to human knowledge about our solar system.

I first want to thank the person who made all of this possible, Imke. The trust she put on a MSc student she saw for just two weeks is something I will never forget. She was the one in the first place to believe in me. I feel gifted to have worked under the supervision of such a fantastic woman, not only professionally speaking, but also as a wonderful person, always available when help is needed, kindly open to critics and different proposals. Her character played a key role in making my work the most enjoyable.

Many thanks also to who can be effectively considered a second mentor, Ned. The help he gave me was tremendous. His critical thinking made me reflect upon what I was assigned to, and he always showed interest in my progress, spurring me in the moments of difficulty and giving credit to every step ahead I was making. A strong moral support came from Chris, former student at TU Delft, now graduate student in Cal, as he already made the path I have been following. He gave me invaluable advice for my decisions and future.

I have to thank also the whole Planetary Sciences group in Cal: Josh, Charles, Erin, Mike, Statia. A terrific help and support came from Daphne, who provided precious availability and crucial comments to improve the quality of the work.

All this would not have been possible without the incredible support from the people I left to move to the Netherlands and U.S., starting from my parents and my brothers, my whole family, as well as my dearest *Incapriati* friends and university mates.

Andrea Zorzi
Delft, September 2019

Contents

Nomenclature

α	Referred to upper haze layer	[-]
α_ν	Absorption coefficient	[m^{-1}]
β	Referred to lower haze layer	[-]
χ^2	Reduced χ^2 test value	[-]
δ	Depolarization factor	[-]
δ_φ	I/F threshold for cloud removal at latitude φ	[-]
κ_ν	Mass absorption coefficient	[m^2 kg^{-1}]
λ	Wavelength	[μm]
λ_{eff}	Filter effective wavelength	[μm]
λ_{peak}	Filter peak wavelength	[μm]
μ	Cosine of emission angle	[-]
μ_0	Cosine of incidence angle	[-]
μ_a	Mean molecular mass	[amu]
ν	Frequency	[Hz]
Ω	Solid angle	[sr]
ω	Single scattering albedo	[-]
ω_0	Single scattering albedo in near infrared	[-]
ω_1	Single scattering albedo's spectral slope towards ultraviolet	[-]
Φ	Double Henyey-Greenstein phase function	[-]
ρ	Mass density	[kg m^{-3}]
σ	Cross section	[m^2]
σ_ν	Scattering coefficient	[m^{-1}]
σ_n	Total error on reflectivity annual mean	[-]
σ_s	Standard deviation	[-]
σ_{obs}	Observation uncertainty	[-]
σ_{phot}	Photometric uncertainty	[-]
τ	Optical depth	[-]
Θ	Scattering angle	[rad]
θ	Phase angle	[rad]
$\underline{n}$	Complex refractive index	[-]

φ	Latitude	[deg]
ϑ	Emission angle	[rad]
A	Area	[m^2]
b	Exponent of number density distribution	[-]
B_ν	Brightness	[W m^{-2} Hz^{-1} sr^{-1}]
E	Energy	[J]
f	Henyey-Greenstein forward scattering fraction	[-]
F_ν	Flux density	[W m^{-2} μm^{-1}]
$F_\odot$	Solar flux density at Earth's distance	[erg s^{-1} cm^{-2} μm^{-1}]
F_N	Neptune's flux density	[erg s^{-1} cm^{-2} μm^{-1}]
$f_0(\nu)$	Non-Raman scattered photons fraction	[-]
$f_{\Delta_\nu}(\nu)$	Photons fraction subject to transition $\Delta\nu$	[-]
g	Gravitational acceleration	[cm s^{-2}]
g_1, g_2	Henyey-Greenstein back-scattering factors	[-]
H	Pressure scale height	[cm]
h_{frac}	Fractional scale height	[-]
I_ν	Specific intensity	[W m^{-2} s^{-1} sr^{-1} Hz^{-1}]
j_ν	Monochromatic volume emission coefficient	[W m^{-3} sr^{-1} Hz^{-1}]
k	Empirical exponent for Minnaert correction function	[-]
l	Pressure resolution logarithmic factor	[-]
m	Number of fitted parameters	[-]
$m_\odot$	Sun magnitude	[mag]
m_i	Imaginary part of refractive index	[-]
m_N	Neptune's magnitude	[mag]
m_{amu}	Mass of atomic unit	[g]
N	Number density	[cm^{-3}]
n	Number of observations on same year	[-]
$n(r)$	Number density of particles with radius r	[-]
n_i	Real refractive index	[-]
P	Pressure	[bar]
p	Probabilities for reduced χ^2 test	[-]
$p(\cos\Theta)$	Phase function	[-]
P_{max}	Pressure level of haze's base	[bar]
r	Heliocentric distance of the planet	[AU]

r_i	Residual between observed and expected I/F value	[-]
r_p	Particle size distribution peak radius	[μm]
r_{eq}	Neptune's equatorial radius	[km]
r_{pol}	Neptune's polar radius	[km]
s	Distance travelled by light	[m]
T	Temperature	[K]
t	Transmission	[-]
V	Volume	[m^3]
X	Volume mixing ratio	[-]
$X_{CH_{4,s}}$	Stratospheric methane mixing ratio	[-]
$X_{CH_{4,t}}$	Tropospheric methane mixing ratio	[-]
z	Discrete atmospheric layer thickness	[cm]
n	Surface normal unit vector	[-]
s	Line of sight direction	[-]
col	Column abundance	[km-am]
den	Number density	[am]
I/F	Reflectivity	[-]
I/F_{conv}	Filter convolved reflectivity	[-]
I/F_{corr}	Minnaert-corrected reflectivity	[-]
MF	Molar fraction	[-]
Q_{ext}	Mie extinction efficiency	[-]

Acronyms

ALMA Atacama Large Millimeter Array.

CCD Charge Coupled Device.

DISORT DIScrete ORdinate Radiative Transfer.

DN Data Number.

HLSP High-Level Science Product.

HST Hubble Space Telescope.

LTE Local Thermodynamical Equilibrium.

LWS Long Wavelength Spectrometer.

MAST Milkuski Archive for Space Telescopes.

MT Moving Target.

NGDS-32 Northern Great Dark Spot at 32°.

PC1 Planetary Camera 1.

PPS PhotoPolarimeter Subsystem.

RMS Root Mean Square.

RT Radiative Transfer.

SDS-15 Southern Dark Spot in 2015.

STIS Space Telescope Imaging Spectrograph.

STScI Space Telescope Science Institute.

SUNBEAR Spectra from Ultraviolet to Near-infrared with the BErkeley Atmospheric Retrieval.

TP Temperature-Pressure.

UT Universal Time.

WCS World Coordinate System.

WFC3 Wide Field Camera 3.

WFPC2 Wide Field and Planetary Camera 2.

List of Figures

List of Tables

Abstract

We present an analysis of the temporal evolution of hazes on Neptune between 1994 and 2018, using HST archival data at visible wavelengths from the WFPC2 and WFC3 cameras. We assess the changes over time of the global reflectivity in the F850LP/F845M (methane) and F467M (blue) filters, adding more than 10 years of data to previous analyses. We see an increase in brightness in the methane filter from at least 1996 until 2009, followed by a decrease until today, as seen from cloud-free regions only. A similar behavior is observed in the blue filter, which reaches a maximum disk-averaged I/F value in 2002 and stays nearly constant until 2015, when the planet starts to darken. We also evaluate variations in individual latitudinal bands between 90°S and 50°N. We note the largest increases for southern mid-latitudes (65°S-30°S) for both filters, and the northernmost band (20°N-50°N) for the methane filter. The largest decreases are seen in the northernmost band for the blue filter and for southern near-polar (90°S-65°S) and mid- to low latitudes (50°S-5°N) in the methane filter.

We perform radiative transfer modeling to assess the latitudinal variability in the hazes altitudes and to identify changes in the atmospheric vertical structure that may give rise to the observed trends. Adopting the SUNBEAR code and assuming a two-haze-layer model, we find an optically thin ($\tau_\alpha = 0.03$) upper haze layer placed around 0.6 bar and an optically thicker ($\tau_\beta = 2.2$) lower cloud based at 4.1 bar. This model describes the observed I/F values of the atmosphere in 2009 as well as for 2015 for latitudes north of 30°S, but does not agree with southern latitudes, where the best fitting model demands a shallower pressure base (3.4 bar) and methane depletion (methane mixing ratio lowered from 0.05 to 0.03) for the lower haze. The parameters retrieved for 2002 hint at a higher altitude (2.6-3.0 bar) lower haze layer compared to both 2009 and 1996, with the largest difference occurring in relatively cloud-free latitudes (65°S-50°S and 30°S-5°N). The upheaval of the lower haze might be related to the strong cloud activity seen in 2002. Today, southern latitudes' lower hazes have descended to deeper pressure levels (3.6-4.1 bar) with respect to 2009, and different scattering properties are seen for them at southern mid-latitudes and northern regions.

1 Introduction

For more than a century after its discovery in 1846, Neptune had been characterized from ground-based observations as a "featureless green disk" (Newburn and Gulkis, 1973). The technical difficulties posed by the distance of the planet with respect to Earth, having an orbital semi-major axis of 30 AU (de Pater and Lissauer, 2011), prevented the scientific community to have a clear picture of the phenomena taking place in its atmosphere. Indeed, infrared ground-based observations were not able to resolve the latitudinal structure of the planet nor the presence of dark regions (Hammel et al., 1989b). A terrific improvement in our knowledge was provided by Voyager 2, who did a flyby of Neptune in 1989 and returned images spanning 7 months at a unprecedented closeness from the target (Smith et al., 1989). The spacecraft revealed the presence of structures never observed before, such as dark spots, bright features and clouds. The subsequent launch of the Hubble Space Telescope (HST) allowed for a timely monitoring of the planet in the visible spectrum between 1994 and 2018, enabled by the Wide Field and Planetary Camera 2 (WFPC2) and its follow-on Wide Field Camera 3 (WFC3), currently active since mid-2009 (Dressel, 2019).

Many open questions about the atmospheric activity, such as the appearance of dark vortices and bright clouds we have been recording on the planet, are still unresolved, notwithstanding the improvements in space instrumentation that allowed humankind to study Neptune with remote sensing from Earth. Among these open problems, little is known about Neptune's hazes. Hazes are aerosol layers present in the atmosphere, made of gas particles and droplets of various chemical species. Their vertical location and optical properties determine the amount of sunlight they reflect, absorb and transmit to deeper atmospheric pressures. Looking at the amount of sunlight they reflect in a certain wavelength range can constrain their physical properties and the atmospheric vertical structure. The majority of studies were focused on the showy atmospheric structures, such as bright clouds and dark spots, but few authors (e.g. Karkoschka, 2011; Luszcz-Cook et al., 2016) focused on dark regions, where hazes do not cover or are not covered by brighter features such as clouds and can be analyzed.

Filters sensitive to visible wavelengths, i.e. between 0.3 and 1.0 μm, are suitable to probe the deeper ($\sim$ 4 bar) atmospheric layers (Sromovsky and Fry, 2003), where hazes are thought to be located (Karkoschka and Tomasko, 2011; Luszcz-Cook et al., 2016), and record temporal variation of the haze's brightness. A complete characterization of hazes is yet to be done. Indeed, given the long orbital period (approximately 165 terrestrial years, de Pater and Lissauer, 2011), the long-term variability is poorly constrained, especially related to the seasonal variations affecting the planet. Photometric disk-averaged measurements have been taken since 1950 with the 21-inch Lowell observatory telescope and reported by Lockwood (2019), spanning nearly 65 years of the planet's orbital period around the Sun and providing the mean behavior of the Neptune's brightness. Karkoschka (2011) analyzed the haze variations over time from disk-resolved WFPC2 images between 1994 and 2008. Dark regions were observed to brighten according to a pattern modeled with an exponential decay with a 5 year time constant.

The variation in hazes' reflectivity might be caused by changes in the vertical distribution of these layers. The structure of Neptune's atmospheric hazes is still debated. Its characterization led to two models currently proposed. Karkoschka and Tomasko (2011) reports a single stratospheric optically thin layer, above the tropopause (0.13 bar), and a semi-infinite optically thicker haze below the 1.4 bar layer, deduced from observations made with HST's Space Telescope Imaging Spectrograph (STIS). An alternative structure was sug-

gested by Luszcz-Cook et al. (2016), who favored the presence of an optically thick layer at ~ 3 bar, overlain by a second haze layer spanning from 0.59 bar to the stratosphere. The two models might be complementary, as the wavelengths inspected by the two papers (0.3-1.0 μm and 1.47-2.38 μm, respectively) probe different pressure levels, and are sensitive to different-sized particles. In addition, Luszcz-Cook et al. (2016) focused on a near equatorial band (2°N-12°N), whereas Karkoschka and Tomasko (2011) description refers to the whole planetary disk.

The objectives of this work are two-fold. First, we aim to assess the long-term behavior of hazes by analyzing the variations over time of reflected sunlight in the visible spectrum. Our work adds more than 10 years of observations with respect to previous analyses (Karkoschka, 2011), aiming to provide a more complete picture of the hazes' long-term evolution. We also analyze the brightness trend in individual latitudinal bands. Second, we analyze the hazes vertical structure using radiative transfer modeling; this analysis yields possible physical explanations for the observed brightness changes. Chapter 2 formulates the research questions of this work, deduced from the gaps pointed out in summarizing previous relevant literature on Neptune's hazes. Chapter 3 reports the methodology used to collect, navigate and reduce data, in order to obtain measurements in terms of reflectivity. The temporal analysis of reflectivity is done for disk-averaged measurements (Chapter 4) and for individual latitudinal dark regions photometry (Chapter 5). An introduction to the basic definitions of radiative transfer theory and how these concepts are implemented in the employed radiative transfer code are presented in Chapter 6. Subsequently, radiative transfer modeling is performed to match Neptune's vertical structure with multi-wavelength reflectivity data (Chapter 7), followed by a comparison with previous literature for temporal behavior and location of hazes (Chapter 8). Finally, Chapter 9 summarizes our findings and provides recommendations for future works on the matter.

2

Problem statement

This Chapter is dedicated to the formulation of the problem. Hazes (hereafter equivalently referred to as aerosols) of Neptune have been subject to study after Voyager 2 flyby of the planet. Section 2.1 summarizes the state of the art for our understanding of temporal and latitudinal trends of hazes' reflectivity, and about the vertical structure of the atmosphere. Based on this literature review, the research questions and objectives of this work are formulated in Section 2.2.

2.1. Literature review

Peer-reviewed articles focusing on Neptune's hazes have been following two main directions. On the one hand, analyses were conducted on the temporal trend of hazes' reflectivity, assessing how the measured flux from cloud-free regions changes over the years. This kind of study has been conducted both for whole disk and individual latitudinal bands. On the other hand, works have focused on the vertical structure of aerosol layers from observations in wavelengths spanning from visible to near infrared. The methodology adopted has been to model flux measurements by means of radiative transfer (treated in its theoretical aspects in Chapter 6).

The following literature review aims to give a context in which the state-of-the-art is, in order to find shortcomings and space to improve our body of knowledge on the matter. The effort is to summarize as briefly as possible these works for this. All details left outside, such as formulas or specific values, will be mentioned when comparing the result of this work with respect to literature in Chapters 4, 5 and 7.

2.1.1. Temporal trend of hazes reflectivity

Reflectivity changes over time have been object of study for several authors. The oldest work in this sense is provided by Lockwood and Thompson (2002) and its follow-ups (Lockwood and Jerzykiewicz, 2006; Lockwood, 2019). A short-term comparison is made by Sromovsky et al. (2001d) between observations collected in 1996 and 1998. The most recent paper on the topic is by Karkoschka (2011).

Lockwood and Thompson (2002) and follow-ups

This series of peer-reviewed articles is based on observations taken from Lowell Observatory, Arizona, in the Strömgren photometric system's b- and y-magnitude filters, sensitive to visible wavelengths close to 0.472 μm and 0.551 μm, respectively. The purpose of these measurements was the long-term characterization of solar system's objects. With respect to later spacecraft imaging (Voyager 2, HST), filters used for these ground observations lack the necessary wavelength coverage to identify individual atmospheric features. Measurements are nearly insensitive to discrete features, but the presence of large features can be spotted with anomalously increased short-term variations, such as sudden high brightness values with respect to other measurements. Nonetheless, photometry measurements of outer planets started in 1950, providing a unique long-term monitoring of the variations in magnitudes of Neptune.

Data provided in Lockwood's papers are disk-averaged annual mean magnitudes and cover nearly 65 of the 165 years of Neptune orbital period. In 1959, the planet passed its aphelion, thus getting closer to the Sun and reaching northern winter solstice in 2005. Figure 2.1 shows the lightcurve provided by Lockwood

(2019). The slowly increasing trend seen in the first years (1950-1990) dramatically changes to a unprecedented steady growth, peaking at solstice. The trend appears to be asymmetric with respect to solstice, suggesting the presence of either a seasonal lag or bright features altering the photometric behavior of the planet. Two departures from the smooth curve are noticed, corresponding to the two so-called outbursts in 1972-1977 and 1983-1990, when Neptune appeared anomalously brighter.

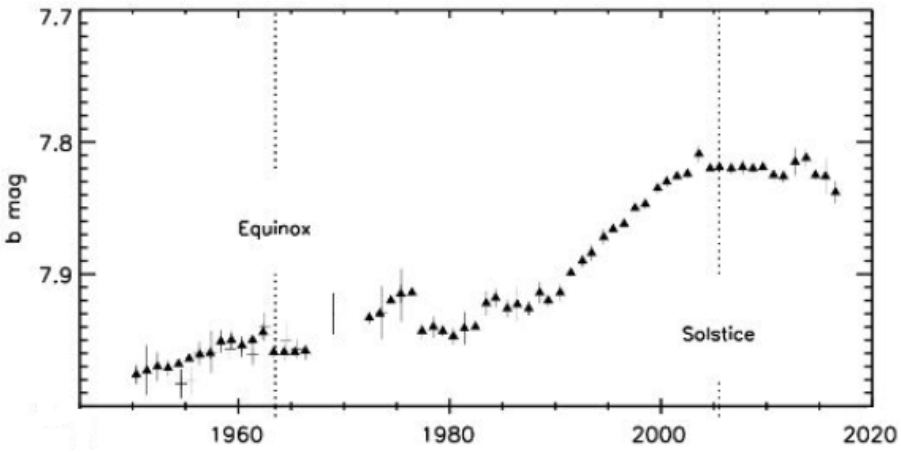

Figure 2.1: **Lightcurve of Neptune in Strömgren *b*-magnitude filter.** Data span between 1950 and 2018 (x-axis) and are provided in units of magnitudes (y-axis). The different markers indicate differential magnitudes (triangles) and magnitudes converted from B, V Johnson system to *b*, *y* Strömgren magnitudes (crosses). The dotted lines indicate the years for equinox and northern winter solstice in the Neptunian year. Error bars are equal to 2σ. The image displays the upper part of Figure 2 in Lockwood (2019).

If, on the one hand, the analysis done by these authors certainly has the advantage of offering an important comparison with measurements taken with other instruments, as they span a long time period and provide values for nearly all years, on the other hand several shortcomings are there. Firstly, a limited number of wavelengths is investigated (only two), which are also close to each other and sensitive to similar pressure levels of the atmosphere. Secondly, measurements capture an average behavior of magnitude variations, as they are disk-averaged. As a consequence, given the wavelengths investigated, they are not capable to identify whether specific latitudes are more responsible for the enhanced brightness.

Sromovsky et al. (2001d)

After having studied coordinated HST and Infrared Telescope Facility (IRTF) observations from 1996 (Sromovsky et al., 2001a,b,c), Sromovsky et al. (2001d) analyzed HST data from 1998 and compared them to the 1996 set, in order to point out the major changes in atmospheric circulation and cloud morphology. Variations are analyzed in three filters: F467M, F673N and F850LP, each of them sensitive to different pressure levels of the atmosphere. Specifically, the first allows to probe down to 10 bar, as it is most sensitive to particulate absorption in this pressure range, whereas the other two are most responsive to particulate scattering down to the 8-bar and 2-bar pressure levels, respectively.

Data are in terms of reflectivity, corrected for limb-darkening, i.e. the reduction of brightness near the edges of the planet caused by the increase of incidence and emission angles. As it will be seen in Chapter 3, reflectivity, or I/F, is a measure of brightness corrected for Sun-target and target-observer distances. The change in brightness is investigated both for dark cloud-free regions in its latitudinal trend and for disk-averaged reflectivities. Results are displayed in Figure 2.2. For the dark region analysis (left panel of Figure 2.2), the authors found an overall increasing brightness at all latitudes, with maxima different for each filter in terms of both value and latitudinal location. In the F467M filter, variations were small ($\sim \pm 1\%$), with peaks near 25°N, 45°N and in southern high-latitudes (75°S-60°S). Similar changes are seen for F673N, with the same peaks and magnitude of variation. Changes for F850LP were generally higher at all latitudes, with maxima reaching 15% (30°N) and lower peaks for 40°S-20°S (+4%).
Disk-averaged measurements (referred to as disk-integrated in the paper, right panel of Figure 2.2) revealed average variations that were smaller for F467M ($\sim 1.1\%$) and F673N ($\sim 1.4\%$) and larger for F850LP ($\sim 9.5\%$), implying the presence of brighter and more numerous clouds in 1998 with respect to 1996. The local maxima

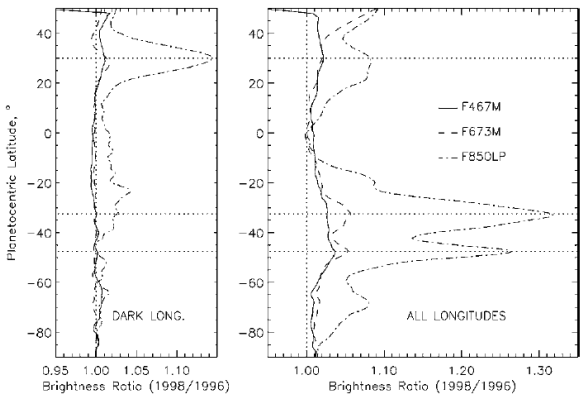

Figure 2.2: **Latitudinal brightness ratio between 1998 and 1996 for dark regions (left) and longitudinal averages (right).** Data are taken in the F467M (solid line), F673N (dashed) and F850LP (dashed-dotted) filters. The image is Figure 9 in Sromovsky et al. (2001d).

having the largest impacts on the overall observed brightness were located at 47°S and 32°S: these latitudes were marked by a stronger bright cloud activity with respect to 1996.

An extension of this study is done in Sromovsky and Fry (2003), in which brightness variations are quantified in the same three filter as above, adding data from 2002. The obtained percentage increases from 1996 to 2002 were found to be 3.2, 5.6 and 40% for F467M, F673N and F850LP, respectively.

The novelty introduced by these authors is in the latitudinal analysis of reflectivity variations and the attention given to dark regions. However, the considered time period is restricted to 6 years, limited from the availability of measurements from HST. Additional observations are needed to extend results in the temporal trend of dark regions' brightness.

Karkoschka (2011)

The most comprehensive study for hazes' variations in time was done by Karkoschka (2011). From WFPC2 images between 1994 and 2008, he analyzed changes in 10 visible wavelength filters, among which Sromovsky et al. (2001d)'s three filters, in disk-averaged albedo, and he focused on latitudinal variability for F467M and dark regions seen by methane absorption wavelengths filter (i.e. sensitive to wavelengths greater than 0.65 μm). Most of his results are shown in figures reported for convenience in Chapter 5, to allow for a more direct comparison with the results of our work.

He found an analytical expression to model the reflectivity changes over time in the continuum (non-methane absorption) filters, whose form includes a constant minus an exponential decay:

$$\mathrm{I/F} = A - Be^{-t/t_1} \tag{2.1}$$

with parameters A and B dependent on latitude and wavelength, $t_1 = 5$ years the time scale and t the year in which the I/F is desired. The fit is shown in Figure 5.3, which returns a good agreement except for the 1996-1998 period between 15°N-30°N (later measurements are also fitted with Equation 2.1).

His results in global disk-averaged photometry are reported in Figure 5.7. The largest increase in reflectivity is displayed in F467M in the southern part of the planetary disk, whereas a trend consistent with a constant I/F is found for filters covering methane absorption wavelengths when clouds are removed. Looking at the trend including clouds, a general brightening is observed in all filters. F467M is also compared with Lockwood and Jerzykiewicz (2006) results, showing a good match between the two datasets (Figure 2.3).

The novelty proposed by this author stems in the connection made between reflectivity changes and variations in the vertical structure of the atmosphere. In fact, the author hypothesized a cause-effect link for increasing brightness and settling of dark hazes at a 1-bar-per-year rate. Nevertheless, today the reported study misses more than 10 years of observations done by WFPC2's follow-on WFC3 from 2009 onward, whose inclusion would clarify whether Karkoschka (2011)'s fit for reflectivity describes also more recent measurements or not.

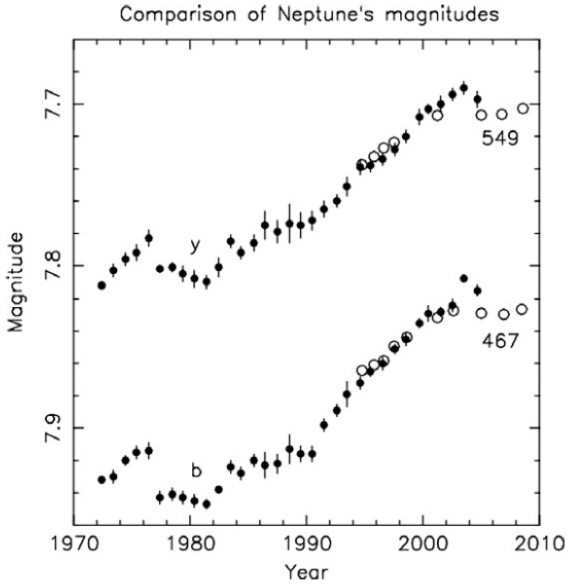

Figure 2.3: **Comparison between Karkoschka (2011) (white dots) and Lockwood and Jerzykiewicz (2006) (black dots) datasets.** Comparisons are made between HST F467M and Lowell *b*-magnitude (bottom), and HST F547M and Lowell *y*-magnitude filters (top). The image is Figure 2 in Karkoschka (2011).

2.1.2. Vertical structure of hazes

The atmospheric vertical structure describes the atmosphere in terms of pressure levels (or altitudes) at which aerosol and cloud layers are present. The relevant works in this sense are from Sromovsky et al. (2001b), Luszcz-Cook et al. (2016), Molter et al. (2019) and Karkoschka and Tomasko (2011). From these works, three models have been proposed, with Sromovsky et al. (2001b), Luszcz-Cook et al. (2016) and Molter et al. (2019) having a similar model and Karkoschka and Tomasko (2011) favoring an alternative description. Each work is hereby summarized in its major findings. Some concepts, such as optical depth and scattering albedo, are mentioned. Their rigorous definition is explained in Chapter 6. For now, it is sufficient to understand that an optically thin layer allows more light to pass through itself with respect to an optically thicker layer, which is more reflective or absorptive. In addition, high scattering albedo causes more light to be scattered (i.e. redirected).

Sromovsky et al. (2001b)

The vertical structure model proposed in Sromovsky et al. (2001b) is based on the visible and near infrared observation of HST and IRTF from 1996. Data are processed as in Sromovsky et al. (2001d), i.e. correcting for limb-darkening and expressed in terms of reflectivity.

Using measurements from cloud-free regions, the authors fitted their observations with a model atmosphere comprising of a homogeneous optically thin cloud based at 1.3 bar and an underlying optically thicker layer at 3.8 bar, formed by H_2S aerosols, perhaps extending down to 7 bar, where hydrogen sulfide has its condensation level. When bright clouds are present, a heterogeneous third layer is added at 0.1 bar. With this structure, the I/F expected per wavelength, computed by means of radiative transfer (Chapters 6-7) has a good fit with the measured data.

The resulting vertical structure is visualized on the left of Figure 2.4. Particles in the lower haze layer were estimated to have a single scattering albedo near unity shortward of 0.8 μm, after which it was thought to decrease down to 0.8 at 0.9 μm. For the 1.3-bar layer, scatterers composed a layer with optical depth up to 0.1.

Luszcz-Cook et al. (2016) and Molter et al. (2019)

An analogous discrete-layered structure was inferred by Luszcz-Cook et al. (2016) from measurements taken by Keck OSIRIS camera at infrared wavelengths (1.47-2.38 μm) at the limbs of the planet. Their model is depicted in the center of Figure 2.4 and it was built from observations in dark regions at 2°N-12°N latitude, using a former version of the radiative transfer code employed for this work (see Chapter 6).

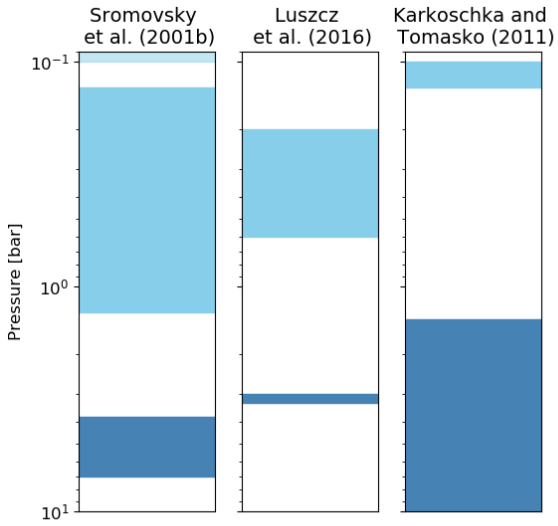

Figure 2.4: **Vertical structure as modeled by Sromovsky et al. (2001b) (left), Luszcz-Cook et al. (2016) (center) and Karkoschka and Tomasko (2011) (right).** The y-axis represents pressure in a logarithmic scale. In Sromovsky et al. (2001b)'s model, the upmost layer is placed at 0.1 bar and it is absent in cloud-free regions. The middle layer is optically thin, so that light passes through it easily, and based at 1.3 bar. The bottom layer is thought to be composed of hydrogen sulfide, based at 3.8 bar and might expand down to 7 bar, as at this pressure the H_2S condensation level is present. The extent of the top and middle layers is arbitrary. In Luszcz-Cook et al. (2016)'s model, the optically thin upper haze is placed at 0.59 bar, whereas the optically thicker lower haze at 3.3 bar: their extent is also drawn arbitrarily. In Karkoschka and Tomasko (2011)'s model, the optically thin discrete bright haze is based at the tropopause (0.13 bar), whilst the semi-infinite dark haze starts from 1.4 bar. The nuances of blue qualitatively indicate the optical depth, with darker blue for optically thicker layers and light blue for optically thinner hazes.

After having explored multiple solutions, e.g. single layer structures and different atmospheric methane abundances, the best fitting model for the specified region and wavelengths was found to have two layers, as for Sromovsky et al. (2001b) cloud-free case. The upper haze layer was based at 0.59 bar, vertically extended, optically thin and formed by highly scattering particles. The lower haze was placed at 3.3 bar, optically thicker and more compact with respect to the upper layer, with low scattering particles. Physical parameters of the hazes were also retrieved from other latitudes: a latitudinal variability was shown in terms of pressure levels and vertical extension of the two haze layers. The layers were thought to get more vertically compact and closer to each other for latitudes south of 45°S, to the point that they overlap.

This model is extended by Molter et al. (2019) to visible wavelengths, in the modeling of background hazes for the characterization in reflectivity of the 2017 equatorial storm seen on Neptune. The retrieved model is different only for the scattering albedo of the lower haze's particles. This parameter was modeled with a spectral dependence, i.e. its value depended on wavelength, in order to smoothly model the transition from 1.0 in the visible to 0.45 at 1.6 μm, respectively. In terms of pressure levels, the configuration was the same as in Luszcz-Cook et al. (2016).

Karkoschka and Tomasko (2011)

With respect to the aforementioned papers, the vertical structure model proposed by Karkoschka and Tomasko (2011) is different. From visible wavelengths observations with HST-STIS in 2003, the authors inferred the model displayed on the right of Figure 2.4.

Instead of a two discrete haze layers model, the authors favored a solution comprising of a stratospheric optically thin haze layer, based at the tropopause (separation surface between stratosphere and troposphere) pressure level (0.13 bar), and a semi-infinite dark haze layer, extending from 1.4 bar to deeper pressures. The latitudinal variability seen in reflectivities was accounted for with changing methane humidity at the 1.2-3.3 bar level. The novelty introduced by these authors is in the new empirical parameterization of the single scattering albedo of particles in the lower haze layer, modeled according to a spectral dependence to fit empirical observations in the visible range.

2.2. Research questions

Based on the literature review presented in the previous Section, three main problems are identified.

The first one concerns the temporal evolution of reflectivity. On the one hand, former works that provided a long-term characterization of brightness have focused mainly on disk-averaged measurements in limited wavelengths (Lockwood, 2019), lacking the spatial resolution necessary to understand which latitudes mostly drive the observed trend. On the other hand, papers dedicated to reflectivity latitudinal variability (Sromovsky et al., 2001d; Sromovsky and Fry, 2003) analyzed time intervals not exceeding 6 years, which is a short time scale with respect to the 165-year orbital period of the planet. Karkoschka (2011) did so, putting together more than 10 years of measurements and studying the latitudinal trend. Nonetheless, the bands he identified (i.e. 60°S-30°S, 20°S-10°N, 15°N-30°N) are broad and not covering the whole visible planetary disk, thus not providing a refined analysis. In addition, HST has now collected more than 10 years of observations not included in the study, since they were not available, that does not invalidate the findings, but makes them old.

The second problem is related to the vertical structure. As Figure 2.4 shows, Neptune's vertical structure is still debated in its number and extension of aerosol layers. Empirical brightness values were fit with a discrete (Sromovsky et al., 2001b; Luszcz-Cook et al., 2016; Molter et al., 2019) or a semi-infinite (Karkoschka and Tomasko, 2011) lower haze layer, with discrepancies in analyzed locations and pressure levels altitude of all layers. As a result, the characterization of the vertical structure latitudinal variation has been explained with different changing parameters: Luszcz-Cook et al. (2016) found varying pressure levels, whereas Karkoschka and Tomasko (2011) favored changes in the methane relative humidity. Also, the different wavelength regions inquired cause discrepancies. For example, the latitudinal variability seen by Luszcz-Cook et al. (2016) was explained with a changing upper haze layer pressures and optical depths, since their infrared observations are more sensitive to it, whereas Karkoschka and Tomasko (2011), looking at visible wavelengths, explained this variability in terms of methane relative humidity changes in the troposphere. With different wavelengths, different conclusions are reached for the atmospheric structure.

The third problem comes as a combination of temporal reflectivity changes and vertical structure modeling. Only Karkoschka (2011) looked for variations in the vertical structure to account for the brightness trend he observed, motivating it with the settlement of the dark lower haze in Karkoschka and Tomasko (2011)'s model. As noted for the temporal analysis, the paper misses more than 10 years now, so that it should be complemented to assess whether the trend has continued.

From these three open problems, the research questions for this work are formulated as follows.

1. How does Neptune's hazes brightness trend at visible wavelengths change in the last 10 years with respect to previous analyses?
   (a) How has reflectivity changed over time globally, i.e. in a disk-averaged sense?
   (b) How has reflectivity changed over time locally, i.e. looking at specific latitudinal bands?
2. What is the best fitting vertical structure model that agrees with visible data we collect from the whole HST mission time period?
   (a) How does the vertical structure vary with latitude?
   (b) For each latitudinal band, how does the structure change in time?

The objective of this work is to characterize the long-term evolution of hazes, in its brightness and vertical distribution, by analyzing HST visible data between 1994 and 2018 and finding their best-fitting atmospheric model by means of radiative transfer modeling.

3

Data processing

This Chapter presents the methodology adopted in collecting and processing Neptune's images to extract brightness measurements. Section 3.1 explains the kind of images retrieved and where these were taken from. Section 3.2 describes how the images were navigated and the reference system of the planet was built. The extraction of photometric values from the pictures is reported in Section 3.3, followed by the assessment of errors on the computed brightness (Section 3.4).

3.1. Data selection

Images of Neptune were retrieved from HST's WFPC2 and WFC3 data archives. In the analysis of hazes temporal variations, two filters were selected in the visible region for each camera: F467M, present on both cameras and covering blue wavelengths; F850LP (WFPC2) and F845M (WFC3), covering methane absorption bands. The reader is referred to Appendix A for details on F850LP and F845M filters. The emphasis is put on these three filters for two reasons. Firstly, we consider them to be representative as they cover wavelengths where methane absorption is (F850LP/F845M) and is not (F467M) strong. Secondly, pictures in these filters are the most numerous among all available WFPC2 and WFC3 filters.

Figures 3.1-3.2 display a selection of images from each filter. The different peak wavelengths of the filters make them sensitive to different altitudes of the atmosphere. Specifically, F467M, hereafter referred to as *blue filter*, probes pressure layers as deep as 2-4 bar (Sromovsky and Fry, 2003), limited by Rayleigh scattering, resulting in a high background reflectivity (Figure 3.1). The F850LP/F845M filters, hereafter referred to as *methane filters*, show an enhanced contrast between bright clouds and dark background, due to the dominant effect of methane absorption, which allows to probe altitudes down to 1 bar (Sromovsky et al., 2001d).

The pictures span years from 1994 to 2018 and were retrieved from the Space Telescope Science Institute (STScI) Milkuski Archive for Space Telescopes (MAST) portal[1]. The data product provided is in the *fits* format: the image has units of electrons per second and it is complemented with a header file, specifying engineering parameters, position of the planet with respect to the telescope when imaged, time of observation and general information about the observation. The main source of data used was the High-Level Science Product (HLSP) Moving Target Pipeline, providing images with a common orientation, rescaled to a common pixel scale, drizzled through AstroDrizzle[2] and put through a cosmic ray rejection routine (Wong et al., 2018). The common orientation is such that the picture's vertical axis is aligned with the sky North direction. The rescaling provides images with the same pixel scale, i.e. such that the area subtended by a single pixel is the same for all images, regardless of the observer-target distance. The drizzling procedure allows to linearly reconstruct undersampled images (i.e. with too few pixels) and corrects for geometric distortions (Fruchter and Hook, 2002). The cosmic rays rejection routine removes artefacts caused by cosmic rays hitting pixels in the camera charge coupled device (CCD). In order to have better temporal coverage, measurements from the HST Data Search were included. Images coming from HST Data Search were still corrected for cosmic rays and drizzled, but neither were oriented according to the HLSP data product nor rescaled. Of 470 Neptune images, 20 were discarded due to analysis unsuitability, caused by various reasons: the planet was only partially included in

[1] `https://archive.stsci.edu/`
[2] `http://www.stsci.edu/scientific-community/software/drizzlepac.html`

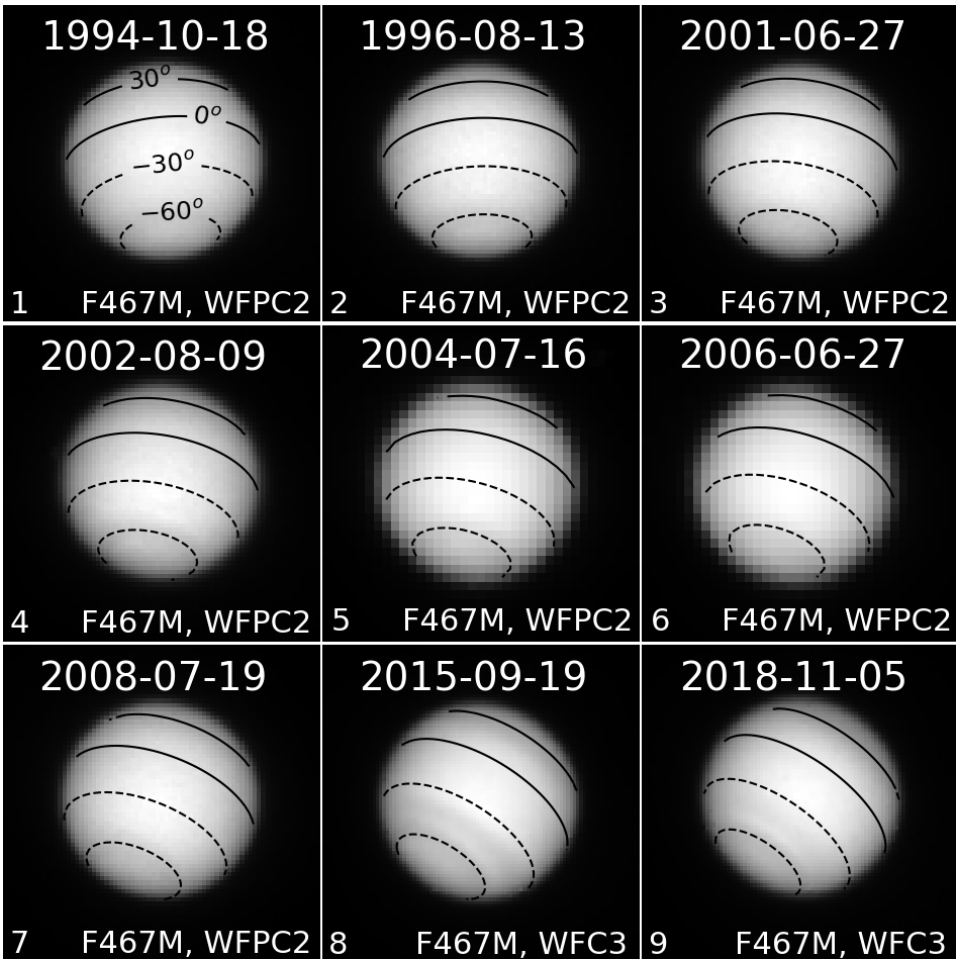

Figure 3.1: **Selection of Neptune observations in the F467M blue filter.** Panels 1-7 were obtained from WFPC2, panels 8-9 from WFC3. The planetary disk is overlain with black latitude lines every 30°, with solid lines representing northern latitudes and dashed lines representing southern latitudes. The latitude value for each line is indicated in Panel 1 and the values are the same for all subsequent panels. The lower resolution of images in 2004-2006 is due to the different database from which they were retrieved, namely HST Search, instead of the HLSP MT project.

the image, if not completely missed, or Neptune was severely blurred, or the image was altered by artefacts. In the end, the data selection included 241 images in the F845M/F850LP filters (214 for F845M and 27 for F850LP) and 209 images in the F467M filter.

Two significant temporal gaps are present in the data. The first one is between 2002 and 2007, where we lack images in the F850LP filter. The second one is between 2011 and 2014, where WFC3 did not record any measurements of Neptune.

For the radiative transfer modeling, data were not limited to the blue and methane filters. Images were retrieved from all filters through which WFPC2 and WFC3 observed the planet. Specific years were selected, based on the availability of measurements and the previous temporal analysis. As it will be seen in Chapter 7, in 1996, 2002, 2009, 2015 and 2018, observations in 5 or more filters were performed by the cameras. The higher the number of filters that provided measurements, the better the model atmosphere is constrained, as reflectivities for more wavelengths are available. Furthermore, the significance of these years is due to the fact that these dates correspond to the boundaries of the time intervals identified from the temporal trend found in the blue and methane filters (Chapter 5). The sources for these observations are the same as the blue and methane filters and the images were processed analogously, as described in Section 3.2. In the end, the data selection for the radiative transfer modeling included 130 images in 25 different filters, from 0.336 to 0.953 μm.

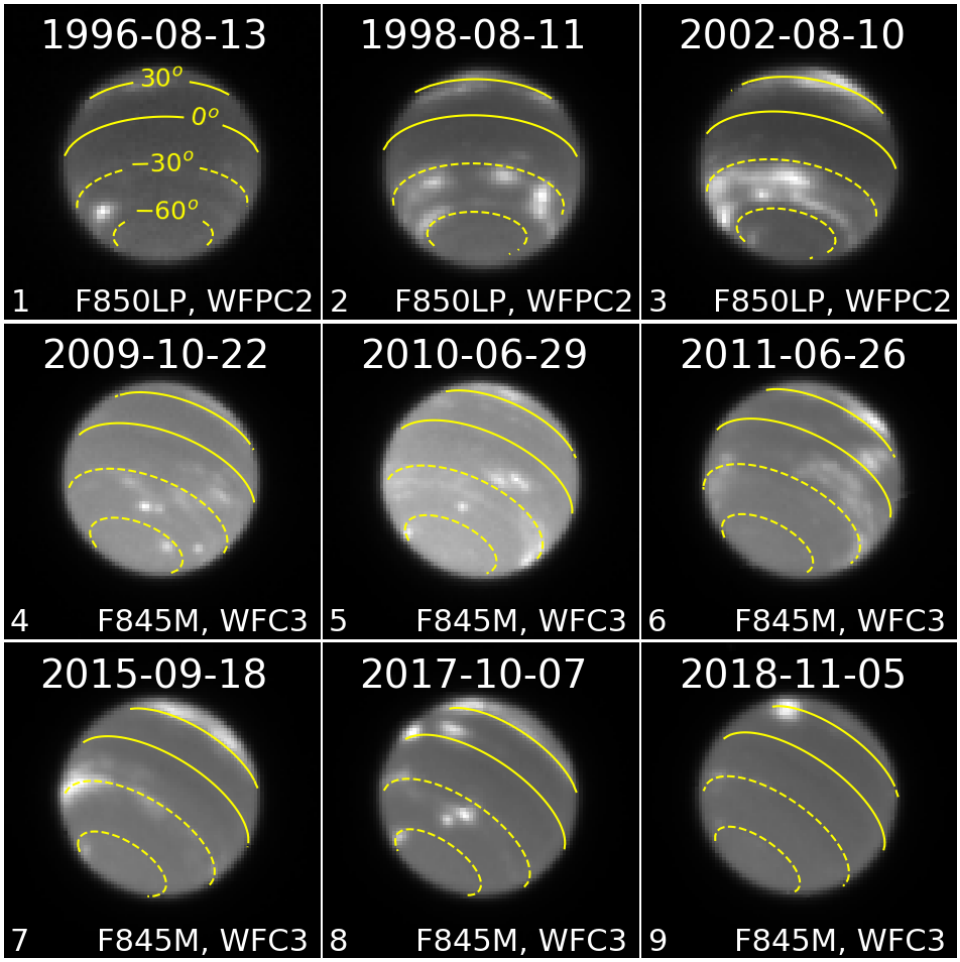

Figure 3.2: **Selection of Neptune observations in the F850LP/F845M methane filters.** Panels 1-3 were obtained from WFPC2's F850LP filter, panels 4-9 from WFC3's F845M filter. The planetary disk is overlain with yellow latitude lines every 30°, with solid lines representing northern latitudes and dashed lines representing southern latitudes. The latitude value for each line is indicated in Panel 1 and the values are the same for all subsequent panels. At these wavelengths, the contrast between clouds and background is sharper than in the images taken with the F467M filter.

3.2. Image navigation

For the latitudinal temporal analysis and the radiative transfer modeling, each image was processed with the Python navigation code from Molter et al. (2019), adapted to handle HST data. The routine produces deprojected maps of the planet from the telescope's images, i.e. projection of the planetary disk onto a rectangular (x,y) coordinate system.

To HST Data Search files, lacking a common orientation, a preliminary rotation was applied to align the image's vertical direction with the sky North Pole direction. The angle formed by the y-axis of the image with respect to the North direction is stored under the header's keyword "ORIENTAT", indicating the degrees in the East (clockwise) direction. A rotation of 360° – ORIENTAT returns the planet oriented as the HLSP files. This task was implemented with the `ndimage.rotate()` function of the `scipy` Python package.

Following the rotation, the position of the planet in the image was found through the conversion of Neptune's World Coordinate System (WCS) coordinates to (x,y) pixel coordinates, using the `wcs_world2pix()` function of the `astropy` Python package. The image was cropped into a square, centered on the target position and its edges were identified by means of the Canny edge algorithm (Canny, 1986) included in the `scikit-image` package. An elliptical latitude/longitude reference system was overlain on top of it, having an equatorial radius r_{eq} = 24764 km and a polar radius r_{pol} = 24341 km (Yoder, 1995) and accounting for the relative distance between the observer and the target, and the orientation of the rotation axis of the planet at the time of observation, retrieved from JPL's *Horizons*[3].

[3] `https://ssd.jpl.nasa.gov/horizons.cgi`

To build the latitude/longitude model, the dimensions subtended by a single detector's pixel, referred to as the pixel scale, are required. The two data sources store this quantity in two different header entries. Specifically, in HLSP data, the pixel scale is given by $\sqrt{\text{CD1\_1}^2 + \text{CD1\_2}^2} \cdot 3600$, with CD1_1 and CD1_2 header keywords. HST data provide the value directly from the "D001SCAL" keyword. The Molter et al. (2019) navigation code is publicly available on GitHub[4].

On the other hand, for global photometry analysis, image processing was restricted to find the planet in the picture and crop a square in which the planet is centered. In disk-averaged assessment, the average of reflectivities extracted solely from the deprojected surface would miss a significant part of the real flux density. Indeed, the point spread function (PSF) is not completely contained on the planetary disk, but leaks outside it, forming a halo (Gonzaga and Biretta, 2010). Taking into account the surroundings of the planet assures the inclusion of nearly all the PSF.

3.3. Data reduction

The flux density retrieved from images was converted to I/F, as defined by Hammel et al. (1989a), to eliminate the dependence on heliocentric and geocentric distance:

$$\frac{I}{F} = \frac{r^2}{\Omega}\frac{F_N}{F_\odot} \tag{3.1}$$

r is the planet's heliocentric distance, expressed in AU, retrieved from JPL's *Horizons* ephemerides generator. Ω is the solid angle of interest over which the flux F_N is measured, in steradians: this could be as small as a single detector pixel or as large as Neptune's full visible disk. $\pi F_\odot$ is the solar flux density at Earth's distance and F_N the observed flux density, both expressed in consistent units, e.g. erg cm^{-2} μm^{-1} s^{-1}. The solar flux density was taken from Colina et al. (1996). The observed flux density F_N was obtained through the conversion of the data provided in the images, given in units of electron per second, to erg cm^{-2} μm^{-1} s^{-1}, multiplying the data count with the inverse sensitivity (i.e. the flux density that produces a response of one electron per second, Gonzaga and Biretta, 2010) of the considered image filter, stored under the PHOTFLAM keyword. Nonetheless, the inverse sensitivity keyword in the HLSP archive is incorrectly populated (McMaster, 2009), as it returns an incorrect value for flux density; this was corrected according to the McMaster and Biretta (2008) gain value of 7.12, for which the inverse sensitivity was multiplied to lead to the correct flux density value. For the methane filters, given their sensitivity to bright clouds, we estimated reflectivities after having applied the cloud removal technique reported in Appendix A, as we are interested in the background hazes in cloud-free regions.

We followed Sromovsky et al. (2001c)'s approach in applying a limb-darkening correction, in order to make visible features at the edge of the disk (e.g. bright clouds). To reduce limb-darkening effect (darker pixels on the edge of the planet), we applied the Minnaert correction function to the extracted I/F, to obtain the Minnaert-corrected I/F$_{\text{corr}}$:

$$\text{I/F}_{\text{corr}} = \text{I/F}\ \mu_0^{-k}\mu^{1-k} \tag{3.2}$$

where μ_0 and μ are the cosine of the incidence angle and the cosine of the emission angle, respectively (Wong et al., 2018). The incidence angle is the angle formed by the direction of incoming solar rays with respect to the normal of the surface, where the rays hit the atmosphere. The emission angle is the angle formed by the direction of propagation of light reflected from the atmosphere, again with respect to the normal of the surface. k is an empirical factor computed for each filter by fitting data at all longitudes. From Equation 3.2, it is possible to put in evidence k, taking the natural logarithm on both sides of the equation:

$$\ln(\text{I/F}_{\text{corr}}) = \ln(\text{I/F}) - k\ln(\mu_0\mu) + \ln(\mu) \tag{3.3}$$

Including $\ln(\mu)$ in $\ln(\text{I/F})$ and reordering Equation 3.3 gives:

$$\ln(\text{I/F}\ \mu) = \ln(\text{I/F}_{\text{corr}}) - k\ln(\mu_0\mu) \tag{3.4}$$

Equation 3.4 has the same form as the equation of a line: $y = b + mx$ with slope $m = k$, ordinate $y = \ln(\text{I/F}\ \mu)$, independent variable $x = \ln(\mu_0\mu)$ and y-axis intercept $b = \ln(\text{I/F}_{\text{corr}})$. Since I/F, μ and μ_0 are known terms, it is possible to estimate slope k as the linear fit of the points with coordinates $(\ln(\mu_0\mu), \ln(\text{I/F}\ \mu))$. Pixels

[4] https://github.com/emolter/nirc2_reduce

with $\mu < 0.3$ were excluded from the correction and neglected in average computations, since the first-order approximation in Equation 3.2 is no longer accurate (Wong et al., 2018).

In addition, the Minnaert correction is also beneficial for the radiative transfer modeling part of this work. Indeed, the correction returns I/F values as if every location had $\mu = 1$. The employed radiative transfer code (Chapter 6) handles a single emission angle at the time, so that, in modeling a certain latitude region, we would need to run simulations for several emission angles. Using the Minnaert function allows for a lower computational time, as every pixel has $\mu = 1$,

3.4. Error assessment

We computed errors on reflectivities considering two contributions: photometric uncertainty and random (statistical) errors.

The photometric accuracy of WFPC2 and WFC3 amounts to 2% of the measured I/F for intermediate and broad filters and 5% for narrow filters (Gonzaga and Biretta, 2010; Gennaro et al., 2018). This error can be considered systematic for measurements done in a given filter, as it does not change over time, and thus cannot be reduced by multiple measurements. Nonetheless, this error is potentially random from filter to filter, since it comes as a combination of HST calibration and the solar spectrum uncertainties. As a consequence, when comparing measurements in a single filter, the photometric error, being systematic, can be neglected, as it will be done in Chapters 4-5. On the other hand, when plotting measurements taken in different filters, as done in Chapter 7, the photometric error has to be included.

The random contribution comes from the statistical background noise of the image, quantified as the root mean square of the reflectivity fluctuations seen in a background region of the considered image. Differently from the photometric error, it can be lowered with the increase of measurements.

In averaging multiple measurements, we assessed the error σ_n associated with the yearly mean to be the standard error of the mean, i.e. the standard deviation σ_s of the N images from a certain year reduced by a factor of $1/\sqrt{N}$, to account for the variation between images. To this error, the photometric uncertainty σ_{phot} was added in quadrature:

$$\sigma_n = \sqrt{\left(\frac{\sigma_s}{\sqrt{N}}\right)^2 + \sigma_{\text{phot}}^2} \tag{3.5}$$

with σ_{phot} the 2-5% of the mean I/F of the N images in a specific year.

4

Global reflectivity

In this Chapter, results in disk-averaged reflectivity are presented. Section 4.1 deals with the blue filter behavior, while Section 4.2 reports what is seen in the methane filters. In both Sections, results are presented and compared with previous literature.

4.1. Reflectivity from F467M filter

Figure 4.1 shows the resulting disk-averaged reflectivity values computed from HST measurements for the blue filter between 1994 and 2018 (red), compared to historical data from Lockwood (2019) (blue). The peak wavelength of the HST blue filter (λ_{peak} = 467 nm) is close enough (1%) to the sensitivity of Strömgren *b*-magnitude filter (λ_{peak} = 472 nm) used by Lockwood (2019) that we can compare the two datasets. Lockwood (2019)'s photometric observations of Neptune from Lowell observatory, dating back to 1950, are disk-averaged annual mean opposition measurements, obtained from multiple images taken during half-dozen nights. Brightness is expressed in magnitudes. To convert them in terms of I/F, the following expression was applied (Gonzaga and Biretta, 2010):

$$F_N = F_\odot \cdot 10^{\frac{m_\odot - m_N}{2.5}} \tag{4.1}$$

with $m_\odot = -26.43$ mag the Sun brightness in magnitudes (de Pater and Lissauer, 2011), m_N Neptune's brightness in magnitudes (found in Lockwood, 2019) and $F_\odot = 204.6 \cdot 10^6$ erg cm^{-2} μm^{-1} s^{-1} the solar flux density at wavelength λ = 472 nm (Colina et al., 1996). The resulting F_N is the one that has to be inserted in Equation 3.1 to obtain the desired I/F. Converting these data from magnitudes to I/F, a close agreement with the overlapping measurements from 1994 to 2018 is seen. The error bars on the HST data take into account only the spread of data in each year, as Karkoschka (2011) did. The photometric error ($\sim$ 0.01) is to be considered systematic (Section 3.4) and thus can be neglected in the plot.

Prior to 2015, HST data appear to be shifted downwards by $\sim$ 0.005. This shift, also noticed in Karkoschka (2011), who made the comparison with Lockwood and Jerzykiewicz (2006) as well, is at least in part caused by the slight differences in the filters used. In addition to the slight difference (5 nm) in peak wavelength between the *b*-magnitude filter and HST's F467M filter, the *b*-magnitude filter transmission curve includes a broader wavelength region. Hence, the two filters see a slightly different wavelength range. To be able to compare them, it is necessary to quantify a scaling factor between the reflectivities observed by the two filters, with the methodology described in Appendix B. The convolved point for Lowell is a factor of 1.01 higher with respect to the HST convolved point. Multiplying HST data by 1.01 produces the desired upwards shift of $\sim$ 0.005, so that the two datasets are in excellent agreement. Additional differences may be caused by shorter-term variations.

From Figure 4.1, we notice that our HST measurements follow the increasing trend up to 2003 detected by Lockwood (2019) and consistent with Karkoschka (2011). The growth in this initial period, from 0.538 (1994) to 0.563 (2003), amounts to 4.6%, in close agreement with Sromovsky and Fry (2003), and thus falls outside the error bar range of the 1994 data point. The difference is statistically significant, as the growth is continuous in many blue filter's observations in this time period. In fact, 1994-2002 data are fitted in a least squares sense with a linear function with slope 0.0030 ± 0.0003, hinting at an increasing behavior. The subsequent 2004-2008 I/F values are distributed around a constant value ($\sim$ 0.558). The linear fit of these points returns a slope

of 0.0003 ± 0.0003, consistent with no change over this time interval. After the 2008-2015 gap in WFC3 data, in the most recent period (2015-2018), the behavior hints at a decreasing trend, dropping from 0.559 to 0.548. The slope of the fitting line is -0.003 ± 0.002, favoring a decreasing trend as well. Since the same trend is observed in both Lockwood (2019)'s and this HST dataset, this behavior is most likely real.

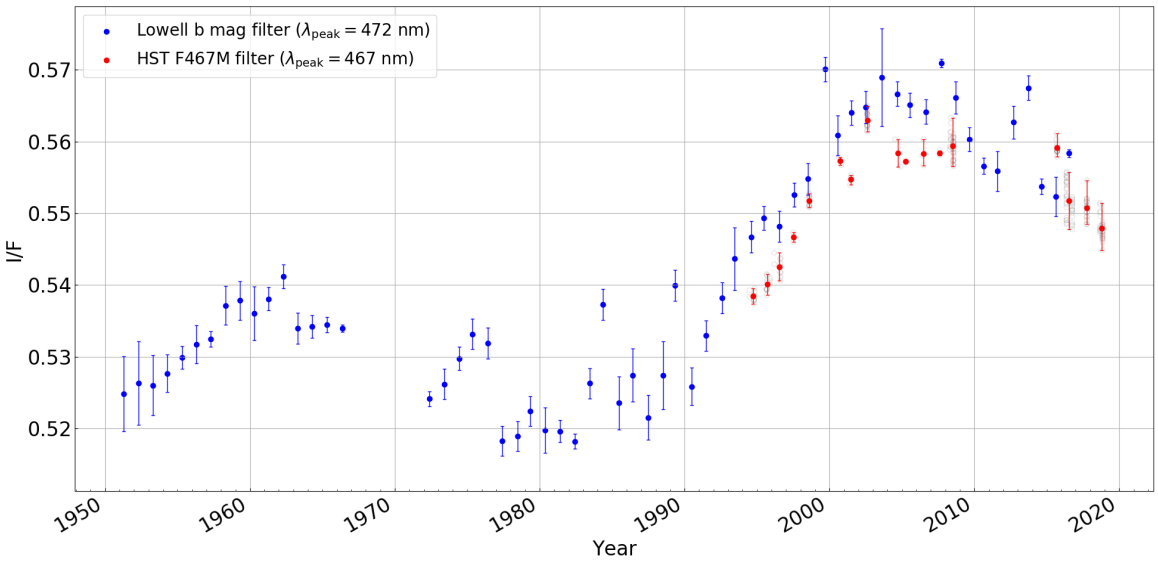

Figure 4.1: **Disk-averaged reflectivities from F467M**. HST data (red points) are compared to Lowell *b*-magnitude data (blue points), taken from Lockwood (2019) and converted from magnitudes to I/F. The small offset between the two datasets is due to differences in filter shapes and short-term variations. Error bars include only the variance of data within the same year, whose individual points are faintly plotted as empty circles. The systematic photometric error for HST amounts to an I/F ~ 0.01.

4.2. Reflectivity from F850LP and F845M filters

Disk-averaged I/F values were computed for the methane filters as for the blue filters. At these wavelengths, there are no historical records as we had for F467M with Lowell's measurements. Unlike in the blue filter, WFPC2 and WFC3 do not have a common filter with the same central wavelength, so that a corrective factor of 1.65 is applied to the WFPC2 data (see Appendix B) to enable a direct comparison between them. The resulting I/F values are shown by the cyan points in Figure 4.2. Between 1996 and 2002, the reflectivity increased by 39% (from 0.0703 to 0.0977), in good agreement with Sromovsky and Fry (2003). 2002 stands out because of the anomalously high cloud activity (see Figure 3.2, panel 3). In 2009-2011, the reflectivity trend is consistent with a constant trend within error bars. In 2015-2018, the mean disk-averaged reflectivity decreases by 13.1% from 0.069 to 0.061, but the extent of the error bar does not rule out a constant behavior.

To isolate the contribution from the hazes only, a cloud removal technique was applied to the Minnaert-corrected projected images (see Appendix A), and then the mean I/F was computed from all remaining pixels in the map. These "mean cloud-free" I/F values are shown by the black points in Figure 4.2. With respect to the disk-averaged data, the clear increasing trend between 1996 and 2002 is not there anymore. The linear fit of these points is affected by an uncertainty as large as the slope itself, namely 0.00058 ± 0.00059, consistent with either an increasing or constant behavior. This is also the case for 2009-2011, for which the linear fit results in a slope of 0.0001 ± 0.0006, again not ruling out neither an increasing, constant nor decreasing trend. The negative slope value for the linear fit of data in 2015-2018 (-0.0008 ± 0.0006) corroborates the decreasing behavior in this period. Figure 4.2 shows that contributions from the bright clouds (cyan points) increase the planet's brightness by up to a factor of 1.5. The presence of clouds also increases the variance between data points taken in the same year due to the short-timescale evolution of cloud features and the planet's rotation (Sromovsky et al., 2001c; Smith et al., 1989). It is noted that the exclusion of large emission angles from the cloud-free I/F values also contributes somewhat to the difference between these values and the disk-averaged values, but this is a second-order effect.

The majority of years with larger spread in disk-averaged reflectivity values are associated with strong

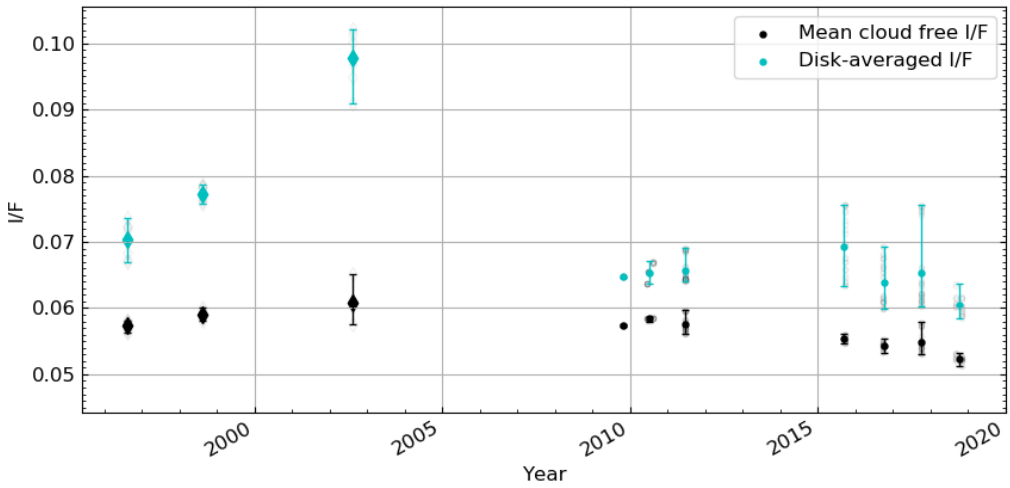

Figure 4.2: **Disk-averaged and mean reflectivities for methane filters**. The cyan points represent the disk-averaged I/F, to which no cloud removal procedure was applied. The black points are mean reflectivities computed from regions to which we applied the cloud removal technique described in Appendix A. The symbols distinguish WFPC2 (diamonds) and WFC3 (circles) data. The higher values for the disk-averaged data are due to the contribution of bright clouds. Error bars include the variance in each year.

atmospheric activity, such as the presence of a dark spot's bright companions, or the occurrence of bright storms. These are 1996, 2002, 2015 and 2017.

HST imaging in 1996 found several bright features on Neptune, such as the pair of clouds at 45°S reported by Sromovsky et al. (2001c). The points with higher I/F correspond to images in which the clouds are visible on the planetary disk. On the contrary, the lower points are representative of pictures where the bright features are closer to the planetary disk edges or not visible.

No literature documented the high cloud activity in 2002 at the southern mid-latitudes. The error bar lower extent is caused by a single image, where we observed fainter bright structures, resulting in a lower reflectivity value.

In 2015, a new dark spot was reported (Wong et al., 2018). The vortex, referred as SDS-2015, displayed a bright companion on its north side, near 40°S. Its passage on the visible side of the planet caused an increase of the overall reflectivity on 18 September 2015, so that the corresponding data points are the ones with higher I/F.

Molter et al. (2019) reported the finding of an equatorial bright storm in 2017. Our data were taken on 6-7 October 2017. The higher values in reflectivity are associated with images where the storm was in view, taken between 8:59 and 9:45 on the first day (not in view at 5:49 and after 14:29), and between 2:28 and 3:14 on the second day (not in view at 00:00 and after 7:58). The description of the morphology of the storm in October 2017, consisting of two distinct clouds, is witnessed in our HST images. As for SDS-2015, the time intervals are consistent with the rotational period of the storm, i.e. 17.5 hours (Molter et al., 2019), meaning that for approximately less 8.7 hours the storm dominates the contribution to the increased disk-averaged I/F values. Other bright features were noticed, such as the SDS-2015 companion and the 2015-P* cloud, both fainter than two years earlier (Wong et al., 2018).

5

Latitudinal variations

The following Chapter presents results in reflectivity trends extracted for specific latitudinal bands. These bands are defined in Section 5.1. For each band, its variability in brightness is reported for the blue (Section 5.2) and the methane filters (Section 5.3). Throughout the Sections, a comparison with previous studies is provided.

5.1. Latitudinal bands selection

The planetary disk was divided in latitudinal bands according to the impact that bright clouds have in the methane filters. Figure 5.1 shows the ratio between longitudinally averaged reflectivity and mean cloud-free reflectivity for each latitude, both computed as average in the time period from 1996 to 2018. The higher the ratio, the stronger the presence of bright clouds. Bands were identified starting from the two principal peaks between 50°S-30°S and 20°N-50°N. Intermediate cloud incidence bands are found at the local maximum between 75°S-65°S and the increasing value at 5°N-20°N. Lower impact regions are 90°S-75°S, 30°S-5°N and northward of 50°N. Therefore, 7 bands were defined, as for latitudes higher than 50°N the limb-darkening is not properly corrected for, since $\mu < 0.3$. The boundaries of these bands, defined above on the basis of high (ratio ≥ 1.15), intermediate ($1.02 \leq$ ratio < 1.15) and low (ratio < 1.02) cloud impact, are collected in Table 5.1.

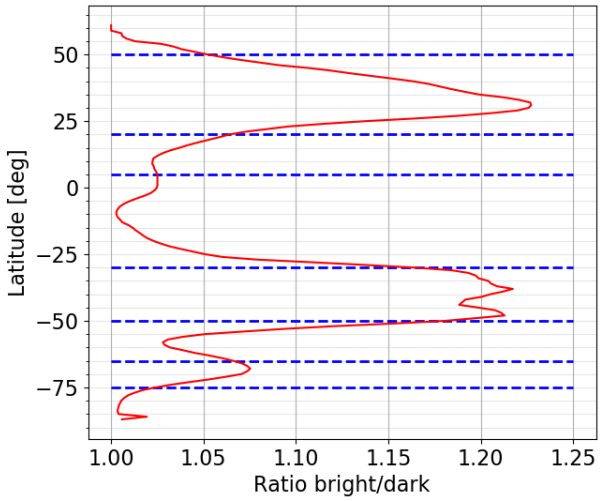

Figure 5.1: **Brightness ratio between bright and dark regions**. For each latitude, the points on the red curve represent the ratio between the brightness computed averaging all pixels at that latitude and the brightness of the same region with clouds removed, between 1996 and 2018. The rightward peaks represent bands where the impact of bright clouds is stronger. The dashed blue lines define the boundaries of the bands: these are specified in Table 5.1.

Southern boundary	Northern boundary	Brightness ratio
90°S	75°S	1.01
75°S	65°S	1.06
65°S	50°S	1.06
50°S	30°S	1.20
30°S	5°N	1.03
5°N	20°N	1.03
20°N	50°N	1.15

Table 5.1: Definition of latitudinal bands with corresponding boundaries.

	1994 – 2002		2004 – 2008		2015 – 2018	
Band	k (10^{-3})	σ_k (10^{-3})	k (10^{-3})	σ_k (10^{-3})	k (10^{-3})	σ_k (10^{-3})
90°S-75°S	4.38	0.77	−0.99	2.12	1.74	2.41
75°S-65°S	4.50	0.48	−1.71	1.63	0.05	2.37
65°S-50°S	6.76	0.84	0.60	0.92	1.55	1.93
50°S-30°S	8.14	0.69	1.23	1.27	2.00	2.66
30°S-5°N	3.68	0.39	1.34	0.87	−0.87	1.53
5°N-20°N	3.39	0.23	1.43	0.82	−2.76	4.72
20°N-50°N	5.50	0.99	0.78	0.80	−14.50	10.80

Table 5.2: Slopes of blue filter's linear fit for each band in the three time intervals we identified: 1994-2002, 2004-2008 and 2015-2018. k is the angular coefficient value of the fitting line, σ_k is the associated uncertainty.

5.2. Latitudinal results for F467M

The temporal evolution of reflectivity is investigated for the selected latitudinal bands. I/F values were extracted for the blue filter by averaging the pixels contained in a single band. Figure 5.2 reports the results in the blue filter. Three time intervals are identified, in which the whole period is divided: 1994-2002, 2004-2008 and 2015-2018.

For the 1994-2002 period, the increasing trend noticed in the disk-averaged data (see Figure 4.1) is reflected in all bands. The largest increase is registered at southern mid-latitudes, with bands at 65°S-50°S and 50°S-30°S, in which the growth amounts to 8.9% and 10.6%, respectively. The smallest increase is seen in near-equator latitudes (30°S-5°N and 5°N-20°N), with a 3.1-3.9% variation from 1994 to 2002. Near-polar regions (90°S-75°S and 75°S-65°S) and northern latitudes (20°N-50°N) show an intermediate growth, with variations of 5.7-5.9%. Data were linearly fitted in this time interval and the slopes of each segment were estimated to corroborate the reflectivity changing behavior, collected in Table 5.2 and visible in Figure 5.2, in order to visualize the data trend. These further confirm which bands are seen to display the largest change in I/F: southern mid-latitudinal bands have the largest coefficients, whereas near-equatorial regions have the lowest.

The results of our study are compared with previous studies for the 1994-2002 time period. The increasing brightness pattern agrees with Sromovsky et al. (2001d), who observed the largest difference between 1996 and 1998 to be in southern mid-latitudes (60°S-30°S) and the lowest around the equator (10°S-15°N) and near-polar regions (90°S-60°S). The fact that near-polar regions bands are seen to have an average behavior, rather than showing a minimum increase, is due to the extended timeline we are considering, ranging to 2002. If we were to consider only up to 1998, we see that in 1998 the I/F value indeed shows a slight drop for the southernmost bands.

Moreover, Sromovsky et al. (2001d) identified a dark band in 65°S-55°S, which we also see, as our roughly corresponding latitudinal band 65°S-50°S shows the minimum I/F value among all bands both in 1996 and 1998, namely $0.661^{+0.008}_{-0.008}$ and $0.680^{+0.008}_{-0.008}$. We also find a relatively bright region for our bands 50°S-30°S and 30°S-5°N, enclosing approximately the same region Sromovsky et al. (2001d) indicated as bright between 45°S and 5°N. They also identified a darker band north of 5°N, extending up to ~ 40°N, that corresponds to our northernmost bands (5°N-20°N and 20°N-50°N). We do not see a clear transition at the 5°N boundary.

Karkoschka (2011) made a study of the behavior of background reflectivity, spanning from 1994 to 2008. For our first (1994-2002) and second (2004-2008) time segments, he identified three bands: southern mid-

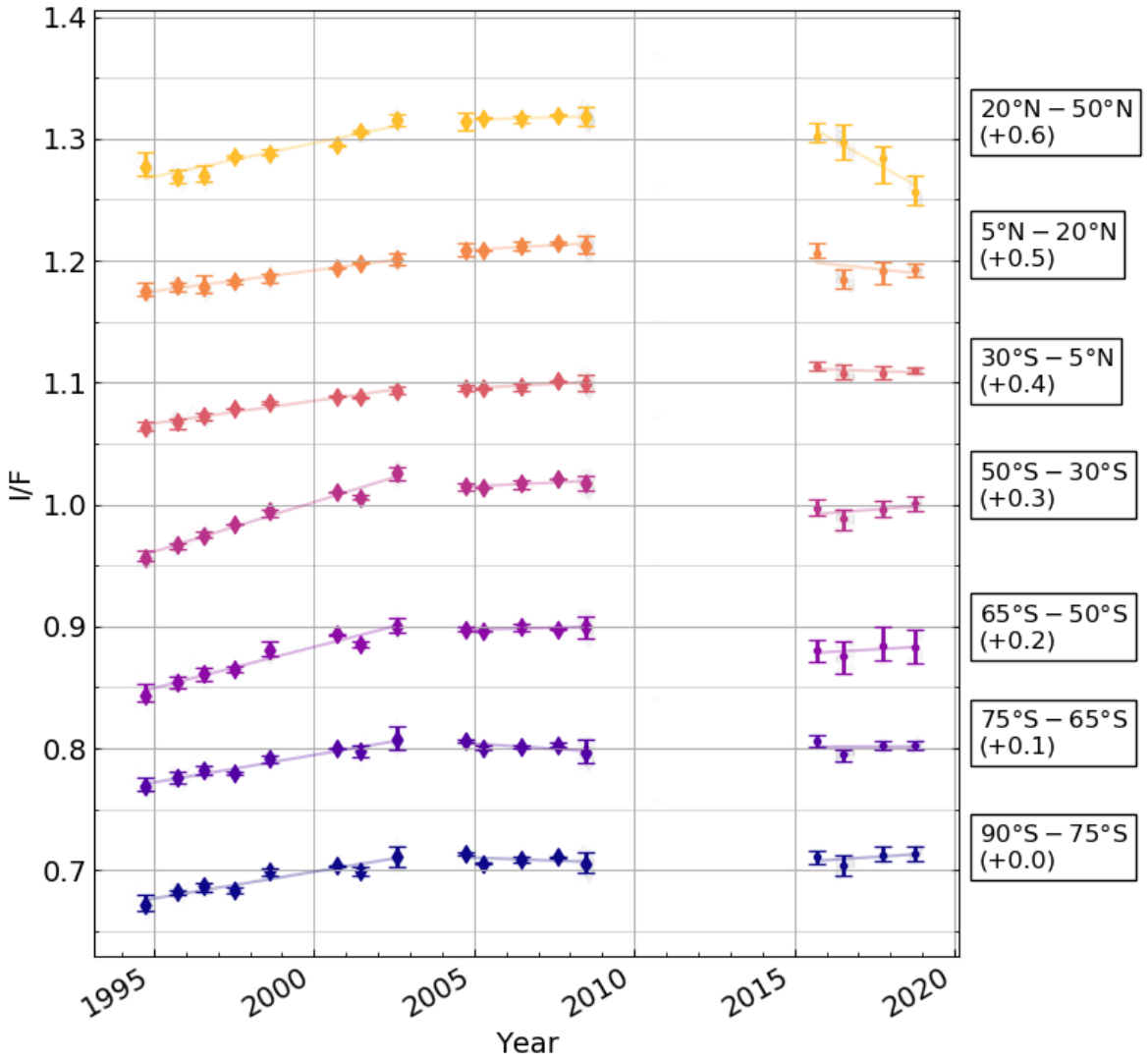

Figure 5.2: **Reflectivity temporal trend in the blue filter for latitudinal bands.** The I/F scale on the y-axis refers to the 90°S-75°S band. The other bands are shifted upwards as indicated on the right. The plotted error bars are computed as to enclose all values found for a specific year. The fainter straight lines represent our linear fits for the three time period we identified: 1994-2002, 2004-2008 and 2015-2018. Markers distinguish data from WFPC2 (diamonds) and WFC3 (circles).

latitudes (60°S-30°S), near-equatorial region (20°S-10°N) and higher northern latitudes (15°N-30°N). The temporal trend for his bands are plotted in his Figure 14, here reported in Figure 5.3. Southern mid-latitudes show the largest increase in reflectivity, in agreement with our findings for 65°S-50°S and 50°S-30°S bands, overlapping Karkoschka (2011)'s band. He fitted the increasing trend with a constant minus an exponential decay function (see Equation 2.1), noticing a progressive decrease in the growth of the I/F values. However, he performed the fit for the whole 1994-2008 period, whereas we break it down in two distinct segments, favoring for each segment a more simple linear trend. Close to the equator, the defined region is shifted northward with respect to our 30°S-5°N, which we acknowledge to be the slowest changing reflectivity band: this is also true for Karkoschka (2011)'s band, with respect to his other two latitudinal bands. His northernmost band shows an intermediate growth rate and it is included in our 5°N-20°N and 20°N-50°N bands, who also display an average increase rate. Furthermore, he noticed a north-south asymmetry: the change in reflectivity is larger for the southern hemisphere latitudes with respect to the northern. The angular coefficient for band 5°N-20°N is indeed the lowest, but this is not the case for band 20°N-50°N. Nonetheless, his northern boundary was set to 30°N, and thus what we obtain can still agree with his observation, as two-thirds of our northernmost band are not explored by this author.

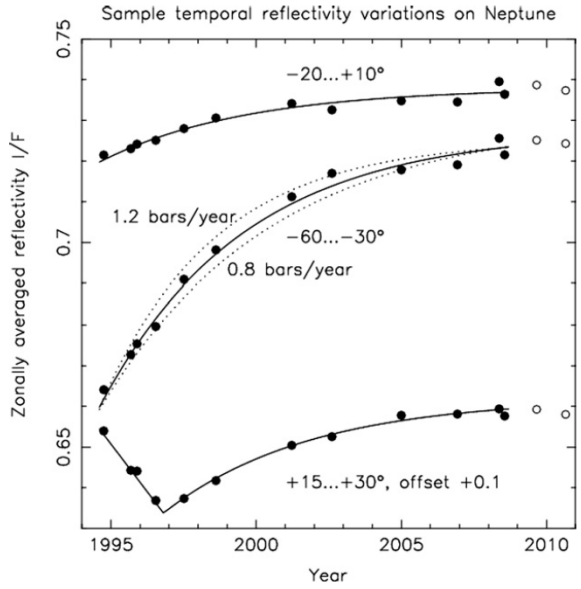

Figure 5.3: **Karkoschka (2011)'s reflectivity temporal trend in the blue filter for latitudinal bands.** The author considered three bands: southern mid-latitudes (60°S-30°S), near-equatorial region (20°S-10°N) and higher northern latitudes (15°N-30°N). I/F scale on the y-axis refers to the two southernmost bands, whereas the northern latitudes band reflectivity is shifted upwards by 0.1. The black points are observations, the black lines are exponential decay fits. The years covered by the exponential fit are between 1994 and 2008. White points report WFC3 measurements after 2008, dotted lines are radiative transfer modeling fits for hazes settling to deeper pressures at the rate labeled. The image displays Figure 14 from Karkoschka (2011).

In the 2004-2008 period, we observe an overall different behavior with respect to the earlier years. We linearly fitted the data points and the resulting parameters of the fitting function are reported in Table 5.2. Overall, most bands show a constant value, within the plotted error bars, as shown in Figure 5.2. Nonetheless, as indicated by our fitting parameters, the low-latitudes regions (30°S-5°N and 5°N-20°N) are consistent with an increasing trend, due to the small error bar for years 2005 and 2007.

In Karkoschka (2011) (Figure 5.3), the southern mid-latitudes appear to be constant after the 2002 data point: the three values between 2002 and 2007 seem to be aligned with 0.715. Nonetheless, an appreciable higher value is displayed for data in 2008, although no error bars were provided to assess whether this is a real increase. For the other northern bands, data after 2002 seem to grow in I/F, more clearly for 15°N-30°N than for 20°S-10°N, in agreement with our hypothesis of increasing trend for our 30°S-5°N and 5°N-20°N bands.

Karkoschka and Tomasko (2011) also analyzed the latitudinal structure from HST-STIS visible data, collected in 2003, a year we are missing from our WFPC2 set. Nonetheless, we can still compare our 2002 and 2004 with what they saw. They identified 8 bands. Their 74S is approximately covered by the upper part of our 90°S-75°S band and the lower part of our 75°S-65°S band. Their 45S band is enclosed in the lower half of our 50°S-30°S band. Their 6N band is centered at the boundary of our 30°S-5°N and 5°N-20°N bands. From their Figure 9, here reported in Figure 5.4, we gather that these bands are the brightest with respect to the other five bands. The three local maxima shown are contained in our 90°S-75°S, 50°S-30°S and 5°N-20°N. We agree with this result, as we also find the highest average I/F in both 2002 ($0.712^{+0.008}_{-0.008}$, $0.726^{+0.006}_{-0.005}$ and $0.701^{+0.005}_{-0.005}$, respectively) and 2004 ($0.714^{+0.001}_{-0.001}$, $0.715^{+0.003}_{-0.003}$ and $0.709^{+0.005}_{-0.005}$, respectively) to be for these bands. Nonetheless, we also find the northernmost band to be among the brightest ($0.716^{+0.005}_{-0.005}$ for 2002 and $0.714^{+0.007}_{-0.007}$ for 2004), but its extent goes beyond Karkoschka and Tomasko (2011) north boundary at 30°N. A peculiar dark band is found to be centered at ~ 60°S, which would have been roughly at the boundary of our 75°S-65°S and 65°S-50°S bands. Its presence is captured by the lower I/F values we register for the latter band, which are effectively a local minimum in 2002 ($0.700^{+0.005}_{-0.007}$) and the absolute minimum for 2004 ($0.698^{+0.001}_{-0.001}$) with respect to all other bands. Between the boundaries of our near-equatorial 30°S-5°N band, an average behavior is displayed in 2003. Nonetheless, in this band we detect the minimum reflectivity for both 2002 ($0.693^{+0.004}_{-0.002}$) and 2004 ($0.696^{+0.003}_{-0.003}$). The discrepancy might be due to events in 2003 we do not see because of the gap we have in our dataset.

The 2015-2018 period is marked by stability for southern hemisphere's bands and more dramatic changes

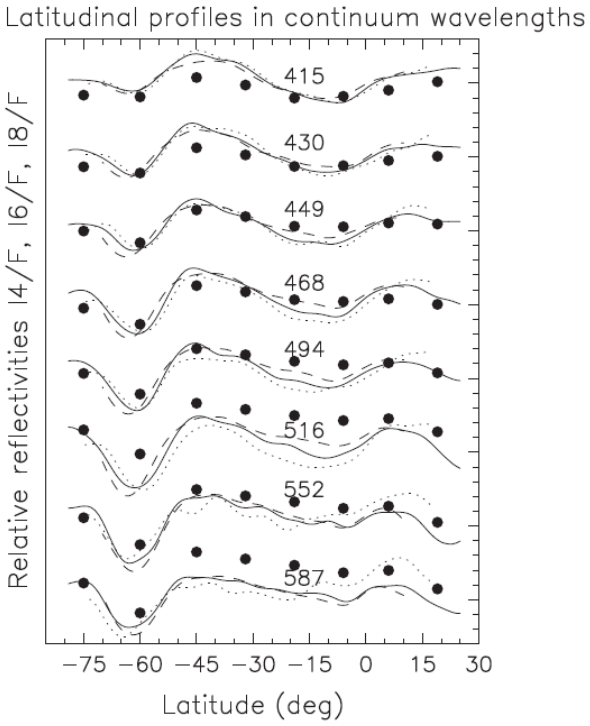

Figure 5.4: **Karkoschka and Tomasko (2011)'s reflectivity in the blue filter for latitudinal bands in 2003.** The authors considered eight bands, centered at latitudes where dots are plotted. We are interested in the dashed line for λ = 468 nm, representing the observed (latitudinal) trend from the blue filter for an emission angle cosine μ = 0.8. For a description of all other symbols and lines, not needed for the comparison made with this work, refer to Figure 9 in Karkoschka and Tomasko (2011).

for the northern. The extracted parameters of our linear fits are collected in Table 5.2. As the k values can be either positive, negative or null, the trends we see are consistent with either increasing, decreasing or constant behavior. The only exception is noticed for the northernmost band at 20°N-50°N, where we record a 6.5% decrease. The cause of this drop could be related to the appearance of a dark vortex in the northern hemisphere of the planet (Simon et al., 2019). It would also give reason to the greater spread of data in these years: the appearance (lower extent of error bar) and disappearance (upper extent of error bar) of the vortex on the planetary disk would cause fluctuations on a time scale similar to the rotational rate of the vortex itself. We also observe a drop in the 2016 data point for bands 75°S-65°S and 5°N-20°N, whose difference with respect to 2015 is larger than the extent of error bars. We do not have literature regarding the latitudinal trends in this recent period, as we do for the previous two time intervals. Hence, we add these new years to Neptune's latitudinal analysis.

5.3. Latitudinal results for F850LP and F845M

The same latitudinal bands were adopted as described in Section 5.1 (Table 5.1). The I/F values were computed as average of pixels in the considered band. For the methane filters, we also applied the cloud removal technique (Appendix A). Figure 5.5 shows our results in these filters. We used a similar time interval division to analyze data and linearly fit them, to highlight possible increasing or decreasing patterns. The starting year is 1996 in this case, as we do not have measurement prior to it in these filters. We considered the intervals 1996-2002, 2009-2011 and 2015-2018.

From 1996 to 2002, an increase in I/F is observed for southern mid-latitudes, i.e. 65°S-50°S and 50°S-30°S. We record a growth of 10.2% and 16.2%, respectively. An increasing behavior is also seen for the northern hemisphere, for bands 5°N-20°N (11.1%) and 20°N-50°N (12.3%). The other bands are consistent with a constant trend, within the extent of error bars. The linear fit of each band's data is also plotted in Figure 5.5. Since the fit was done with a small number of points (less than 4), we used the z-test to test the hypothesis of no change between the data points at the boundaries of each time interval. The results of the z-test for each band are listed in Table 5.3. When $|z| > 1.7$ (numbers in bold), the hypothesis is not statistically significant for

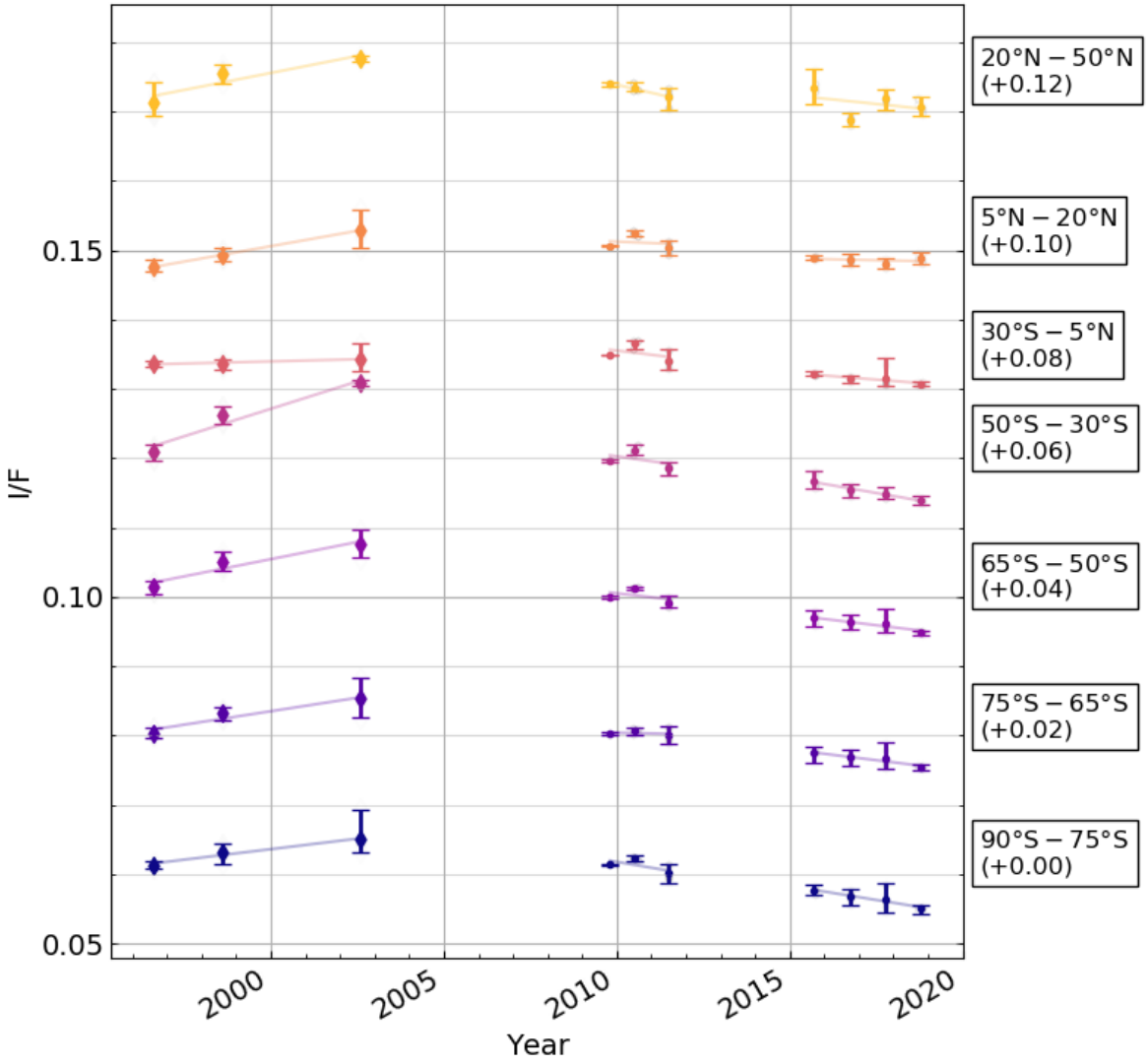

Figure 5.5: **Reflectivity temporal trend in the methane filter for latitudinal bands.** The I/F scale on the y-axis refers to the 90°S-75°S band. The other bands are shifted upwards as indicated on the right. The plotted error bars are computed as to enclose all values found for a specific year. The fainter straight lines represent our linear fits for the three time period we identified: 1996-2002, 2009-2011 and 2015-2018. Markers distinguish data from WFPC2 (diamonds) and WFC3 (circles).

probabilities $p < 0.05$, hence a changing behavior is most likely occurring.

Comparing our results with other studies, we see that Sromovsky et al. (2001d) provided a comparison between 1996 and 1998 for all latitudes in their Figure 9, here displayed in Figure 5.6. From it, they registered the largest relative variation to be in the northern hemisphere, between 20°N-40°N. This is in line with our findings, as we also find the greatest 1996-1998 change in our 20°N-50°N band, but this does not reflect the overall behavior up to 2002. The other most changing region is around 25°S, enclosed in our 30°S-5°N, in which we do not see a remarkable growth between 1996 and 1998, perhaps due to the extent of the band, that includes also most of the average behavior region that was seen in 20°S-15°N. Two minor bumps are seen within 65°S-50°S, matching our latitudinal band in this region, in which we also see a change larger than error bars on data. Sromovsky et al. (2001d) found negligible changes for south polar regions, corresponding to our 90°S-75°S and 75°S-65°S bands. The latter band agrees with their findings, whereas the former displays an appreciable increase. These minor discrepancies are generated from the different selection of dark regions for the analysis: Sromovsky et al. (2001d) looked at longitudes between 75°W and 125°W, whereas we look at all pixels of cloud-removed images, not fixed to a certain longitudinal range.

Karkoschka (2011) provided also a temporal evolution in the methane filter for the 1996-2002 period. In

Band	1996 – 2002	2008 – 2011	2015 – 2018
90°S-75°S	−1.23	0.93	**2.58**
75°S-65°S	−1.66	0.10	**1.74**
65°S-50°S	**−2.81**	0.86	1.63
50°S-30°S	**−8.10**	1.14	**1.92**
30°S-5°N	−0.33	0.57	**2.85**
5°N-20°N	**−1.78**	0.17	0.20
20°N-50°N	**−2.56**	1.19	0.94

Table 5.3: z-test values for methane filter's boundaries I/F values for each band in the three time intervals we identified. The bold values are associated with non significant differences for probability $p < 0.05$, meaning that the time interval is consistent with changing behavior.

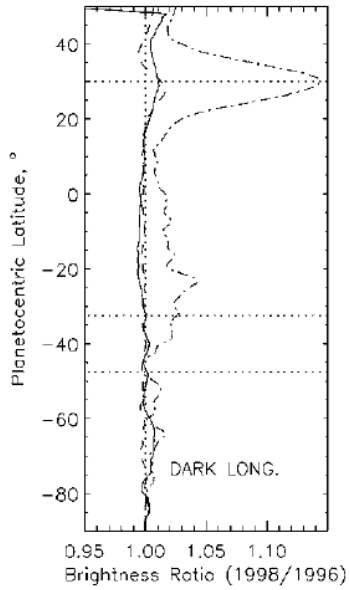

Figure 5.6: **Sromovsky et al. (2001d)'s reflectivity changes between 1996 and 1998 in the F850LP filter for latitudinal bands.** The authors plotted the ratio between the two years for dark cloud-free regions. The y-axis represents latitude, the x-axis the I/F ratio. We are interested in the dotted-dashed line, which refers to the methane filter. The other lines refer to blue (F467M) and F673M filters. The image displays Figure 9 from Sromovsky et al. (2001d).

his Figure 3, displayed in Figure 5.7, he reports the changes in the northern and southern half of the planetary disk, with and without clouds for the methane filters. The trend hints at a constant value throughout the years. The difference with our findings could be related to the different cloud removal implementation and latitudinal structure considered. We removed clouds with the evaluation of the yearly median of selected dark regions (Appendix A), whereas he considered specific lowest reflectivities. The selection of dark regions and low reflectivities is subject to the authors and might lead to different results. Moreover, we considered a more refined latitudinal band structure than Neptune's hemispheres. Since our cloud removal method is more similar to Sromovsky et al. (2001d)'s, this might explain our proximity to their findings, rather than to Karkoschka (2011)'s.

In the 2009-2011 period, we observe a peak in 2010 for all bands, with the exception of 75°S-65°S and 20°N-50°N, where the trend is consistent with no change over time within error bars, as we see also from the z-test values (Table 5.3). Nonetheless, linearly fitting data in this time interval results in a constant trend for all bands. In general, we notice a brighter southern hemisphere, with respect to the northern. We do not have a previous study to make a comparison with.

For the most recent 2015-2018, from Table 5.3, we observe a changing behavior for near-polar regions (90°S-75°S and 75°S-65°S) and southern mid- to low- latitudes (50°S-30°S and 30°S-5°N). This is seen also in Figure 5.5. In near-polar regions, the I/F value drops by 3.5-4.5%, whereas the latter changes by 2.6-4.9%. As for the 2009-2011 period, northern latitudes are darker than southern, with a maximum in reflectivity in the

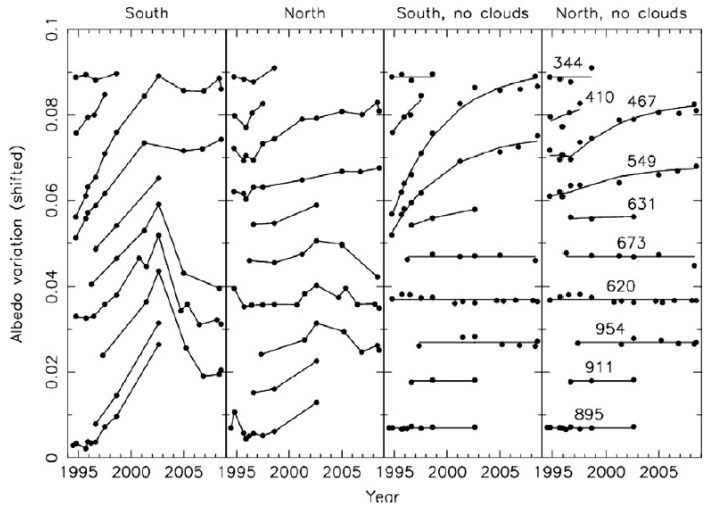

Figure 5.7: **Karkoschka (2011)'s albedo for northern and southern half of the disk in time.** The author divides the planetary disk in a north and south part, and analyzed the variation in time with and without clouds. We are interested in the fitted lines labeled as 911 (peak wavelength for F850LP) without clouds (right panels). The reflectivity indicated on the y-axis corresponds to a shifted I/F to offset the various filters reported. The years covered are between 1994 and 2008. The image displays Figure 3 from Karkoschka (2011).

near-polar regions. Northern hemisphere's bands (5°N-20°N and 20°N-50°N), as well as band 65°S-50°S, are consistent with a constant trend, as the extent of error bars for 2015 and 2018 have an overlap. A peculiar drop is noticed in 2016 for band 20°N-50°N. This might be related to the appearance of the northern dark spot seen in 2018 at 23°N, possibly anticipated by prior cloud activity (Simon et al., 2019) affecting the hazes' brightness. No other analogous analysis in our methane filters' wavelengths is available on this period to compare results with.

6

SUNBEAR radiative transfer code

The following Chapter treats the basics of radiative transfer (RT) theory and provides the definitions for the operations and input parameters used in the employed RT code. Radiation is the main energy transport mechanism acting in the upper troposphere and stratosphere (de Pater and Lissauer, 2011), i.e. the altitudes at which our visible wavelengths data allow to probe (Chapter 3). Understanding how sunlight interacts with atmospheric particles is crucial to model the structure and composition of a planetary atmosphere, as this allows us to infer conclusions based on remote sensing measurements.

The radiative transfer modeling in this work is performed with the Spectra from Ultraviolet to Near-infrared with the BErkeley Atmospheric Retrieval (SUNBEAR) code, written by S. H. Luszcz-Cook, J. Tollefson, M. Ádámkovics and K. de Kleer. This code has been used in previous solar system analyses for Titan, Uranus and Neptune itself (Ádámkovics et al., 2016; de Kleer et al., 2015; Luszcz-Cook et al., 2016; Molter et al., 2019). The algorithm is based on the DIScrete Ordinate method for Radiative Transfer (DISORT) developed by Stamnes et al. (1988). The idea of the method is to approximate the planetary atmosphere with multiple plane-parallel adjacent homogeneous layers, each having constant single scattering albedo and phase function, that are allowed to change among the different layers. In every layer, the radiative transfer equation is solved numerically.

The key definitions and equations of radiative transfer are introduced in Section 6.1, followed by assumptions and methods used to perform radiative transfer modeling. In order to have an accurate model of I/F after sunlight reflection on Neptune's atmosphere, several aspects are taken into account. First, the atmospheric structure has to be specified, in its temperature-pressure profile, chemical composition and vertical division into discrete layers (Section 6.2). Second, from the species present in the atmosphere, the gas opacity and Rayleigh scattering are computed, from the chemical constituents' absorption coefficients, abundances and optical properties (Section 6.3). Third, haze layers are introduced into the atmosphere and their impact in terms of single scattering albedo and optical depth is assessed from the scatterers properties, present in each haze layer (Section 6.4). Finally, once the total optical depth is estimated, corrections on the obtained reflectivities are implemented to account for Rayleigh polarization (Section 6.5) and Raman scattering (Section 6.6). In each Section, the relevant parameters are introduced and explained. Section 6.7 summarizes these parameters, used in the code, their meaning and from which reference were taken, if not considered as free parameters. In conclusion, Section 6.8 deals with parameter sensitivity, i.e. how the change of values for input parameters affects the output model spectrum.

6.1. Basic definitions and equations of radiative transfer

This Section briefly reports the definition of key concepts for radiation theory, necessary condition to describe the radiative transfer code operations later on (Sections 6.2-6.6). The equations presented are taken from Rybicki and Lightman (2004), if not otherwise indicated.

6.1.1. Flux density

The flux density is defined as the brightness B_ν of an object multiplied by the subtending solid angle Ω considered:

$$F_\nu = \Omega B_\nu(T) \tag{6.1}$$

The flux density has units of W m^{-2} Hz^{-1}, meaning that it represents the flux for a given wavelength range. The flux density defined in Equation 6.1 is used for the computation of I/F values, as F_N and $F_\odot$ in Equation 3.1.

6.1.2. Specific intensity

The specific intensity is one of the terms that are present in the equation of radiative transfer. It is defined as follows:

$$I_\nu = \frac{dE}{dA\cos\theta\, dt\, d\Omega\, d\nu} \tag{6.2}$$

where dE is the amount of energy passing through the differential element of area $dA\cos\theta$, being θ the angle between the direction of propagation of the radiation and the normal direction with respect to dA, in the time interval dt and frequency range $d\nu$ throughout the solid angle $d\Omega$. Therefore, units for the specific intensity are W m^{-2} s^{-1} sr^{-1} Hz^{-1}, alternatively the energy per unit area per unit time per direction per wavelength. The scenario is depicted in Figure 6.1. For a blackbody, the specific intensity corresponds to the brightness $B_\nu(T)$.

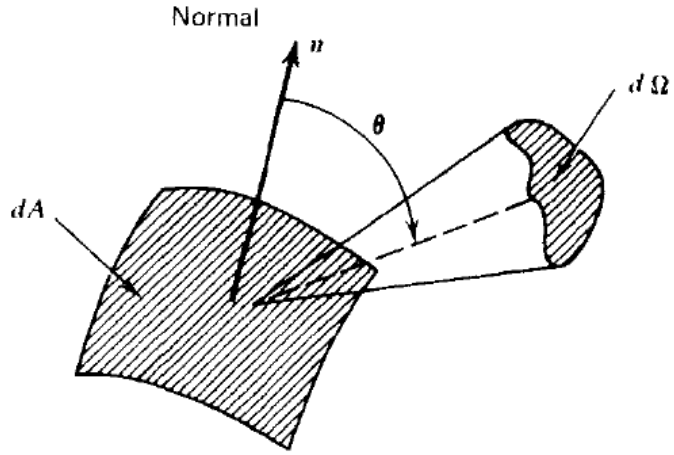

Figure 6.1: **Geometry for incident energy.** The angle θ is defined from the direction of the surface's normal (**n**) and the direction of the rays. The solid angle $d\Omega$ encloses the specific intensity calculated in Equation 6.2. The image is taken from Rybicki and Lightman (2004).

6.1.3. Radiative transfer

The description of energy transport by means of radiation is affected by several phenomena occurring as a result of interaction between incident light and particles present in the atmosphere. These are emission, absorption and scattering, hereby introduced, which are responsible for specific intensity's variation. The wavelength region examined (0.3-1.0 μm) does not contain thermal emission, so that the formulation of the radiative transfer equation includes only absorption and scattering, and emission is not treated.

Absorption

Whereas emission causes an increase in the energy transported by means of radiation, absorption has an opposite effect, decreasing the beam's energy. To find an analytical expression of the energy loss, we consider a beam with cross-section dA, traveling a distance ds, containing randomly distributed absorbing particles with density N and cross-section σ. The absorbed energy from the beam within a solid angle $d\Omega$ is given by

$$-dI_\nu\, dA\, d\Omega\, dt\, d\nu = I_\nu\,(N\sigma\, dA\, ds)\, d\Omega\, dt\, d\nu \tag{6.3}$$

The term into brackets on the right-hand side is the absorbing area of the particles in the beam. Simplification yields to

$$dI_\nu = -N\sigma\, I_\nu\, ds \tag{6.4}$$

We can define an absorption coefficient $\alpha_\nu = N\sigma$, also expressed as

$$\alpha_\nu = \rho\kappa_\nu \tag{6.5}$$

where ρ is the mass density (kg m^{-3}) and κ_ν is known as mass absorption coefficient or opacity coefficient (m^2 kg^{-1}). α_ν is thus expressed in terms of m^{-1}.

Hence, Equation 6.4 can be rewritten as

$$dI_\nu = -\alpha_\nu I_\nu ds \tag{6.6}$$

which represents the loss of intensity for a beam with specific intensity I_ν travelling for a distance ds.

As noted in Rybicki and Lightman (2004), Equation 6.6 holds if the cross-section of the particles is small in comparison to the distance between the particles themselves, and if these are randomly distributed and independent. These two conditions are generally verified in astrophysical scenarios, such as in planetary atmospheres.

Scattering

When traveling in vacuum, electromagnetic radiation propagates without being modified in its characteristics. This condition is not verified when sunlight hits a planetary atmosphere, as the beam encounters aerosols and clouds layers that absorb energy and redirect the incoming flux, changing both its direction of propagation and its polarization state. The redirection is referred to as scattering. The effects of scattering are dependent on the particles size, morphology and composition, wavelength and polarization state of light, so that it provides a useful tool for remote sensing characterization of atmospheres on planets (Mishchenko et al., 2015).

Scattering contributes to the variation of specific intensity. Particles hit by the electromagnetic wave absorb the energy of the incident ray and re-radiate it in all direction. The variation of specific intensity caused by scattering follows the same laws seen for absorption. Scattering is already included in Equation 6.6, in which the absorption coefficient accounts for it. As explained in de Pater and Lissauer (2011), α_ν is the sum of the contributions given by scattering and absorption: $\alpha_\nu = \alpha_\nu(\text{absorption}) + \alpha_\nu(\text{scattering})$. Hence, the analytical expression of the contribution to radiative transfer by absorption remains the same as in Equation 6.6, in which scattering is included in the coefficient as explained.

The scattering coefficient is indicated as σ_ν (previously called $\alpha_\nu(\text{scattering})$). This allows for the definition of the single scattering albedo as

$$\omega_\nu = \frac{\sigma_\nu}{\alpha_\nu} \tag{6.7}$$

which represents the fraction of radiation lost because of scattering, with α_ν the total extinction coefficient, sum of scattering and absorption coefficients.

Depending on the direction in which scattered radiation is propagated after interaction with particles, forward scattering or back scattering can take place. The former occurs when the scattering angle Θ, i.e. the angle between the direction of the incoming ray (x-axis, oriented from the light source to the scattering medium) and the direction of the scattered ray, is smaller than 90°: light continues to move in a forward direction, with increasing x component. If $\Theta \geq 90°$, the x component of light's motion decreases or stays constant. The simplest case is isotropic scattering, i.e. when scattered light is redirected uniformly in all directions. In the anisotropic case, where there are preferential directions of propagation, the angular dependency of scattered light is represented by a phase function $p(\cos\Theta)$. A simple analytical approximation was introduced by Henyey and Greenstein (1941), which will be introduced later on (Section 6.4).

Depending on the size of the particles responsible for scattering with respect to the wavelength of the incoming radiation, a different description of the scattering phenomenon is provided. In fact, the larger the particle is, the more the scattered light is concentrated in the forward direction, whereas smaller particles have a more balanced scatter in both forward and backward direction. Rayleigh (Section 6.3) and Mie scattering theories provide analytical relations considering the scattering mechanism as elastic. The inelastic case is treated in Raman's scattering theory (Section 6.6).

The radiative transfer equation

Considering scattering already included in absorption and emission, responsible for the variation of the specific intensity, the general radiative transfer equation comes from the sum of two contributions (Equation 6.6 for absorption) and can be formalized as

$$dI_\nu = j_\nu ds - \alpha_\nu I_\nu ds \tag{6.8}$$

with j_ν the emission coefficient. The angle that the direction of sight **s**, i.e. the target-observer direction, forms with the normal to the target's surface **z** is the emission angle ϑ, so that $ds = dz/\cos\vartheta$. Hence, defining $\mu = \cos\vartheta$ gives

$$\mu \frac{dI_\nu}{dz} = j_\nu - \alpha_\nu I_\nu \tag{6.9}$$

Looking at visible wavelengths, where no thermal emission is present, allows to neglect the emission term ($j_\nu = 0$), so that only absorption is taken into account.

The solution of Equation 6.9 is straightforward for only absorption (Rybicki and Lightman, 2004):

$$\mu \frac{dI_\nu}{dz} = -\alpha_\nu I_\nu \tag{6.10}$$

Applying the separation of variables method brings to the solution

$$I_\nu = I_\nu(s_0)\, e^{-\int_{z_0}^{z_1} \frac{\alpha_\nu(z)}{\mu} dz} \tag{6.11}$$

The specific intensity decreases exponentially with the absorption coefficient integrated along direction **z**.

A simpler form of the transfer equation is obtained with the introduction of the optical depth τ_ν, defined as

$$d\tau_\nu = \alpha_\nu\, dz \Longrightarrow \tau_\nu = \int_{z_0}^{z_1} \alpha_\nu(s) dz \tag{6.12}$$

The numerical value of τ_ν determines whether the considered medium is optically thick ($\tau_\nu > 1$) or thin ($\tau_\nu < 1$). Substituting the optical depth in the radiative transfer equation gives

$$\mu \frac{dI_\nu\, \alpha_\nu}{d\tau_\nu} = -\alpha_\nu I_\nu \tag{6.13}$$

Dividing by the absorption coefficient yields to

$$\mu \frac{dI_\nu}{d\tau_\nu} = -I_\nu \tag{6.14}$$

The analytical solution is the so called formal solution of the transfer equation for only absorption:

$$I_\nu(\tau_\nu) = I_\nu(0)\, e^{-\tau_\nu/\mu} \tag{6.15}$$

known as Bouguer-Beer-Lambert's exponential absorption law (de Pater and Lissauer, 2011).

6.2. Atmosphere layers, temperature and composition setup

The first operation that SUNBEAR performs is to build the atmospheric model in its layered structure, temperature-pressure profile and gas composition.

From the maximum ($P_{\text{max,atm}}$) and minimum ($P_{\text{min,atm}}$) pressure values in which the atmosphere is analyzed, input by the user, the code splits the atmosphere into several discrete layers, following a logarithmic division and computing the upper and lower pressure boundaries for each of them. The number and extension of these discrete layers can be specified. In addition to $P_{\text{max,atm}}$ and $P_{\text{min,atm}}$, it is possible to set a reduced sub-interval where discrete layers have a higher resolution, i.e. are less extended in terms of pressure. This improves the accuracy of calculations, as the discretization is more refined (more numerous and narrower layers are considered), better approximating the real atmospheric structure the more heterogeneous it is. Outside this interval, a coarse discretization is adopted, i.e. discrete layers are thicker and further from reality. The refined sub-interval will include pressure levels of interest, e.g. altitudes where we want to model clouds or aerosols, whereas the coarse regions are for altitudes we are not focusing on. With this method, computational time is reduced, as lower resolution altitudes contain less layers for which radiative transfer calculations are done.

In this study, we set $P_{\text{max}} = 25$ bar and $P_{\text{min}} = 10^{-5}$ bar. The refined sub-interval we considered is between $P_{\text{max,ref}} = 20$ bar and $P_{\text{min,ref}} = 10^{-2}$ bar, where the extension of discrete layers is defined to be 0.075 in logarithmic space. This means that, setting $P_{\text{min},n}$ the n$^{\text{th}}$ layer's pressure upper boundary, the n+1$^{\text{th}}$ layer

extends between $P_{\min,n}$ and $P_{\min,n+1} = P_{\min,n} \cdot e^{-0.075}$. An analogous approach is implemented for the coarse pressure levels, where the logarithmic factor is set to 0.5, such that $P_{\min,n+1} = P_{\min,n} \cdot e^{-0.5}$.

Subsequently, the code imports a temperature-pressure profile from previous literature. As in Luszcz-Cook et al. (2016), we used the stratospheric and the tropospheric temperature structure proposed by Fletcher et al. (2014), deduced from thermal infrared measurements taken with Keck Long Wavelength Spectrometer (LWS) in 2003. The profile allows to determine the temperature at discrete pressure levels, which serves to deduce the state of chemical species present in the atmosphere.

Indeed, to complete the atmospheric model, its composition is specified by the user. The input requires the gaseous species present, which one is the main component of the atmosphere, whether they are well-mixed throughout the atmosphere and their molecular mass in atomic mass units (amu). Following Luszcz-Cook et al. (2016), four main components are identified: hydrogen (H_2), helium (He), nitrogen (N_2) and methane (CH_4). The dominant species is H_2, followed by He: we adopted the He/H_2 ratio of 0.15/0.847, in agreement with Conrath et al. (1993). The volume mixing ratio of nitrogen was fixed to 0.003. Whereas those ratios were kept constant along pressure levels, the methane abundance was modeled as a function of depth. The model was created from the methane mixing ratio in the deep troposphere ($X_{CH_4,t}$) and the maximum stratospheric CH_4 abundance ($X_{CH_4,s}$), input by the user. The volume mixing ratio quantifies the amount of methane present in a certain atmospheric layer, defined as the ratio between the number of particles of the considered species (CH_4 in our case) in a specified volume, i.e. the number density, and the number density of all constituents in the same volume. Analytically:

$$X_k = \frac{N_k}{\sum_{i=1}^{n} N_i} \tag{6.16}$$

with N_k the k$^{\text{th}}$ gas' number density and n the number of different gases in the air mixture (Chamberlain and Hunten, 1989). The deep tropospheric and maximum stratospheric CH_4 mixing ratios set the boundaries of the methane abundance variability: it cannot be higher than $X_{CH_4,t}$ below (at deeper altitudes than) its condensation pressure level, nor higher than $X_{CH_4,s}$ above (at higher altitudes than) this level. X_{CH_4} is allowed to decrease with decreasing pressure (increasing altitude) until its condensation level, where its mixing ratio will be minimum. We assumed that the relative humidity is constantly equal to 1. At higher altitudes with respect to the methane condensation pressure level, the mixing ratio increases again up until $X_{CH_4,s}$, following the saturation vapor pressure curve, parameterized as in Luszcz-Cook et al. (2016).

6.3. Gas opacity

After the setup of the atmosphere, the routine proceeds to compute the optical depth of each discrete layer due to gas opacity. The contribution to optical depth varies between the various species composing the atmosphere (Section 6.2) and their compounds. The considered source of opacity are CH_4, H_2, H_2CH_4, H_2H_2 and H_2He. The impact that these compounds have on the opacity of the single discrete layer depends on molar fraction, density, column abundance and absorption coefficient. All these parameters are evaluated in the discrete layer's temperature-pressure conditions.

The absorption coefficients are referred to as k-coefficients, collected in dedicated k-tables. k-coefficients are not only dependent on the temperature and pressure conditions of the considered layer, but also on wavelength intervals. Hence, k-tables contain k-coefficient for every combination of temperature-pressure and wavelength. k-tables are present in literature (Karkoschka, 1994, 1998; Karkoschka and Tomasko, 2010; Sromovsky et al., 2012). The adopted methane absorption coefficients were taken from Karkoschka and Tomasko (2010) for wavelengths 0.3-0.518 μm, and from Sromovsky et al. (2012) for 0.518-1.0 μm. For H_2CH_4, H_2H_2 and H_2He, the same references as Luszcz-Cook et al. (2016) were used.

The dependence of the optical depth τ_i of a given layer i due to a specific molecule C, formed by species $c1$ and $c2$, is formalized as follows (Luszcz-Cook et al., 2016):

$$\tau_i = k_{C,i} \cdot \mathrm{MF}_{c1,i} \cdot \mathrm{MF}_{c2,i} \cdot \mathrm{col}_{C,i} \cdot \mathrm{den}_{C,i} \tag{6.17}$$

where $k_{C,i}$ is the absorption coefficient of the compound C in the i$^{\text{th}}$ layer's temperature-pressure conditions, den is the density in the i$^{\text{th}}$ layer in units of amagat, i.e. particles per unit of volume at standard pressure and temperature conditions (P = 1 atm and T = 273.15 K), and col is the column abundance (km-amagat) of C. MF is the molar fraction of species $c1$ or $c2$ in the i$^{\text{th}}$ layer, defined as:

$$\mathrm{MF_k} = \frac{\mathrm{mol_k}}{\mathrm{mol_{tot}}} \tag{6.18}$$

where mol_k is the amount, in moles, of the k^{th} species and $\text{mol}_{\text{tot}} = \sum_k^N \text{mol}_k$ the total amount of all chemical species, again in moles. By definition, the sum of all mole fractions is 1. Equation 6.17 is implemented for all considered wavelengths in the 0.3-1.0 μm range.

In the visible range considered, Rayleigh scattering is dominant in Neptune's atmosphere (Sromovsky, 2005), so that, to have an accurate model of reflectivity, this phenomenon has to be accounted for. The code computes the scattering extinction coefficient from Rayleigh theory. Analytically, for a given discrete layer and at wavelength λ, this is expressed as follows (Luszcz-Cook et al., 2016):

$$k_R = \frac{24\pi^3}{\lambda^4} \cdot \frac{N}{N_0^2} \sum_i \left(\text{MF}_i \cdot \left(\frac{n_i^2 - 1}{n_i^2 + 2} \right)^2 \cdot \frac{6 + 3\delta_i}{6 - 7\delta_i} \right) \tag{6.19}$$

where λ is wavelength in cm, N is the number density (amagat) in the layer, $N_0 = 2.687 \cdot 10^{19}$ cm^{-3} (= 1 amagat) is Loschmidt's number, MF_i is the molar fraction of species i, n_i its refractive index and δ_i its depolarization factor. δ_i describes the effect of molecular anisotropy (Bucholtz, 1995). k_R is computed for each layer, and all contributions are summed up to give the total Rayleigh scattering coefficient. N is essentially the den parameter converted from amagats to cm^{-3} by multiplication with N_0. For the refractive index, we adopted Luszcz-Cook et al. (2016) parameterization:

$$n = 1 + A \cdot \left(1 + \frac{B}{\lambda^2} \right) \tag{6.20}$$

with λ expressed in μm, A and B parameters empirically determined from the molecule considered. Similarly, the depolarization factor is empirically defined for each molecule. A, B and δ were set equal to Luszcz-Cook et al. (2016)'s (see Table 6.2).

Finally, the contribution to optical depth due to Rayleigh scattering follows Equation 6.12, with the absorption coefficient equal to k_R. The total optical depth due to gas at a certain wavelength is thus given by the sum of gas opacity contribution (Equation 6.17) and Rayleigh contribution (Equation 6.12 with $\alpha_\nu = k_R$ from Equation 6.19). In DISORT, having discrete layers with constant absorption coefficient, the integral in Equation 6.12 becomes:

$$\tau_\nu = \int_{z_0}^{z_1} \alpha_\nu(z) dz = \alpha_\nu(z)\, z \tag{6.21}$$

with $z = z_1 - z_0$ the layer's thickness.

6.4. Aerosols modeling

In the defined discretized atmosphere, characterized by its optical depth per wavelength according to its chemical composition, the code allows for the introduction of hazes and clouds structures in the model. In this work, two haze layers were inserted, as done in Luszcz-Cook et al. (2016): the upper and lower haze layer are hereafter referred as α and β. The physical parameters that can be chosen for each layer are several. From them, the modeling of the discrete layers is done, i.e. how the aerosol properties are retrieved for each layer per wavelength and how these affect the overall optical depth of the atmosphere.

The physical properties of each haze's molecules responsible for scattering (hereafter *scatterers*) are determined through the single scattering albedo (ω), phase function parameters (f, g_1, g_2) and extinction cross section (σ). All these quantities are usually dependent on wavelength, so that they are evaluated for λ in the analyzed interval (0.3-1.0 μm in this case). Nonetheless, it is also possible to approximate them to be independent from λ.

As seen in Section 6.1, ω represents the fraction of radiation lost due to scattering. This parameter can be set to a constant value (as in both haze layers in Luszcz-Cook et al., 2016) or can be modeled as dependent on wavelength (as in Karkoschka and Tomasko, 2011's tropospheric haze). In this work, a constant value was used for the upper haze layer scatterers and a spectral dependence for the lower haze layer molecules was adopted, following Karkoschka and Tomasko (2011). The single scattering albedo was considered to be free while looking for the best fitting model, retrieving the values and expressions presented in Section 7. It is specified that this single scattering albedo is a property of the molecules of the aerosol, and not of the aerosol layer itself. The total single scattering albedo of the modeled atmosphere is computed starting from ω and the other physical and positional properties of aerosols, as it will be seen shortly.

The phase function parameters are modeled according to the expression proposed by Irvine (1968), i.e. the so-called double Henyey-Greenstein phase function. The Henyey-Greenstein phase function (Henyey

and Greenstein, 1941) was introduced as an analytical approximation of the angular dependence of anisotropic scattered radiation. The expression of the phase function $p(\cos\Theta)$ is

$$p(\cos\Theta) = \frac{1}{4\pi}\frac{1-g^2}{(1+g^2-2\,g\cos\Theta)^{3/2}} \tag{6.22}$$

where Θ is the scattering angle, i.e. the angle between the scattered and incident radiation, and g the asymmetry parameter, such that $-1 \leq g \leq 1$. Three notable cases are $g = -1$ (complete back-scattering, $\Theta = \pi$), $g = 0$ (isotropic scattering, $p(\cos\Theta)$ = constant) and $g = 1$ (complete forward scattering, $\Theta = 0$). For $g < 0$, back-scattering dominates, whereas for $g > 0$ forward scattering is predominant.

If, on the one hand, Equation 6.22 reproduces well the forward and back-scattering scenarios, on the other it fails to include both a forward and backward scattering case in a single phase function (Goody and Yung, 1995). To account for this, Irvine (1968) introduced the double Henyey-Greenstein phase function, defined as

$$\Phi(\cos\Theta) = f\,p(\cos\Theta, g_1) + (1-f)\,p(\cos\Theta, g_2) \tag{6.23}$$

where $0 < f < 1$ is the forward scattering function fraction, g_1 and g_2 are factors to define the back-scattering peaks: the three parameters are known as the double Henyey-Greenstein parameters. Setting $g_1 > 0$ and $g_2 < 0$ allows the phase function $\Phi(\cos\Theta)$ to have a forward ($p(\cos\Theta, g_1)$) and a backward ($p(\cos\Theta, g_2)$) scattering part. With $f = 0$, Equation 6.23 reduces to Equation 6.22.

We used Equation 6.23, defining parameters f, g_1 and g_2. These values were adopted from Karkoschka and Tomasko (2011), since they also perform radiative transfer to fit visible wavelengths, and their spectral dependence and constant values are fixed to:

$$f = 0.7 \tag{6.24}$$

$$g_1 = 0.725 - 0.075\sin\left(\frac{\lambda - 680}{2}\right) \tag{6.25}$$

$$g_2 = -0.225 + 0.175\sin\left(\frac{\lambda - 680}{2}\right) \tag{6.26}$$

for wavelengths λ between 500 and 860 nm. For $\lambda < 500$ nm, the g parameters are set constant, such that $g_1 = 0.8$ and $g_2 = -0.4$, whereas for $\lambda > 860$ nm, $g_1 = 0.65$ and $g_2 = -0.05$.

The layer's particle extinction cross section per wavelength was also kept constant. This value is determined from the radius of the particles modeled with the exponential distribution, such that:

$$n(r) \propto r^6 \cdot e^{\frac{-b\cdot r}{r_p}} \tag{6.27}$$

where $n(r)$ is the particles number density with radius r, r_p the radius at which the distribution has its peak, b the exponent value. We input $r_p = 0.1$ μm and $r_p = 1.0$ μm for the upper and lower haze, respectively, and set $b = 6$, according to Hansen and Pollack (1970). These values remained fixed throughout the RT modeling.

At a given wavelength, once $n(r)$ is evaluated for a range of radii r (0.001-100 μm), the code computes the Mie extinction efficiency (Q_{ext}) from the size parameter of the (spherical) particle and its complex refractive index. The former is defined as $x = 2\pi r/\lambda$, with r the radius of the particle and λ the considered wavelength. The latter, with respect to "normal" refractive indices, takes into account both absorption and scattering causing the decrease of light's velocity as it is traveling through a medium. Its formulation was adopted from Karkoschka and Tomasko (2009) as $\underline{n} = n + i\,m_i$: the real part is fixed to a constant value ($n = 1.4$), whereas the imaginary part m_i is modeled with a spectral dependence:

$$m_i = 0.055\,e^{\frac{350-\lambda}{100}} \tag{6.28}$$

with λ the wavelength expressed in nm.

The desired extinction cross section σ for a particle with radius r_i is given by the product of its extinction efficiency Q_{ext} and the geometrical cross section of the particle, i.e. πr_i^2. The extinction cross section of the radii distribution is the weighted sum of all σ per each radius r_i, with weights equal to the corresponding $n(r_i)$ (see Equation 6.27). The procedure is repeated for the analyzed wavelengths.

The impact of a specific aerosol layer on atmospheric opacity is assessed from the layer positional properties. These are the maximum (P_{max}) and minimum (P_{min}) pressure levels, i.e. the lower and upper pressure

boundaries, respectively, of the considered haze, and its fractional scale height (h_{frac}). From these quantities, it is possible to compute the number density N in every discrete layer in which the atmosphere has been divided (Section 6.2) that are contained in the aerosol layer. N is needed to compute the contribution of the aerosol layers to the optical depth of the atmosphere. For each of these discrete layers of thickness z, the number density at its top is given by (Luszcz-Cook et al., 2016):

$$N = N_0 e^{\frac{z}{H \cdot h_{\text{frac}}}} \tag{6.29}$$

with N_0 number density at the bottom of the layer in cm^{-3}, H pressure scale height in cm. H is computed for the discrete layer placed at altitude y as (de Pater and Lissauer, 2011):

$$H(y) = \frac{kT(y)}{g(y)\mu_a(y)m_{\text{amu}}} \tag{6.30}$$

where $k = 1.381 \cdot 10^{-16}$ cm^2 g s^{-2} K^{-1} is the Boltzmann constant, $T(z)$ is temperature in K, $g = 11.15$ cm s^{-2} the gravitational acceleration of Neptune (assumed constant), μ_a is the mean molecular mass in amu, $m_{\text{amu}} = 1.66054 \cdot 10^{-24}$ g is the mass of 1 amu in grams. k, g and m_{amu} are constant values, taken from Luszcz-Cook et al. (2016). μ_a is deduced from the atmosphere setup, computed as the sum of products between molar fraction and molecular mass of each species present in the atmospheric model. T is retrieved from the temperature-pressure profile, interpolated and evaluated at the input pressure boundaries of the discrete layer. The pressure scale height computed in Equation 6.30 is then used to compute N with Equation 6.29.

In the end, the contribution of the hazes on the total optical depth is computed. As seen in Section 6.1, the absorption coefficient results from $N\sigma$, with σ the extinction cross section previously explained. For each discrete layer contained in the considered haze, the optical depth is computed as $N\sigma z$, summed up with all other layers' values to obtain the total optical depth of the haze. Similarly, from the optical depth, the code computes the single scattering albedo of the haze. By definition, ω is the ratio between scattered and absorbed light, i.e. the ratio between the scattering coefficient and the total absorption coefficient (see Equation 6.7). For the entire haze layer, the single scattering albedo is given by the ratio of the total scattering optical depth (i.e. optical depth due to scattering) and the total optical depth.

Two facts are underlined. Firstly, the whole procedure has to be implemented for every considered wavelength. Secondly, the computed single scattering albedo is the total single scattering albedo of the haze layer itself, which is the combination of the single scattering albedos of aerosol particles and gas particles. The aforementioned physical parameter ω, input by the user, was referred to the single scattering albedo of molecules present in the haze layer.

From Equation 6.29, it can be seen that h_{frac} drives the number density of a certain discrete layer. In fact, with fixed N_0, z and H, the smaller the fractional scale height, the larger the number density ratio N/N_0, meaning that the layer has a larger variation of number density between its bottom and its top. As it will be specified in Section 7.1, we adopted a fixed P_{min} for our aerosol layers, in order to reduce free parameters, and we considered the upper boundary of an aerosol layer as the pressure level where the optical depth τ is reduced by a factor of $1/e$ with respect to the optical depth at the base of the aerosol layer. Hence, the fractional scale height drives the vertical extension of the layer itself: the larger it is, the more vertically extended the haze is, since the number density varies more slowly throughout the discrete layers, and the optical depth with it. Therefore, the upper boundary will be placed at a shallower pressure level, with respect to an aerosol layer with a smaller h_{frac}.

Summing up the modeling of the aerosols, the modifiable driving parameters are the single scattering albedo, phase function parameters, exponent of the distribution and peak radius (to compute the cross section) of the haze's scatterers, plus the pressure levels and fractional scale height of the aerosol itself. ω (scatterers single scattering albedo) and P_{max} were considered as free parameters to find the best fit, whereas all other quantities were taken from literature (Chapter 7) and maintained as they are throughout the modeling.

6.5. Rayleigh polarization

A further complication for radiative transfer modeling of Neptune's atmosphere is the dominant effect of Rayleigh scattering, causing the polarization of reflected sunlight, i.e. the change of direction of oscillation plane of electromagnetic waves. Sromovsky (2005) estimates that neglecting this effect returns a consequent error of up to 9% in reflected intensity estimation in cloud-free regions.

To correct for this effect, Rayleigh polarization was taken into account and modeled according to Sromovsky (2005). In his Appendix, the author provided the empirical expression to quantify the extra I/F to be added to the reflectivity computed by DISORT. In a fixed observing geometry, i.e. with cosine of emission angle μ and cosine of incidence angle μ_0 defined, for an atmosphere with N layers, the I/F to be added (ΔI_{tot}) is

$$\Delta I_{\text{tot}} = \sum_{i=1}^{N} e^{-\tau_{E,i}\left(\frac{1}{\mu}+\frac{1}{\mu_0}\right)} \cdot (\Delta I_i - \Delta I_{i-1}) \tag{6.31}$$

with τ_E the cumulative effective aerosol extinction optical depth, defined as

$$\tau_{E,i} = \sum_{i=0}^{i} \Delta\tau_{C,i}(1-g_i) \tag{6.32}$$

where $\tau_{C,i}$ is the optical depth of the i$^{\text{th}}$ aerosol layer and g_i the aerosol's particles local asymmetry parameter. g_i is deduced from the double Henyey-Greenstein phase function moments, i.e. the Legendre polynomial expansion terms of the phase function. The code considers only the first four moments (Luszcz-Cook et al., 2016). For a generic atmospheric layer, the contribution ΔI is expressed as

$$\Delta I = \begin{cases} I_{\max} - (I_{\max} - I_0)\left(1 - e^{-\left(\frac{\theta-\theta_{\max}}{\theta_{\text{width}}}\right)^2}\right)\left(1 - e^{-\left(\frac{\theta_{\max}}{\theta_{\text{width}}}\right)^2}\right)^{-1} & \text{for } 0 \le \theta < \theta_{\max} \\ I_{\max}\left(1-\omega^4\right)\left(\cos\left(\frac{\pi}{2}\left|\frac{\theta-\theta_{\max}}{\frac{\pi}{2}-\theta_{\max}}\right|^{1.15}\right)\right)^{0.6} + \omega^4 \cos\left(\frac{\pi}{2}\left|\frac{\theta-\theta_{\max}}{\frac{\pi}{2}-\theta_{\max}}\right|^{1.4}\right) & \text{for } \theta \ge \theta_{\max} \end{cases} \tag{6.33}$$

where the dependency is on the phase angle θ (angle between incoming rays and the surface's normal directions), the single scattering albedo ω and optical depth τ of the considered layer. All angular variables in the above equation have the following values:

$$\begin{aligned} \theta_{\max} &= \theta_\infty + \left(\frac{\pi}{2} - \theta_\infty\right) e^{\frac{-\tau}{0.935}} \\ \theta_{\text{width}} &= \theta_0 \left(1 - \frac{\theta_{\max}}{\frac{\pi}{2}}\right)^{0.75} \left(\frac{\omega^4 \theta_{\max}}{\theta_\infty}\right)^{1.3} \\ \theta_\infty &= \omega^4 \cdot 44° \\ \theta_0 &= 36.8° \end{aligned} \tag{6.34}$$

with $\theta_{\max}$ the phase angle at which ΔI is maximum and θ_{width} a measure of the steepness of ΔI from its maximum towards smaller angles. $I_{\max}$ and I_0 depend on ω and τ as follows:

$$\begin{aligned} I_0 &= 0.0403\left(1 - e^{-\frac{|\log(1-\omega)|^{1.789}}{0.458}}\right)\left(1 - e^{-\frac{\tau^{1.01}}{0.493}}\right)^{\frac{2}{1.01}} \\ I_{\max} &= 0.0457\left(1 - e^{-\frac{\tau^{1.617}}{1.015}}\right)^{0.6} f(\omega) \end{aligned} \tag{6.35}$$

where $\log(x) = \log_{10}(x)$ and

$$f(\omega) = \begin{cases} \omega^3 & \text{for } \omega > 0.95 \\ 0.882\left(1 - e^{-\frac{|\log(1-\omega)|^{1.789}}{0.458}}\right) & \text{for } \omega \le 0.95 \end{cases} \tag{6.36}$$

The above formulation is adopted from Sromovsky (2005) and is valid for $\theta = 0$, which is a good approximation for our study, as the phase angle θ of Neptune with respect to Earth is such that $\cos\theta \approx 1$.

The described Rayleigh polarization approximation returns the additional I/F to the reflectivity computed with DISORT. All parameters were adopted in their original values and expressions from Sromovsky (2005) and fixed throughout the RT modeling. The scalar approximation at near-zero phase angle is estimated to have a 1% error with respect to the full vector calculations.

To quantify the magnitude of the correction in our study, we used a base model, whose parameters are summarized in Table 6.4, that will be also used for the sensitivity analysis later on (see Section 6.8). We computed two spectra from the same input parameters, but taking into account Rayleigh polarization for one, using the aforementioned approximation, and neglecting it for the other: these are plotted in Figure 6.2 in the blue and red lines, respectively. On the bottom of the spectra, residuals between the two curves are displayed as percentage with respect to the Rayleigh-corrected spectrum. Disregarding the polarization effect leads to a computed reflectivity which is 6% lower than the Rayleigh-corrected I/F at short wavelengths, with this difference progressively decreasing with increasing wavelength, in agreement with Sromovsky (2005).

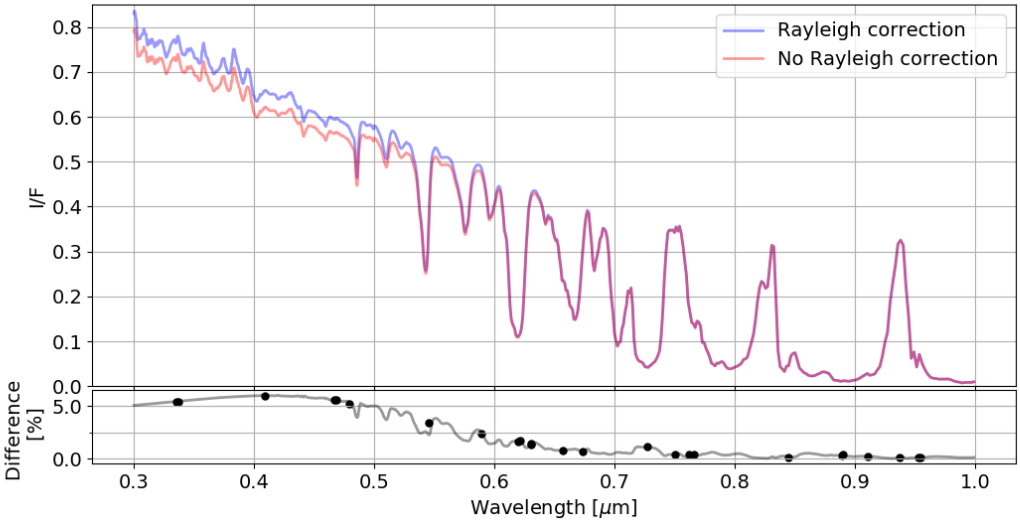

Figure 6.2: **Rayleigh-corrected (blue) and non-Rayleigh corrected (red) spectra.** The image displays the effect of neglecting Rayleigh polarization (red line) with respect to the base Rayleigh-corrected model (blue line). The bottom part shows the difference between the two models (grey line), expressed in percentage with respect to the base model. Black points represent the difference between filters' convolved points of the two models (refer to Appendix B for filters convolution). The correction increases the computed reflectivity up to 6% at shorter wavelengths. The difference decreases as wavelength increases.

6.6. Raman scattering

When the Rayleigh polarization correction is computed, the radiative transfer model of the planet is built from the optical depth and single scattering albedo of the complete atmosphere model, emission and incidence angle, observer azimuth angle and solar azimuth angle. These two last angles are roughly 0° (de Pater and Lissauer, 2011). The Minnaert-corrected data allows to set emission and incidence angle such that their cosine is 1: $\mu = 1$ and $\mu_0 = 1$.

The last correction to be done to the output spectrum from DISORT is related to Raman scattering. Sunlight photons can lose energy due to inelastic scattering with atmospheric particles. As a result, they are reflected at longer wavelengths, causing a loss of reflected light in the UV region (Karkoschka, 1994). To correct for this phenomenon, SUNBEAR adopts the semi-empirical approximation in Karkoschka and Tomasko (2009). The amount of Raman scattering is computed considering the three major hydrogen transitions, i.e. rotational S(0), S(1) and vibrational $Q_1(1)$, responsible for 0.354, 0.587 and 4.161 cm^{-1} shifts, respectively, in photon frequency when arriving with $\lambda = 0.4$ μm. Table VI in Karkoschka (1994) reports that, for Neptune, 17% of photons having wavelength of 0.4 μm is subject to Raman scattering, causing a variation in their wavelength either equal to one of the three aforementioned shifts or to other frequencies.

The impact of Raman scattering is assumed to change with a power c of wavelength. Karkoschka and Tomasko (2009) assessed the exponents to be -0.5 for $\lambda < 0.5$ μm, -2 for 0.5 μm $\leq \lambda < 0.55$ μm, -3 for 0.55 μm $\leq \lambda < 0.6$ μm and -4 for $\lambda \geq 0.6$ μm. These values were adopted and fixed in computing Raman-

corrected reflectivities, whose analytical expression is given by (Sromovsky, 2005):

$$p = f_0(\nu)\,q(\nu) + \sum_{\Delta\nu} f_{\Delta_\nu}(\nu+\Delta\nu)\,q(\nu+\Delta\nu)\,\frac{F_\odot(\nu+\Delta\nu)}{F_\odot(\nu)} \tag{6.37}$$

with $f_0(\nu)$ the fraction of non-Raman scattered photons, f_{Δ_ν} the fraction of photons subject to transition $\Delta\nu$ and $F_\odot$ the solar spectrum intensity. In particular, for each of the three considered transition, the corresponding fraction subject to transition is

$$f_{\Delta_\nu}(\nu+\Delta\nu) = \left(\%_{\Delta_\nu}\right)\left(\frac{\lambda}{0.4}\right)^c \tag{6.38}$$

where $\%_{\Delta_\nu}$ represents the value provided in Table VI in Karkoschka (1994) for the considered transition. Finally, $q(\nu+\Delta\nu)$ is the non-Raman-corrected I/F value output by DISORT for frequency $\nu+\Delta\nu$.

The obtained p is the desired reflectivity for wavelength λ. Iterating the procedure for all wavelengths results in the desired I/F values per wavelength.

The magnitude of the correction for Raman scattering is visualized in Figure 6.3, where the same base model used for the Rayleigh polarization correction is plotted (blue). The base model is Raman-corrected. Neglecting Raman scattering generates a different spectrum (red), whose difference with the same model (grey line, bottom of Figure 6.3) increases as wavelengths increases, reaching more than 80% with respect to the base model values towards the infrared part of the spectrum. The correction for $\lambda < 0.5$ μm agrees with Karkoschka and Tomasko (2009) estimated 4% difference. The largest differences are seen for wavelengths where methane absorption features are seen, e.g. $\lambda = 0.620$ μm, $\lambda = 0.727$ μm and $\lambda = 0.889$ μm.

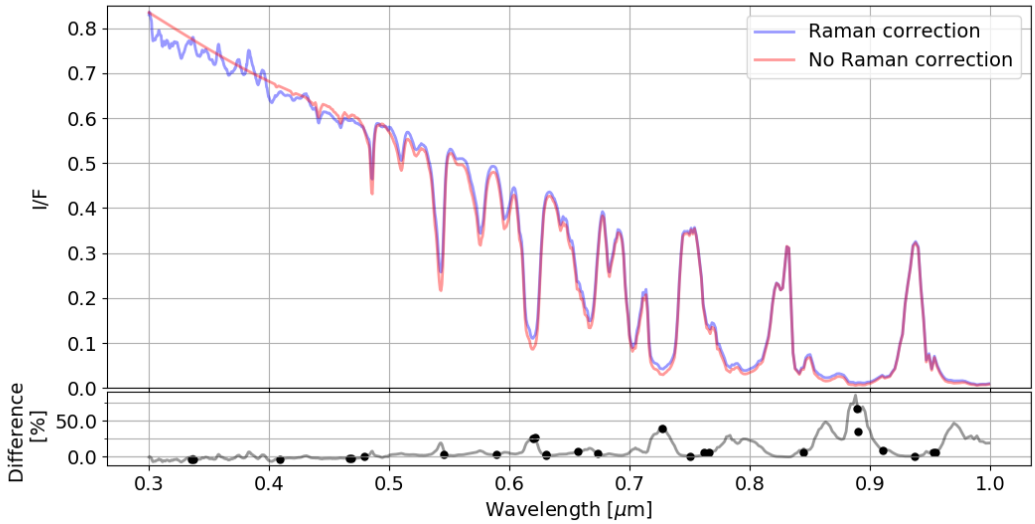

Figure 6.3: **Raman-corrected (blue) and non-Raman corrected (red) spectra.** The image displays the effect of neglecting Raman scattering (red line) with respect to the base Raman-corrected model (blue line). The bottom part shows the difference between the two models (grey line), expressed in percentage with respect to the base model. Black points represent the difference between filters' convolved points of the two models. The correction increases the computed reflectivity up to more than 80% at longer methane absorption features wavelengths.

6.7. Free parameters

To conclude the part dedicated to SUNBEAR assumptions and methods, all parameters are hereby summed up, specifying which of those were taken from literature and kept as they are for the RT modeling, and the ones that were considered free parameters, i.e. that were modified from literature values and were subject to changes in finding the best fitting model for our reflectivity data.

In the atmospheric setup (Section 6.2), the presented quantities were the maximum and minimum pressures of the atmosphere, the pressure boundaries for the higher resolution discrete layers and the resolution itself, the temperature-pressure profile, the chemical composition in terms of species and their abundances,

the (maximum) stratospheric and (deep) tropospheric methane mixing ratios, the methane relative humidity and the saturation vapor pressure curve. Of these, the tropospheric and stratospheric abundance of CH_4 were set as free parameters.

In the gas opacity assessment (Section 6.3), we introduced the k-coefficients for CH_4, H_2, H_2CH_4 and H_2He, the refractive index and depolarization factor for each species. All these values were retrieved from previous literature as they are presented.

In the aerosol modeling (Section 6.4), the treated quantities were the single scattering albedo, phase function parameters, exponent for the exponential distribution of radii and peak radius of scatterers, gravitational acceleration of the planet, fractional scale height and pressure boundaries of aerosols. Of these, we allowed the single scattering albedo of scatterers and pressure boundaries of aerosols as free parameters.

For the Rayleigh polarization (Section 6.5), the driving parameters were θ_∞ and θ_0. For the Raman scattering (Section 6.6), we adopted the solar spectrum and percentage of Raman-scattered photons per major hydrogen transition. All these quantities were taken unchanged from literature.

Tables 6.1-6.2-6.3 collect all parameters used and indicate the reference in literature in which the specific entry was taken. It is also specified which of these were considered as free parameters, whose values will be retrieved with RT modeling in Section 7.

6.8. Sensitivity of parameters

The following Section discusses how changing the free parameters of SUNBEAR, presented in Sections 6.2-6.7 and summarized in Table 6.1, affects the output spectrum. These are the maximum pressure levels of the hazes, the methane mixing ratios, the single scattering albedos of scatterers in the aerosols and the total optical depth at $\lambda = 0.75$ μm of the haze layers. The purpose is to qualitatively describe how free parameters, which are effectively degrees of freedom of the RT code, modify the computed spectrum. Since our measurements are broadband, the difference for convolved points (see Appendix B for details on filter convolution) is also assessed. In the following Sections, the impact of the modification of a single parameter is discussed. A base model is fixed, based on Table 6.1's values of non-free parameters and an arbitrary set of values for the free parameters, displayed in Table 6.4. For each of the parameters, plots of the reference (blue) and altered (red) spectra are shown (Figures 6.4-6.7). Underneath the spectra curves, a plot of the residuals is provided, i.e. the difference between the I/F values of the reference model and the I/F values of the modified model, with points indicating the difference between filters' convolved points of the two models. Where residuals are negative, the modified spectrum returns higher reflectivity values. On the contrary, where residuals are positive, the modified model returns lower reflectivities values. It is noticed that the sensitivity study depends somewhat on the choice of initial parameters. For example, assuming an optically thin upper haze makes the spectrum rather insensitive to changes in the haze parameters. A final caveat on parameter degeneracy closes the current Section.

6.8.1. Pressure levels

In order to assess how the spectrum reacts when the haze layers' pressure levels are modified, four cases are investigated, corresponding to the increase and decrease of the pressure level at which each of the two layers is based. The resulting impact on the spectrum is visible in Figure 6.4.

When the upper haze layer base is moved (left of Figure 6.4), the affected wavelengths are toward the UV region. Up to $\lambda \sim 0.5$ μm, the difference between reference and modified spectra is more significant than for wavelengths longward of 0.5 μm.
The top left plot is obtained with a modified model in which the upper haze is pulled down to larger pressure levels (lower altitudes), namely from $P_{\max,\alpha} = 0.6$ bar to $P_{\max,\alpha} = 1.6$ bar. The expected reflectivity is slightly increased, with the largest change at the shortest wavelength (0.3 μm). The short wavelengths part of the spectrum is more vertical. Beyond $\lambda \sim 0.5$ μm, changes are essentially negligible.
The bottom left plot refers to the modified model, such that the upper haze is lifted to shallower pressure levels, namely $P_{\max,\alpha} = 0.5$ bar. The residual plot displays a mirrored shape with respect to the pulled down haze case. In fact, the strongest change is seen for $\lambda < 0.5$ μm, progressively diminishing with increasing wavelength. In this case, more evident features are seen in the residuals line. Two local maxima are at $\lambda \sim 0.48$ μm, $\lambda \sim 0.54$ μm, $\lambda \sim 0.57$ μm, $\lambda \sim 0.62$ μm, corresponding to the spectrum local minima: these downward peaks are lower with respect to the reference unaltered spectrum. Another remarkable feature is the minimum at $\lambda \sim 0.89$ μm, meaning that the lifted upper haze increases the expected I/F at this wavelength. All these fea-

Parameter	Symbol	Value	Reference
Maximum atmospheric pressure	$P_{\mathrm{max,atm}}$	25 bar	Luszcz-Cook et al. (2016)
Minimum atmospheric pressure	$P_{\mathrm{min,atm}}$	10^{-5} bar	Luszcz-Cook et al. (2016)
Lower high resolution pressure boundary	$P_{\mathrm{max,ref}}$	20 bar	Luszcz-Cook et al. (2016)
Upper high resolution pressure boundary	$P_{\mathrm{min,ref}}$	10^{-2} bar	Luszcz-Cook et al. (2016)
High resolution logarithmic factor	l_{high}	0.075	Luszcz-Cook et al. (2016)
Low resolution logarithmic factor	l_{low}	0.5	Luszcz-Cook et al. (2016)
CH_4 relative humidity at condensation level	$\mathrm{RH_{ac}}$	1.0	Luszcz-Cook et al. (2016)
Phase function parameters	f	0.7	Karkoschka and Tomasko (2011)
	g_1	0.725-0.075 $\sin\left(\frac{\lambda-680}{2}\right)$	Karkoschka and Tomasko (2011)
	g_2	-0.225+0.175 $\sin\left(\frac{\lambda-680}{2}\right)$	Karkoschka and Tomasko (2011)
Exponent for scatterers radii distribution	b	6	Luszcz-Cook et al. (2016)
Peak radius for upper haze	$r_{p,\alpha}$	0.1 μm	Luszcz-Cook et al. (2016)
Peak radius for lower haze	$r_{p,\beta}$	1.0 μm	Luszcz-Cook et al. (2016)
Fractional scale height for upper haze	$h_{\mathrm{frac},\alpha}$	0.17	Molter et al. (2019)
Fractional scale height for lower haze	$h_{\mathrm{frac},\beta}$	0.85	Molter et al. (2019)
Gravitational acceleration	g	11.15 cm $\mathrm{s^{-2}}$	Luszcz-Cook et al. (2016)
θ_0	θ_0	36.8°	Sromovsky (2005)
Exponent of spectral dependence for Raman scattering	c	-0.5 for $\lambda < 0.5$ μm	Karkoschka and Tomasko (2009)
	c	-2 for 0.5 $\mu\mathrm{m} \leq \lambda < 0.55$ μm	Karkoschka and Tomasko (2009)
	c	-3 for 0.55 $\mu\mathrm{m} \leq \lambda < 0.6$ μm	Karkoschka and Tomasko (2009)
	c	-4 for $\lambda \geq 0.6$ μm	Karkoschka and Tomasko (2009)
Upper pressure boundary for upper haze	$P_{\mathrm{min},\alpha}$	10^{-5} bar	Luszcz-Cook et al. (2016)
Upper pressure boundary for lower haze	$P_{\mathrm{min},\beta}$	10^{-5} bar	Luszcz-Cook et al. (2016)
Lower pressure boundary for upper haze	$P_{\mathrm{max},\alpha}$	Free	
Lower pressure boundary for lower haze	$P_{\mathrm{max},\beta}$	Free	
CH_4 tropospheric mixing ratio	$X_{CH_4,t}$	Free	
CH_4 stratospheric mixing ratio	$X_{CH_4,s}$	Free	
Scatterers single scattering albedo for upper haze	ω_α	Free	
Scatterers single scattering albedo for lower haze	ω_β	Free	
Total optical depth of upper haze	τ_α	Free	
Total optical depth of lower haze	τ_β	Free	

Table 6.1: List of SUNBEAR input parameters, with their symbol, value and reference from which the value was taken. Parameters labeled as "free" in their value are the ones modified to obtain the best fitting spectrum for our data.

	H_2	He	N_2	CH_4
Abundance (%)	84.7	15	0.3	Variable
Molecular mass (amu)	2	4	28	16
A (10^{-3})	13.58	3.48	42.70	29.06
B (10^{-3})	7.52	2.30	10.0	7.70
δ	0.02	0.0	0.02	0.03

Table 6.2: Values for the parameters related to the chemical species present in the atmosphere: abundance (volume mixing ratio), molecular mass, empirical parameters for refractive index A and B (see Equation 6.20) and depolarization factor δ. All values are retrieved from Luszcz-Cook et al. (2016) and references within.

Parameter	Symbol	Reference
Temperature-pressure profile	–	Fletcher et al. (2014)
CH_4 k-coefficients	k_{CH_4}	Karkoschka and Tomasko (2010) for $\lambda < 0.518$ μm Sromovsky et al. (2012) for $\lambda \geq 0.518$ μm
H_2 k-coefficients	k_{H_2}	Luszcz-Cook et al. (2016)
H_2He k-coefficients	k_{H_2He}	Luszcz-Cook et al. (2016)
H_2CH_4 k-coefficients	$k_{H_2CH_4}$	Luszcz-Cook et al. (2016)

Table 6.3: Assumed profiles for temperature-pressure and corresponding k-coefficients, with their reference. None of these is a free parameter, as k-tables depend on the temperature-pressure profile.

Model	Upper haze (α)				Lower haze (β)				$X_{CH_{4,s}}$	$X_{CH_{4,t}}$
	$P_{\max,\alpha}$ (bar)	τ_α	ω_α	$h_{\text{frac},\alpha}$	$P_{\max,\beta}$ (bar)	τ_β	ω_β	$h_{\text{frac},\beta}$		
Base	0.6	0.01	0.4	0.85	3.3	5.0	0.95	0.17	0.00035	0.04
Larger $P_{\max,\alpha}$	1.6	0.01	0.4	0.85	3.3	5.0	0.95	0.17	0.00035	0.04
Smaller $P_{\max,\alpha}$	0.5	0.01	0.4	0.85	3.3	5.0	0.95	0.17	0.00035	0.04
Larger $P_{\max,\beta}$	0.6	0.01	0.4	0.85	4.3	5.0	0.95	0.17	0.00035	0.04
Smaller $P_{\max,\beta}$	0.6	0.01	0.4	0.85	2.3	5.0	0.95	0.17	0.00035	0.04
Larger τ_α	0.6	0.1	0.4	0.85	3.3	5.0	0.95	0.17	0.00035	0.04
Smaller τ_α	0.6	0.001	0.4	0.85	3.3	5.0	0.95	0.17	0.00035	0.04
Larger τ_β	0.6	0.01	0.4	0.85	3.3	6.0	0.95	0.17	0.00035	0.04
Smaller τ_β	0.6	0.01	0.4	0.85	3.3	4.0	0.95	0.17	0.00035	0.04
Larger ω_α	0.6	0.01	0.5	0.85	3.3	5.0	0.95	0.17	0.00035	0.04
Smaller ω_α	0.6	0.01	0.3	0.85	3.3	5.0	0.95	0.17	0.00035	0.04
Larger ω_β	0.6	0.01	0.4	0.85	3.3	5.0	0.99	0.17	0.00035	0.04
Smaller ω_β	0.6	0.01	0.4	0.85	3.3	5.0	0.90	0.17	0.00035	0.04
Larger $X_{CH_4,s}$	0.6	0.01	0.4	0.85	3.3	5.0	0.95	0.17	0.0005	0.04
Smaller $X_{CH_4,s}$	0.6	0.01	0.4	0.85	3.3	5.0	0.95	0.17	0.0002	0.04
Larger $X_{CH_4,t}$	0.6	0.01	0.4	0.85	3.3	5.0	0.95	0.17	0.00035	0.06
Smaller $X_{CH_4,t}$	0.6	0.01	0.4	0.85	3.3	5.0	0.95	0.17	0.00035	0.02

Table 6.4: Physical parameters for reference models used for parameter sensitivity assessment: the lower pressure boundaries $P_{\max}$, the layer's optical depth τ, the single scattering albedo ω and the fractional scale height h_{frac}, for upper (α) and lower (β) haze layers. The stratospheric ($X_{CH_{4,s}}$) and tropospheric ($X_{CH_{4,t}}$) methane mixing ratio are reported in the last two columns of the table.

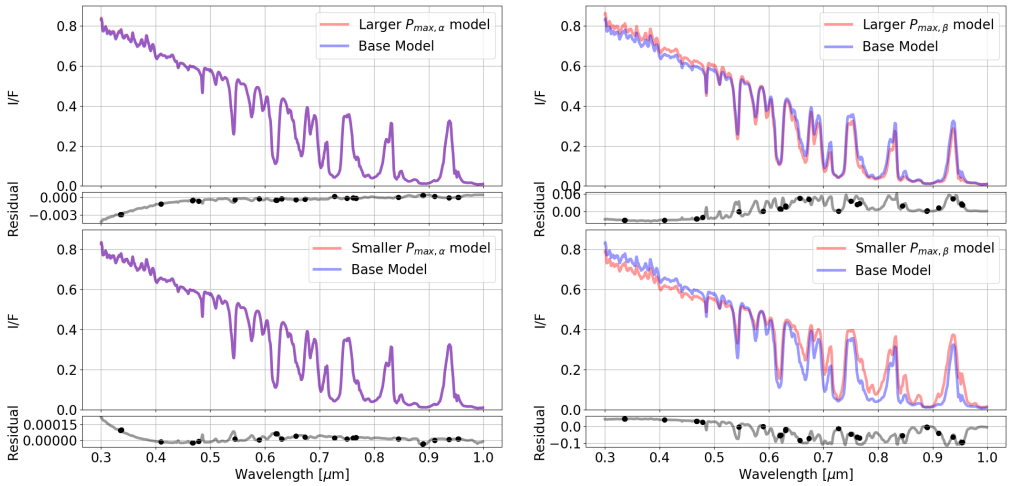

Figure 6.4: **Pressure level sensitivity.** The image displays the effect of changing the lower pressure level of hazes (red line) with respect to the reference model (blue line). The cases shown are for larger (top left) and smaller (bottom left) $P_{\max,\alpha}$, larger (top right) and smaller (bottom right) $P_{\max,\beta}$. On the bottom of each case, residuals in I/F between the compared models are plotted in grey, to visualize at which wavelengths the largest changes occur. Black points identify the difference between the filters' convolved point of the two models.

tures in the residuals plots are also noticed for the pulled down haze case (top left plot) previously discussed, opposite in sign, that were difficult to spot before the comparison with the lifted haze case.

When is the lower haze layer to be moved (right of Figure 6.4), the whole spectrum is subject to changes. It is possible to divide the wavelength region into three parts (Sromovsky et al., 2001a): weak methane absorption band ($\lambda < 0.48$ μm), intermediate methane absorption band ($0.48 \leq \lambda < 0.72$ μm) and strong methane absorption band ($\lambda \geq 0.72$ μm).
If the haze is lifted up from $P_{\max,\beta} = 3.3$ bar to $P_{\max,\beta} = 2.3$ bar (top right plot), thus having a higher altitude for its base, in the weak methane absorption region the model I/F is uniformly shifted upwards, i.e. bumps and peaks preserve their depths and heights. This can be assessed by looking at the residual plot for this region, where the difference between the two models is nearly constant. For the intermediate methane absorption region, the residual plot shows a more bumpy behavior. The peaks in the spectra difference corresponds to local minima in I/F (e.g. at $\lambda \sim 0.57$ μm, $\lambda \sim 0.59$ μm), whereas the residuals change sign for local maxima (e.g. at $\lambda \sim 0.51$ μm, $\lambda \sim 0.52$ μm), meaning that the expected reflectivity is higher at these wavelengths. In general, local maxima are shifted upwards, whilst local minima are pulled downwards. In the strong methane absorption region, local maxima (e.g. at $\lambda \sim 0.75$ μm, $\lambda \sim 0.83$ μm, $\lambda \sim 0.93$ μm) are pulled down, so that the expected reflectivity is overall lower. This is easily visible in the plot of the residuals beneath the two spectra, where in correspondence of the three local maxima in the methane absorption window the largest residuals are found. On the other hand, local minima (e.g. at $\lambda \sim 0.72$ μm, $\lambda \sim 0.80$ μm, $\lambda \sim 0.89$ μm) are kept at their reflectivity value, unaffected by the changed pressure level of the lower haze.
When the lower haze is pulled down to higher pressures ($P_{\max,\beta} = 4.3$ bar, bottom right plot), an opposite trend is seen. The residuals plot shows similar features, but with opposite signs: what was previously increased in the lifted up haze is now decreased in the pulled down haze. In the weak methane absorption band, the spectrum maintains its shape, but it is now moved downwards with respect to the unaltered model. Analogously, in the intermediate methane absorption band, both local minima and maxima are less prominent. Finally, in the strong methane absorption band, the absorption features (local minima) are essentially the same, whereas peaks in reflectivity are higher.
The analyzed changes in the spectrum for the lower haze pressure can be explained as follows. An increase in $P_{\max,\beta}$ implies a larger distance travelled by rays into the atmosphere before encountering the haze and its scatterers. Hence, the specific intensity at long wavelengths reaching the haze is lower, since it passes through a more extended absorbing layer above the haze itself, so that the amount of it scattered back to the observer is also lower, resulting in a lower I/F value. The opposite holds for higher altitudes lower hazes: more light is

back scattered, as more light reaches the haze layer.

Three fact are highlighted. Firstly, the convolved points' residuals follow the same behavior as the one described for the high resolution spectra residuals: most black points on the residuals plot are placed on the grey line. The farthest point is seen for the lower haze pressure changes at $\lambda = 0.775$ μm, corresponding to the broad filter F775W. Secondly, even though the residuals plots have the same (mirrored) shape, values are different, as it can be seen from the residuals' y-axis values. In particular, this is true for the right plots, where the haze is moved by 1 bar both up- and downward with respect to the reference model. Hence, the effect on the expected reflectivity is quantitatively different, showing non-linearity with pressure. This will be the case for all free parameters and it was expected, as the equations of RT presented in the current Chapter are non linear. Therefore, increasing and decreasing a certain parameter of the same quantity does not bring to the same change in reflectivity. Thirdly, it appears that at visible wavelengths the change in pressure base of the lower haze layer has a stronger impact on I/F with respect to the upper haze layer. Hence, fitting pressures of the upper haze does not lead to changes as the lower haze does.

6.8.2. CH_4 mixing ratios

The effect of changing the methane abundance in the stratosphere and the troposphere is hereby assessed. Again, four cases are examined: increase and decrease of $X_{CH_4,s}$, increase and decrease of $X_{CH_4,t}$, with respect to the base model values $X_{CH_4,s} = 0.00035$ and $X_{CH_4,t} = 0.04$. The resulting RT models are displayed in Figure 6.5.

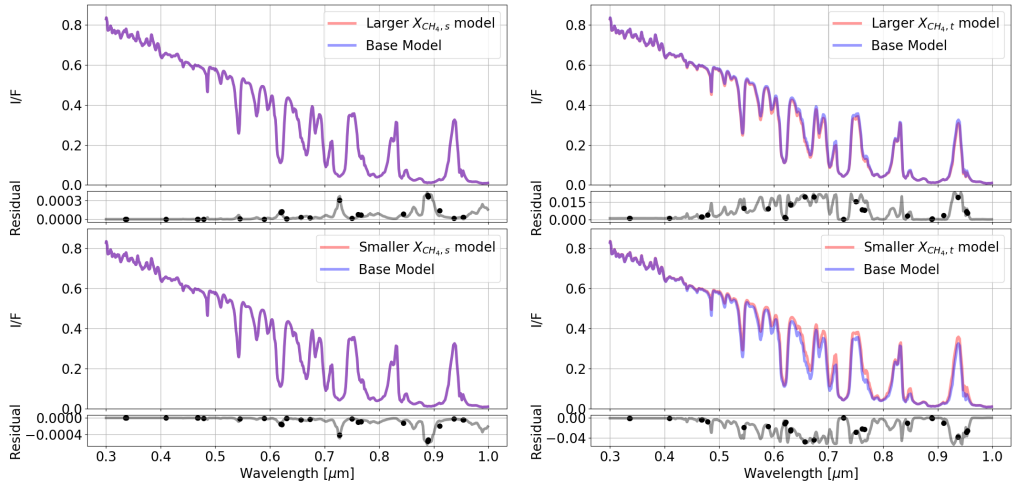

Figure 6.5: **Methane mixing ratio sensitivity.** The image displays the effect of changing the CH_4 mixing ratio of hazes (red line) with respect to the reference model (blue line). The cases shown are for larger (top left) and smaller (bottom left) $X_{CH_4,s}$, larger (top right) and smaller (bottom right) $X_{CH_4,t}$. On the bottom of each case, residuals in I/F between the compared models are plotted in grey, to visualize at which wavelengths the largest changes occur. Black points identify the difference between the filters' convolved point of the two models.

The impact of increased stratospheric methane abundance ($X_{CH_4,s} = 0.0005$, top left) is negligible at short wavelengths, in the weak CH_4 absorption region (see Section 6.8.1): the residuals plot show no difference between the unaltered and modified spectra. In fact, methane abundance is expected to influence methane absorption features of the spectrum. This is the case for the intermediate CH_4 absorption band, where the three spikes in the residuals ($\lambda \sim 0.48$ μm, $\lambda \sim 0.54$ μm, $\lambda \sim 0.62$ μm) correspond to the three absorption features seen at these wavelengths. Hence, in these features, in the modeled scattering conditions, more sunlight is expected to be absorbed, decreasing the expected reflectivity, as a consequence of enriched methane abundance: the more the methane present, the more the absorption phenomenon. On the other hand, local maxima in the spectrum are essentially the same, so that non-methane-absorption regions remain the same. The same holds for the strong CH_4 absorption region: the largest discrepancies with the unaltered model are at $\lambda \sim 0.72$ μm, $\lambda \sim 0.86$ μm and $\lambda \sim 0.89$ μm, i.e. the three most prominent absorption features. No change is expected for the I/F corresponding to the spikes of the spectrum ($\lambda \sim 0.75$ μm, $\lambda \sim 0.83$ μm, $\lambda \sim 0.93$ μm).

When stratospheric methane is depleted ($X_{CH_4,s} = 0.0002$, bottom left), all described trends are maintained, but reversed in sign. The negative residuals in correspondence of methane absorption features previously identified along the spectrum indicate that the lower presence of methane decreases the magnitude of absorption of CH_4.

If the tropospheric methane mixing ratio is increased ($X_{CH_4,t} = 0.06$, top right), the effect starts to show up already in the weak CH_4 absorption band ($\lambda \sim 0.45$ μm). In the intermediate CH_4 absorption band short wavelengths ($\lambda < 0.6$ μm), peaks in the residuals plot correspond to the absorption features (e.g. $\lambda \sim 0.48$ μm, $\lambda \sim 0.54$ μm, $\lambda \sim 0.62$ μm), where the I/F is lower, whereas local maxima have the minimum change with respect to the unaltered model. This behavior is reversed longward of $\lambda \sim 0.6$ μm: the residuals line resembles the shape of the spectrum itself. The largest differences are displayed in the local maxima ($\lambda \sim 0.75$ μm, $\lambda \sim 0.83$ μm, $\lambda \sim 0.93$ μm), where a lower reflectivity is expected, whilst the smallest (null) ones correspond to the absorption features ($\lambda \sim 0.72$ μm, $\lambda \sim 0.86$ μm and $\lambda \sim 0.89$ μm), where the expected I/F is the same. The residuals plot is reversed in sign for the depleted tropospheric methane mixing ratio ($X_{CH_4,t} = 0.02$, bottom right): no difference is seen for short wavelengths, local maxima for $0.45 < \lambda < 0.6$ μm and absorption features for $\lambda \geq 0.6$ μm. The expected reflectivity is higher for all other wavelengths.

It is noticed that the change in methane causes differences between the models that have the same sign: a higher CH_4 abundance cannot increase the expected I/F, and a lower methane mixing ratio cannot decrease the modeled reflectivity. Furthermore, as observed for pressure levels, the quantitative effect of the same change in abundance is different: the absolute values of residuals is not the same when increasing or decreasing methane abundance of the same amount.

6.8.3. Scatterers' single scattering albedo

The single scattering albedo of the scattering particles present in each haze layer causes changes in the modeled spectrum as displayed in Figure 6.6.

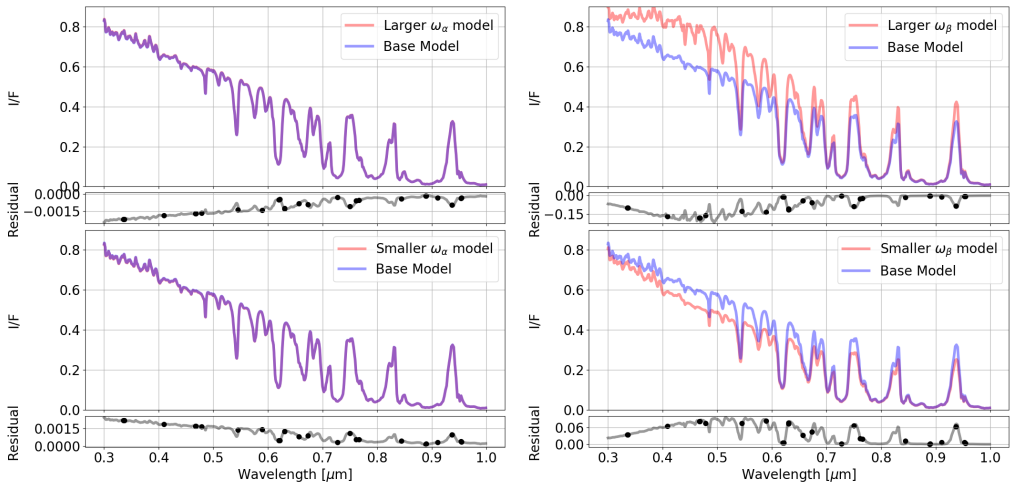

Figure 6.6: **Single scattering albedo sensitivity.** The image displays the effect of changing ω of hazes' scatterers (red line) with respect to the reference model (blue line). The cases shown are for larger (top left) and smaller (bottom left) ω_α, larger (top right) and smaller (bottom right) ω_β. On the bottom of each case, residuals in I/F between the compared models are plotted in grey, to visualize at which wavelengths the largest changes occur. Black points identify the difference between the filters' convolved point of the two models.

The increment of the upper haze particles' single scattering albedo from $\omega_\alpha = 0.4$ to $\omega_\alpha = 0.5$ (top left) produces residuals with the unaltered model that are proportionally larger with decreasing wavelength. Overall, the modified spectrum has a higher expected reflectivity. As for the pressure level case, at short wavelengths (weak methane absorption band), the discrepancies are largest toward the UV region and the modified spectrum has a more negative slope. In the intermediate methane absorption band, local maxima in the residuals correspond to local minima (absorption features) in the spectrum. Since residuals are negative, with respect to non-absorption features, the difference in these minima is lower. This is also true for the strong methane

absorption band, where the downward spikes in the residuals are at wavelengths where the spectra show local maxima in I/F. Hence, in this band, the modified spectrum has an overall higher expected reflectivity, with the largest difference for these wavelengths (e.g. $\lambda \sim 0.75$ μm, $\lambda \sim 0.83$ μm, $\lambda \sim 0.93$ μm).
The opposite holds for the decreased upper haze particles' single scattering albedo ($\omega_\alpha = 0.3$, bottom left). The residuals have opposite sign, so that local maxima are in correspondence of reflectivities' local maxima and local minima at the spectrum's local minima. Again, the residuals grow in value as wavelength decreases. Therefore, the modified model expects an overall lower I/F, with local (within one specific methane absorption band) larger differences for local maxima in the spectrum.

Increasing the lower haze particles' single scattering albedo from $\omega_\beta = 0.95$ to $\omega_\beta = 0.99$ (top right) brings to an overall brighter (i.e. with larger reflectivities) spectrum. For $\lambda < 0.4$ μm, the residuals increase in absolute value with wavelength, meaning that the spectrum has a more horizontal trend with respect to the unaltered model, due to the stronger scattering effect at these short wavelengths. In the remaining weak CH_4 absorption region, the discrepancy is maximum, with a local minimum corresponding to the absorption feature at $\lambda \sim 0.48$ μm (this is true also for minor local minima). Longward of $\lambda \sim 0.5$ μm, residuals progressively diminish, with local minima corresponding to absorption features and local maxima corresponding to local maxima in the spectrum. Therefore, for these wavelengths, absorption features are expected to produce an equal I/F, whereas peaks are higher, producing a larger expected reflectivity.
An opposite behavior is seen when the lower haze particles' single scattering albedo is reduced ($\omega_\beta = 0.9$, bottom right). The largest changes are seen for wavelengths close to 0.5 μm and local maxima in the strong methane absorption region. However, residuals are positive, i.e. the modified spectrum expects lower reflectivities for these wavelengths.

It is highlighted that the largest impact on visible wavelengths reflectivity is given by the modification of the lower haze single scattering albedo. It has to be noticed, though, that the analyzed sensitivity depends also on the choice of the other parameters. With an optically thicker upper haze, changing its single scattering albedo would have resulted in a larger effect on the modified spectrum. Moreover, as for methane, discrepancies with the reference model have the same sign, so that an increase in ω does not produce a lower reflectivity for the considered wavelength region, and, vice versa, its decrease does not increase the I/F in regions with non-strong absorption. Finally, the effect of RT equations non-linearity results in different reflectivity changes when changing the parameter of the same amount, as noted for the upper haze parameter.

The changes seen in the spectrum can be explained as follows. When the upper haze single scattering albedo is increased, particles in this layer scatter more light, both in the forward and backward direction. Hence, more light is redirected backwards, increasing the registered flux density and consequently the computed I/F value. The effect is stronger at short wavelengths as the scattering particles mostly have a radius of 0.1 μm. The opposite holds for the decrease of ω_α: less light is scattered back to the observer. When the lower haze single scattering albedo is changed, conclusions are similar: more light is scattered backwards when ω_β is larger, whereas less light reaches the observer when ω_β is lower.

6.8.4. Total optical depth

The effect of changing the total optical depth of the haze layers on the output spectrum is displayed in Figure 6.7.

The increase of the upper haze optical depth from $\tau_\alpha = 0.01$ to $\tau_\alpha = 0.1$ (top left) produces an overall decrease in reflectivity for visible wavelengths, as more light is absorbed by the haze. The largest differences are seen at short wavelengths ($\lambda < 0.48$ μm), with residuals slightly decreasing with increasing λ. The decreasing trend continues in the intermediate and strong methane absorption bands. The shape of the residuals line resembles the spectrum itself. Absorption features are progressively closer to the reference spectrum while going toward the infrared region. Local maxima in the difference correspond to local maxima in I/F. This occurs since the increase of optical depth increases the fraction of incoming radiation absorbed by the upper haze.
The opposite holds for the decreased upper haze optical depth ($\tau_\alpha = 0.001$, bottom left), where, in general, the expected I/F is larger with respect to the reference spectrum, since a smaller fraction of light is absorbed. The difference decreases as wavelength increases, with local maxima where the spectrum has peaks in reflectivity, and local minima where the spectrum shows absorption features.

When the lower haze optical depth is increased from $\tau_\beta = 5.0$ to $\tau_\beta = 6.0$ (top right), the discrepancies with the reference model have a more complex trend. In the weak methane absorption region, residuals grow slowly with wavelength. The local minima correspond to the absorption features present in this region, i.e.

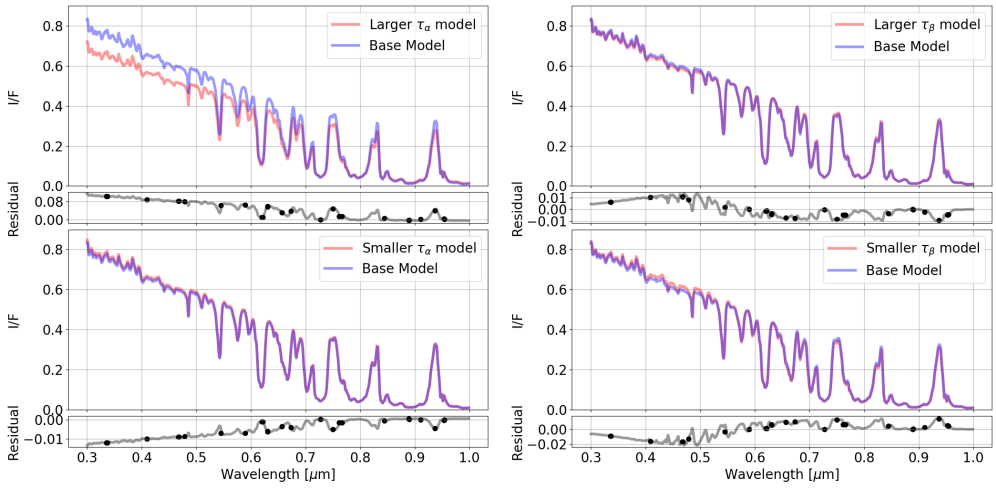

Figure 6.7: **Total optical depth sensitivity.** The image displays the effect of changing τ of hazes (red line) with respect to the reference model (blue line). The cases shown are for larger (top left) and smaller (bottom left) τ_α, larger (top right) and smaller (bottom right) τ_β. On the bottom of each case, residuals in I/F between the compared models are plotted in grey, to visualize at which wavelengths the largest changes occur. Black points identify the difference between the filters' convolved point of the two models.

the modified model expects lower I/F for these features. After having reached a maximum at $\lambda \sim 0.5$ μm, following the direction of growing wavelength, the difference starts to progressively decrease and changes sign before the strong methane absorption band. Local minima in the intermediate methane absorption band shortward of $\lambda \sim 0.6$ μm correspond to absorption features, where a higher reflectivity is expected. The absorption feature at $\lambda \sim 0.62$ μm is essentially the same for the two models. In the strong methane absorption region, an overall higher I/F is expected, with the largest differences corresponding to the spectrum's peaks, whereas no difference is displayed for the methane absorption features in this region. Hence, in general, the expected reflectivity is lower for short and higher for long wavelengths, with respect to the reference model. An inverse-sign behavior is found when the lower haze optical depth is lowered ($\tau_\beta = 4.0$, bottom right). The largest differences are seen for non-absorption features at $0.4 < \lambda < 0.5$ μm and in the strong methane absorption band. The former have a negative discrepancy, i.e. a higher reflectivity is expected; the latter have positive residuals, i.e. a lower I/F is expected, with respect to the reference spectrum.

As for the pressure levels, and unlike the methane abundances and single scattering albedos, residuals are either positive or negative, so that a change in τ causes both a decrease and increase in reflectivities. Similarly to the other parameters, the differences in residuals are not the same if τ is changed by the same quantity, due to RT equations non-linearity.

6.8.5. Degeneracy of parameters

To conclude the Section on parameter sensitivity, considerations are made about parameter degeneracy. With this expression, we refer to the fact that changes in the spectrum can be obtained either with changes in a certain parameter or modifications on a different parameter, to whom the spectrum is sensitive.

In Sections 6.8.1-6.8.4, the effects of changes in free parameters on spectra were analyzed. It is noticed that, for some of them, these effects are similar in specific portions of the considered wavelength region. For example, optical depth and single scattering albedo can have the same (qualitative) impact on wavelengths $\lambda < 0.5$ μm: an increase in ω_α and a decrease in τ_α both produce a higher expected reflectivity, with the magnitude of the increase that is lower with increasing wavelength. Hence, in finding the best fit model, this could be potentially reached with two equal input parameter sets, except for differences in the upper haze single scattering albedo and optical depth.

The parameter degeneracy problem affects radiative transfer performed with broadband observations. A conservative approach is to stick to previous higher spectroscopic resolution literature on the matter. For example, if one of the two input sets obtained has values for ω_α and τ_α similar to such antecedent studies,

these ought to be favored with respect to the other set of parameter that hints at values far from previous analyses.

In this work, this conservative approach is adopted for the RT modeling and models are built on previous works. This affects also the choice of free parameters. Based on Karkoschka (2011), Karkoschka and Tomasko (2011) and Luszcz-Cook et al. (2016), the prioritized parameters are the ones for which sensitivity has been assessed.

7

Radiative transfer modeling results

In order to assess what causes the changing behavior of the background reflectivity over time and latitudinal bands, we performed radiative transfer modeling using the radiative transfer (RT) code SUNBEAR, which is essentially the Luszcz-Cook et al. (2016) code after being extended to the visible wavelength regime (Molter et al., 2019). The purpose is to fit data retrieved from HST with the model spectrum. We did not restrict our data to the blue and methane filters, as done in the temporal analysis in previous Chapters, but we made use of all available filters through which the planet was observed. The RT modeling is done in two directions: one focusing on spatial variations, the other on temporal variations. First, we modeled the vertical structure for all latitudinal bands seen at a certain time, to see whether significant changes affect the physical parameters of hazes at different latitudes. Second, we modeled the vertical structure for selected years seen in the same latitudinal band, to identify how hazes change over time.

In both studies, we started from a "base model", constructed from findings of previous analyses in the visible wavelength region, which best fits a specific latitude or year, and assessed whether this also fits well all other latitudinal bands or years. To assess the goodness of fit, we used the reduced χ^2 test, defined in Tollefson et al. (2019) as:

$$\chi^2 = \frac{1}{n-m} \sum_{i=1}^{n} \left(\frac{r_i}{\sigma_{\text{obs}}} \right)^2 \tag{7.1}$$

where r_i is the residual between the i$^{\text{th}}$ observed reflectivity and the relative expected (convolved) value from the spectrum, σ_{obs} is the observation's uncertainty, $n-m$ is the number of degrees of freedom, i.e. the difference between the number of observations (n) and fitted parameters (m). We computed the associated p value, i.e. the probability that the reduced χ^2 value arises by chance given the degrees of freedom $n-m$. Setting the random chance probability $p = 0.05$, for each value $n-m$ a corresponding limit value for χ^2 is present, such that models with larger χ^2 values are ruled out due to inconsistency with the measurements (Tollefson et al., 2019). For example, for $n-m = 6$, χ^2 values larger than 12.59 imply that the model has a $p < 0.05$ and it is thus inconsistent with data.

7.1. Spatial variations

We chose to perform the modeling in all latitudinal bands for 2009, in which WFC3 returned measurements in 6 different filters. From this same year, Luszcz-Cook et al. (2016) took Keck OSIRIS measurement in NIR, used to model the vertical structure of aerosols in dark regions in a latitudinal band between 2°N-12°N, almost entirely enclosed in our 5°N-20°N band. Thus we are able to have a direct comparison with their model in the same time and location, but seen at different wavelengths.

We set the base model to be the 5°N-20°N band, as it is a representative average behavior band with respect to cloud impact (see Figure 5.1) and it is a good match with the region analyzed in Luszcz-Cook et al. (2016). We adopted the two-layer model proposed in Luszcz-Cook et al. (2016). We fixed the gas abundances also from Luszcz-Cook et al. (2016), the temperature-pressure profile from Fletcher et al. (2014) and particles size distribution peak radii ($r_\alpha = 0.1$ μm and $r_\beta = 1.0$ μm) as in Molter et al. (2019). We followed Molter et al. (2019) in considering the minimum pressure level of both haze layers to be at the upper boundary of the atmosphere (10^{-5} bar), in order to have less free parameters. Nonetheless, the extent of the hazes is

Model	Upper haze (α)				Lower haze (β)					$X_{CH_{4,s}}$	$X_{CH_{4,t}}$
	$P_{\max,\alpha}$ (bar)	τ_α	ω_α	$h_{\text{frac},\alpha}$	$P_{\max,\beta}$ (bar)	τ_β	$\omega_{0,\beta}$	$\omega_{1,\beta}$	$h_{\text{frac},\beta}$		
Base model	1.4	0.04	0.4	0.85	5.1	2.2	0.985	1.4	0.17	0.0006	0.05
Shallow β	1.4	0.04	0.4	0.85	4.6	2.2	0.985	1.4	0.17	0.0006	0.05
CH_4 depleted	1.4	0.04	0.4	0.85	5.1	2.2	0.985	1.4	0.17	0.0006	0.03
Model 2	1.4	0.04	0.4	0.85	4.6	2.2	0.985	1.4	0.17	0.0006	0.03

Table 7.1: Physical parameters of different models: the lower pressure boundaries $P_{\max}$, the layer's optical depth τ, the single scattering albedo ω and the fractional scale height h_{frac}, for upper (α) and lower (β) haze layers. The stratospheric ($X_{CH_{4,s}}$) and tropospheric ($X_{CH_{4,t}}$) methane mixing ratio are reported in the last two columns of the table.

Model	$n-m$	90°S-75°S	75°S-65°S	65°S-50°S	50°S-30°S	30°S-5°N	5°N-20°N	20°N-50°N
Base model	6	**24.08**	**22.10**	**23.36**	**25.89**	5.42	6.11	5.10
Shallow β	5	**15.67**	**13.83**	**14.86**	**17.70**	5.81	**17.50**	7.10
CH_4 depleted	5	6.40	6.48	6.03	6.08	**13.10**	**30.37**	10.18
Model 2	4	4.28	5.27	3.84	3.50	**33.64**	**72.80**	**32.29**

Table 7.2: Reduced χ^2 values for each latitudinal band per model. The number of degrees of freedom $n-m$ is also reported. Statistically significant values for $p < 0.05$ are in bold and indicate regions where the model does not agree with data.

driven by their fractional scale height (h_{frac}) and we considered their upper boundary to be the pressure level at which the optical depth τ is reduced by a factor of $1/e$ (see Chapter 8). Since we are looking at visible wavelengths, we used double Henyey-Greenstein parameters in their wavelength-dependent analytical form found in Karkoschka and Tomasko (2011) (see Section 6.4). We maintained the same fractional scale heights ($h_{\text{frac},\alpha} = 0.85$ and $h_{\text{frac},\beta} = 0.17$) as in Molter et al. (2019). We used methane k-tables from Karkoschka and Tomasko (2011) for $\lambda < 0.518$ μm and from Sromovsky et al. (2012) for $\lambda \geq 0.518$ μm.

All of the aforementioned parameters were kept constant for all latitudes and years. Instead, we left as free parameters the maximum pressure level ($P_{\max}$), optical depth (τ), single scattering albedo (ω) of each layer, as well as the tropospheric ($X_{CH_{4,t}}$) and stratospheric ($X_{CH_{4,s}}$) methane mixing ratio. Our goal is to retrieve the best fitting parameters for the base model and change as few parameters as possible to find better fits for other latitudinal bands.

Our results are summarized in Table 7.1. With respect to previous studies on the physical parameters of hazes in the visible wavelength region, the upper haze layer is located where Karkoschka and Tomasko (2011) set the upper boundary of their semi-infinite haze, with an optical depth consistent with what Hammel et al. (1989a) found ($\tau < 0.05$) from center-to-limb constraints in the visible. The low single scattering albedo value is favored by the NIR observations in Irwin et al. (2016).

The pressure level and opacity of the lower haze is consistent with Hammel et al. (1989a), who found $\tau = 3.0$ and $P_{\max,\beta} > 3$ bar. Since a constant value of the single scattering albedo for the lower layer could not match the I/F values, we followed Karkoschka and Tomasko (2011)'s approach to determine the wavelength dependence of the single scattering albedo of the lower haze using their Equation 2:

$$\omega_\beta(\lambda,\varphi) = \omega_{0,\beta}(\varphi) - \frac{\omega_{1,\beta}(\varphi)}{2 + e^{\frac{\lambda-290}{30}}} \tag{7.2}$$

with $\omega_0(\varphi)$ the single scattering albedo in the near infrared and $\omega_1(\varphi)$ the spectral slope towards the ultraviolet region, both for latitude φ. We used $\omega_0(\varphi = 13°\text{N}) = 0.985$, slightly different from Karkoschka and Tomasko (2011)'s value (0.992), and $\omega_1(\varphi = 13°\text{N}) = 1.4$, which agrees with their Figure 14.

From the sensitivity study in Section 6.8, we noticed that the upper haze and stratospheric parameters do not affect the modeled spectrum as strongly as the lower haze. Hence, the stratospheric methane mixing ratio was adopted from the visible wavelength study from Karkoschka and Tomasko (2011) ($X_{CH_{4,s}} = 0.0006$). This number, despite being larger than Molter et al. (2019)'s value (0.00035), agrees with the $0.00002 - 0.002$ interval proposed by Baines and Hammel (1994) and with the more recent 0.0009 ± 0.0003 value from Fletcher et al. (2010). The retrieved tropospheric value, $X_{CH_{4,t}} = 0.05$, is the upper bound of Karkoschka and Tomasko (2011)'s value.

Table 7.2 reports the reduced χ^2 values for each latitude band with respect to the retrieved base model. For the four southern regions, the values are large, so that the base model is not consistent with the reflectivity values we found in these bands. Hence, we needed a better model to describe the vertical structure at those latitudes. We first attempted to change just one parameter and we noticed that the upper haze does not strongly affect our results as the lower does. Due to degeneracy of parameters, we followed Karkoschka and Tomasko (2011) in restricting the parameters to be changed, i.e. optical depth, single scattering albedo, methane mixing ratio. We also manipulated the bottom pressure level of the hazes, not done by Karkoschka and Tomasko (2011) as they modeled the vertical structure with a thin stratospheric haze overlaying a semi-infinite optically thicker haze below 1.4 bar. Keeping the same formulation for ω, we saw that better fits are obtained by tuning either $P_{\max,\beta}$ or $X_{CH_{4,t}}$. The two new models, which we named shallow β model and CH_4 depleted model, respectively, result in the reduced χ^2 values collected in Table 7.2. We retrieved an alternative model (Model 2), in which we changed both $P_{\max,\beta}$ to a shallower maximum pressure (from 5.1 bar to 4.6 bar) and $X_{CH_{4,t}}$ to a depleted methane mixing ratio (from 0.05 to 0.03) with respect to the base model. Model 2 returns the best fit for bands south of 30°S, whereas it is not consistent with the three bands north of 30°S, as shown by the reduced χ^2 values.

The $X_{CH_{4,t}}$ spatial variability is consistent with Karkoschka and Tomasko (2011). Despite the difference between their model and ours, they also find a depressed tropospheric methane mixing ratio at high latitudes, constraining this variability between 1.2 and 3.3 bar from their 2003 HST-STIS data. We also see that methane depleted regions are south of 30°S, hence extending the mentioned findings to mid-latitudes.

Even though values for $P_{\max,\beta}$ for all the models agree with Hammel et al. (1989a), we found discrepancies of more than 1 bar with respect to the most recent studies of Molter et al. (2019), who also adopted a two-layer model to fit observations in the visible and NIR. They inferred $P_{\max,\alpha} = 0.6$ bar and $P_{\max,\beta} = 3.3$ bar for their background structure, starting from the same temperature-pressure profile, gas abundances, fractional scale heights and similar optical depths we used. Nonetheless, they used single Henyey-Greenstein parameters and a constant value for the single scattering albedo in both layers. We also noticed that the spectra obtained with the parameters of Table 7.1 do not fit well the short wavelengths and that to achieve a good fit for them we affected the goodness of fit for wavelengths longward of ~ 0.65 μm. This could be due to the single scattering albedo parameterization we adopted from Karkoschka and Tomasko (2011) (see Equation 7.2), that might not return a good description of the real ω_β behavior at long wavelengths. Indeed, Karkoschka and Tomasko (2009) pointed out that the aerosols' single scattering albedo for $\lambda > 0.55$ μm is highly uncertain for the ice giants (i.e. Uranus and Neptune). Furthermore, Equation 7.2's expression is empirically extracted from a different vertical structure, namely made of a stratospheric haze and a tropospheric semi-infinite haze, which allows near unity single scattering albedo longward of 0.6 μm, whereas assuming an optically thick layer at 3-4 bar demands for a significant darkening of aerosols (Karkoschka and Tomasko, 2011). We then empirically fitted ω_β longward of 0.65 μm, looking for the simplest possible solution, i.e. a constant value. The best result was achieved imposing $\omega_\beta = 0.85$. Hence, we adopted the following analytical expression for the lower haze single scattering albedo:

$$\omega_\beta = \begin{cases} 0.985 - \frac{1.4}{2+e^{\frac{\lambda-0.29}{0.03}}}, & \text{if } \lambda < 0.65\ \mu m \\ 0.85, & \text{if } \lambda \geq 0.65\ \mu m \end{cases} \tag{7.3}$$

We maintained Karkoschka and Tomasko (2011)'s expression for $\lambda < 0.65$ μm, whereas we set $\omega_\beta = 0.85$ for $\lambda \geq 0.65$ μm. This value at long wavelengths is not far from what Sromovsky et al. (2001b) observed for their 3.8-bar lower haze, for which the single scattering albedo passes from unity for $\lambda < 0.5$ μm to ~ 0.8 at 0.9 μm. Our parameterization is intended to be a simple fit to our data and has to be further corroborated with future measurements (e.g. spectroscopic observation as in Karkoschka and Tomasko, 2009), that might lead to a better and more complicated spectral dependence of ω_β in the 0.65-1.0 μm range.

We redid the radiative transfer modeling with the new single scattering albedo formulation. We found a different base model, whose parameters are collected in Table 7.3. With respect to the previous base model (Table 7.1), in addition to ω_β, the values changed are the maximum pressure levels of the two haze layers, set to values closer to Molter et al. (2019) findings. In fact, $P_{\max,\alpha}$ was set equal (0.6 bar), while the retrieved $P_{\max,\beta}$ (4.1 bar) is found to be slightly higher (0.1 bar) than the upper boundary in Molter et al. (2019) (3.7 bar), when considering error bars.

Table 7.4 collects the reduced χ^2 values for the various bands and quantitatively assesses whether data agree with the base model. As for the previous base model, we find that the bands north of 30°S are well fitted

Model	Upper haze (α)			Lower haze (β)			$X_{CH_{4,s}}$	$X_{CH_{4,t}}$
	$P_{\max,\alpha}$ (bar)	τ_α	ω_α	$P_{\max,\beta}$ (bar)	τ_β	ω_β		
Base model	0.6	$0.03^{+0.02}_{-0.01}$	$0.4^{+0.1}_{-0.2}$	$4.1^{+0.4}_{-0.2}$	$2.2^{+0.7}_{-0.3}$	$\omega_\beta{}^{+0.005}_{-0.008}$	$0.0006^{+0.0394}_{-0.0006}$	$0.050^{+0.009}_{-0.012}$
Shallow β	0.6	$0.03^{+0.02}_{-0.01}$	$0.4^{+0.1}_{-0.2}$	$3.0^{+0.2}_{-0.1}$	$2.2^{+0.7}_{-0.3}$	$\omega_\beta{}^{+0.005}_{-0.008}$	$0.0006^{+0.0394}_{-0.0006}$	$0.050^{+0.009}_{-0.012}$
CH_4 depleted	0.6	$0.03^{+0.02}_{-0.01}$	$0.4^{+0.1}_{-0.2}$	$4.1^{+0.4}_{-0.2}$	$2.2^{+0.7}_{-0.3}$	$\omega_\beta{}^{+0.005}_{-0.008}$	$0.0006^{+0.0394}_{-0.0006}$	$0.020^{+0.015}_{-0.003}$
Model 3	0.6	$0.03^{+0.02}_{-0.02}$	$0.4^{+0.2}_{-0.2}$	$3.4^{+0.2}_{-0.2}$	$2.2^{+0.8}_{-0.2}$	$\omega_\beta{}^{+0.004}_{-0.006}$	$0.0006^{+0.0114}_{-0.0006}$	$0.030^{+0.005}_{-0.008}$

Table 7.3: Physical parameters of different models: the lower pressure boundaries $P_{\max}$, the layer's optical depth τ and the single scattering albedo ω for upper (α) and lower (β) haze layers. The stratospheric ($X_{CH_{4,s}}$) and tropospheric ($X_{CH_{4,t}}$) methane mixing ratio are reported in the last two columns of the table.

Model	$n-m$	90°S-75°S	75°S-65°S	65°S-50°S	50°S-30°S	30°S-5°N	5°N-20°N	20°N-50°N
Base model	6	**29.11**	**27.47**	**28.82**	**30.64**	6.30	2.07	4.58
Shallow β	5	3.93	4.11	3.94	5.18	**22.79**	**57.39**	**26.69**
CH_4 depleted	5	5.63	8.03	6.62	3.52	**24.00**	**44.20**	**17.77**
Model 3	4	2.56	4.16	3.22	2.06	**25.63**	**60.06**	**24.39**

Table 7.4: Reduced χ^2 values for each latitudinal band per model. The number of degrees of freedom $n-m$ is also reported. Statistically significant values for $p < 0.05$ are in bold and indicate regions where the model does not agree with data.

by the new base model, whereas this is not the case for southern mid- and high latitudes (south of 30°S). Following the same approach as before, we built three other models, namely a shallower β layer, a methane depleted troposphere, and a combination of lower $P_{\max,\beta}$ and $X_{CH_{4,t}}$. The parameters used to build these models are collected in Table 7.3.

The shallow β model, where $P_{\max,\beta} = 3.0$ bar, already gives a good fit for the southern hemisphere mid- and high latitudes bands, as the χ^2 values in Table 7.4 show. The opposite holds for bands north of 30°S. The pressure level value is consistent with Molter et al. (2019), as it falls in the range they define ($3.3^{+0.4}_{-0.3}$ bar). The CH_4 depleted model improves the fit only for band 50°S-30°S, with respect to the shallow β model. The decrease in tropospheric methane abundance is from 0.05 to 0.02. We called Model 3 the methane-depleted shallower lower haze model. Its parameters return the best model for bands 90°S-75°S, 75°S-65°S, 65°S-50°S, and 50°S-30°S. The base model (left) and Model 3 (right) are displayed in Figure 7.1. At the bottom of each spectrum, residuals are plotted, computed as $(r_i/\sigma_{\text{obs}})^2$, i.e. the difference between convolved and data points in terms of error bars' extent, so that it is immediate to assess which filters have the largest impact on the χ^2 and thus have the worst fit. The scale in which these residuals are displayed is normalized with respect to the largest residual $(r_i/\sigma_{\text{obs}})^2$ found among all bands in the considered year. The residuals plot shows that bands south of 30°S are not fitted well by the base model due to the large discrepancies at infrared wavelengths.

Our ω_β parameterization allows for pressure levels values closer to previous literature (Luszcz-Cook et al., 2016; Molter et al., 2019) and an overall better fit for latitudinal data, as it can be seen from the lower values in Table 7.4 with respect to those in Table 7.2. This conclusion is to be expected, as we introduced a further free parameter to empirically fit our data.

We computed uncertainties on the retrieved parameter following de Pater et al. (2014)'s approach. The 1σ error on values is defined as the difference between the retrieved parameter and the ones for which the χ^2 value is increased by 1, i.e. $\Delta\chi^2 = \chi^2 - \min\left(\chi^2\right) = 1$. Figure 7.2 shows the χ^2 values of several lower haze pressure base values for the 2009 5°N-20°N base model. The minimum corresponds to our best fitting value (4.1 bar), where $\min\left(\chi^2\right) = 2.07$. $\Delta\chi^2 = 1$ is verified for $P_{\max,\beta} \cong 3.9$ bar and $P_{\max,\beta} \cong 4.5$ bar. Hence, the uncertainty on pressure is -0.2 bar and $+0.4$ bar. Analogously, all other parameters' errors are computed. The method is extended to the temporal variations in Section 7.2.

In Table 7.3, uncertainties are provided for most of the parameters. The upper haze's pressure base does not have an associated error, since $\Delta\chi^2$ is never larger than 1 when changing $P_{\max,\alpha}$. Indeed, the sensitivity analysis (Section 6.8) pointed out that the spectrum is not sensitive to $P_{\max,\alpha}$, so that we adopted the value from Molter et al. (2019). In fact, every value in the 0-10 bar range would have returned $\Delta\chi^2 < 1$. It is also noticed that the stratospheric methane mixing ratio uncertainty is large, spanning from no methane up to $X_{CH_4,s} = 0.04$ for Model 3.

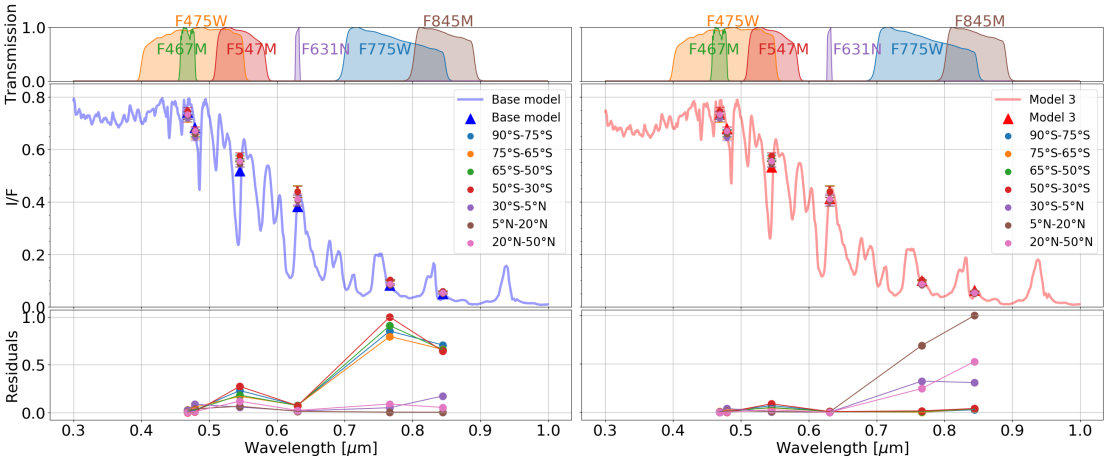

Figure 7.1: **5°N-20°N (left) and 50°S-30°S (right) best fitting models in 2009.** The former is plotted in blue, the latter in red. Circles are the data points extracted from the latitudinal bands, each color corresponds to the band specified in the legend. The triangles represent the model values in filters that imaged Neptune in 2009, obtained by convolution of the model with the filter bandpasses, plotted above the spectrum. Uncertainties include both random and photometric errors (see Section 3.4). Beneath each spectrum, residuals $\left(r_i/\sigma_{\text{obs}}\right)^2$ between convolved and data points are normalized with respect to the largest residual value found in all bands in 2009 and they are displayed for each band, following the same color map of the data points legend.

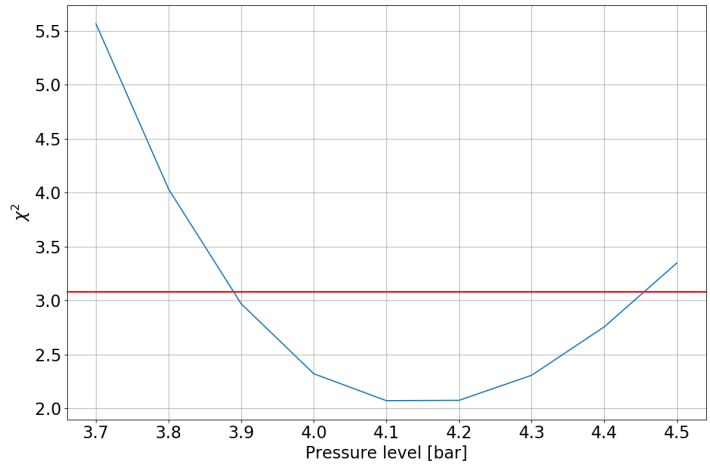

Figure 7.2: χ^2 **values for different** $\mathbf{P_{max,\beta}}$ **values for 2009 5°N-20°N base model.** The minimum value for χ^2, $min\left(\chi^2\right)$, is obtained for the best fitting retrieved parameter of pressure base (4.1 bar). The uncertainties on the retrieved pressure are computed from pressure values where $\Delta\chi^2 = \chi^2 - min\left(\chi^2\right) = 1$ is verified, i.e. $P_{max,\beta} \cong 3.9$ bar and $P_{max,\beta} \cong 4.5$ bar. The red line indicates where $\Delta\chi^2 = 1$.

For the following temporal variations analysis, we adopted the parameters in Table 7.3, specifically the base model for bands 30°S-5°N, 5°N-20°N and 20°N-50°N, while for bands 90°S-75°S, 75°S-65°S, 65°S-50°S and 50°S-30°S we referred to Model 3.

7.2. Temporal variations

Having assessed the latitudinal variability for 2009, we proceeded with the investigation of temporal trends in each of these latitudes, to find the parameters that drive the changes we saw in reflectivity over time. We used 2009 as our reference year, in which we have already defined the base models per latitudinal band. Starting from these, we aim to characterize the vertical structure for specific other years, restricting the variable parameters to the least possible.

Looking at Figures 5.2-5.5, we identified the years in which to model the haze vertical structure. From

the time interval subdivision in blue and methane filters, we selected the approximate boundaries of these intervals, in which we have a sufficient number of filters providing measurements throughout that year. We chose 1996 (9 filters), 2002 (7), 2015 (12) and 2018 (5). For every year, we found the best fitting model, starting from the base model of the considered latitudinal band. We started with the same band we used as base model for the spatial variability analysis, i.e. 5°N-20°N, and then proceeded with all other bands, starting from the South Pole. For each band, the best fitting spectra are shown along with residuals between convolved model and data points, expressed in terms of normalized $(r_i/\sigma_{\rm obs})^2$, as described for the spatial variation (see Section 7.1).

7.2.1. 5°N-20°N

Figure 7.3 reports the best fitting spectra for our 5°N-20°N band, with the 2009 base model spectrum on the left side. The corresponding χ^2 values are collected in Table 7.5. The hazes parameters retrieved from 2009 provide a good fit for other dates, as the reduced χ^2 values show: given the degrees of freedom $n-m$, the χ^2 values are not significant for $p < 0.05$. Nonetheless, the expected I/F for the F336W filter is larger than the observed one. Trying to find a better match leads to worse fit for longer wavelengths, where both error bars and reflectivity values are small with respect to the rest of the spectrum. Small shifts in reflectivity cause large changes in χ^2: from Equation 7.1, small changes of r_i are increasingly amplified with decreasing $\sigma_{\rm obs}$.

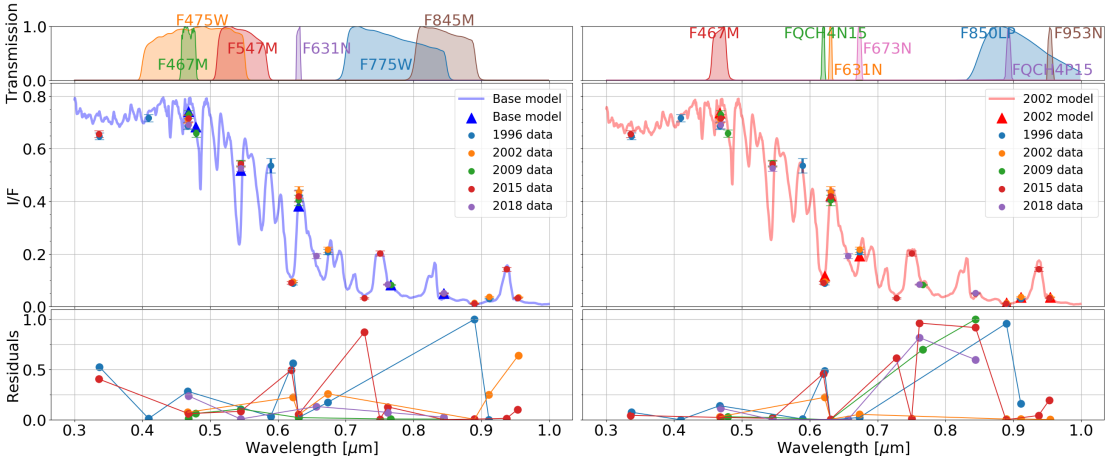

Figure 7.3: **Modeled spectra for band 5°N-20°N.** The 2009 base model is plotted in the blue line (left). The best fitting model for 2002 is plotted in red (right). Circles are the data points extracted from the reference years, each color corresponds to the year specified in the legend. The triangles represent the model values in filters that imaged Neptune in the model's year, obtained by convolution of the model with the filter bandpasses, plotted above the spectrum. Uncertainties include both random and photometric errors (Section 3). Beneath each spectrum, residuals $(r_i/\sigma_{\rm obs})^2$ between convolved and data points are normalized with respect to the largest residual value found in all years with respect to the considered model and they are displayed for each year, following the same color map of the data points legend.

In the attempt to improve the fit, we found a better fitting model for data from 2002 (right of Figure 7.3), output with the same set of parameters of the band's base model (Table 7.3) except for the pressure level at which the lower haze is based, lifted up from $P_{{\rm max},\beta} = 4.1^{+0.4}_{-0.2}$ bar to $P_{{\rm max},\beta} = 3.2^{+0.2}_{-0.2}$ bar. The alternative model better fits F336W data. However, with respect to other years, this model returns a worse fit than the base model. If, on the one hand, the expected reflectivity is closer to the observed one for F336W, on the other hand the alternative model lifts the spectrum in correspondence of the absorption features at $\lambda = 0.619$ μm and $\lambda = 0.727$ μm, whose error bars are small (~ 0.005). The increased r_i for these methane absorption filters produces a larger contribution to the reduced χ^2 value with respect to the decreased residuals found towards the UV part of the spectrum.

For this band, data are consistent with a vertical structure changed in 2002 with respect to other years, in which the structure could have been maintained in its 2009 configuration. The change concerns the lower haze, whose base is lifted up to $P_{{\rm max},\beta} = 3.2^{+0.2}_{-0.2}$ bar. The difference between 1996 and 2002 is consistent with the changing behavior found in the blue filter in these years. The changes seen in the same filter in 2004-2008 might have been too small to imply a modified vertical structure between these two years. The fact that

Band	Model	Years				
		1996	2002	2009	2015	2018
90°S-75°S	Base Model	12.50 (7)	8.30 (5)	2.56 (4)	7.49 (10)	**10.24** (3)
	Model 2018	13.85 (7)	**15.32** (5)	8.57 (4)	8.67 (10)	5.23 (3)
75°S-65°S	Base Model	**14.92** (7)	10.86 (5)	4.16 (4)	7.95 (10)	**9.01** (3)
	Model 1996	13.86 (7)	**15.86** (5)	5.89 (4)	8.38 (10)	**7.85** (3)
	Model 2002	**18.40** (7)	4.73 (5)	**20.27** (4)	20.63 (10)	**44.59** (3)
	Model 2018	**14.99** (7)	**14.80** (5)	5.68 (4)	8.07 (10)	6.78 (3)
65°S-50°S	Base Model	11.58 (7)	**16.82** (5)	3.22 (4)	9.71 (10)	**18.52** (3)
	Model 2002	13.98 (7)	6.26 (5)	**26.93** (4)	**32.22** (10)	**82.07** (3)
	Model 2018	9.90 (7)	**30.58** (5)	**18.67** (4)	10.66 (10)	**8.60** (3)
50°S-30°S	Base Model	7.93 (7)	**30.18** (5)	2.06 (4)	8.75 (10)	**20.75** (3)
	Model 2002	11.08 (7)	**11.58** (5)	**55.72** (4)	**51.34** (10)	**171.32** (3)
	Model 2018	9.13 (7)	**47.76** (5)	**19.87** (4)	12.44 (10)	5.26 (3)
30°S-5°N	Base Model	15.34 (9)	**16.86** (7)	6.31 (6)	11.27 (12)	3.81 (5)
	Model 2002	14.96 (8)	5.18 (6)	**22.79** (5)	**21.97** (11)	**54.67** (4)
5°N-20°N	Base Model	16.48 (9)	12.20 (7)	2.07 (6)	10.56 (12)	5.41 (5)
	Model 2002	**21.58** (8)	5.11 (6)	**32.59** (5)	**27.80** (11)	**35.75** (4)
20°N-50°N	Base Model	8.59 (9)	**31.32** (7)	4.58 (6)	15.62 (12)	**12.86** (5)
	Model 1996	5.04 (8)	**14.41** (6)	**18.33** (5)	10.41 (11)	**53.63** (4)
	Model 2002	8.25 (8)	7.81 (6)	**75.64** (5)	**31.79** (11)	**143.91** (4)
	Model 2018	7.76 (8)	**38.05** (6)	**12.95** (5)	19.00 (11)	7.64 (4)

Table 7.5: Reduced χ^2 values for each latitudinal band per year for several models. The number of degrees of freedom $n-m$ is reported in brackets near the χ^2 value. Statistically significant values for $p < 0.05$ are in bold and indicate regions where the model does not agree with data.

the model is the same for 2015 and 2018 confirms the constant behavior deduced from both the blue and methane filters for this band.

7.2.2. 90°S-75°S

The base model for this latitudinal band is Model 3 in Table 7.3. With respect to other years, the fit does not agree only with 2018 data. This can be assessed from the left plot in Figure 7.4, where Model 3's output spectrum and residuals are reported. The χ^2 value tells that the fit does not agree with the most recent observations in 2018. The residuals for this year are not as large as for 1996 or 2015, but the fact that 2018 has only 5 measurements and that all 5 wavelengths have an appreciable value cause the non-compliance with the spectrum.

We noticed that the driving free parameter is the lower haze pressure layer. Pulling down the lower haze layer base from $P_{\max,\beta} = 3.4^{+0.2}_{-0.2}$ bar to $P_{\max,\beta} = 3.8^{+0.2}_{-0.2}$ bar results in a better fit for 2018: the expected reflectivity gets closer to data in all filters, in particular for wavelengths longward of 0.7 μm. The fitness improvement is restricted to this year, producing larger χ^2 values with respect to the band's base model (see Table 7.5).

With respect to our findings in the latitudinal temporal trend for the reference filters (Section 5), this band showed an average changing behavior (with respect to other bands) in reflectivity for the 1994-2002 period in the blue filter and in the 2015-2018 period in the methane filter. From the RT modeling, we deduced that the increase in reflectivity in the blue filter might not imply a change in the vertical structure, as we found it to be the same between 1996 and 2015. On the contrary, the decreasing reflectivity in the methane filter can be caused by the lower haze layer deeper pressure base found for 2018.

7.2.3. 75°S-65°S

As for band 90°S-75°S, the reference model is Model 3 from Table 7.3. When verifying if the model fitting 2009 is also in agreement with other years, we noticed that this is the case only for 2002 and 2015. All best fitting spectra are shown in Figure 7.5.

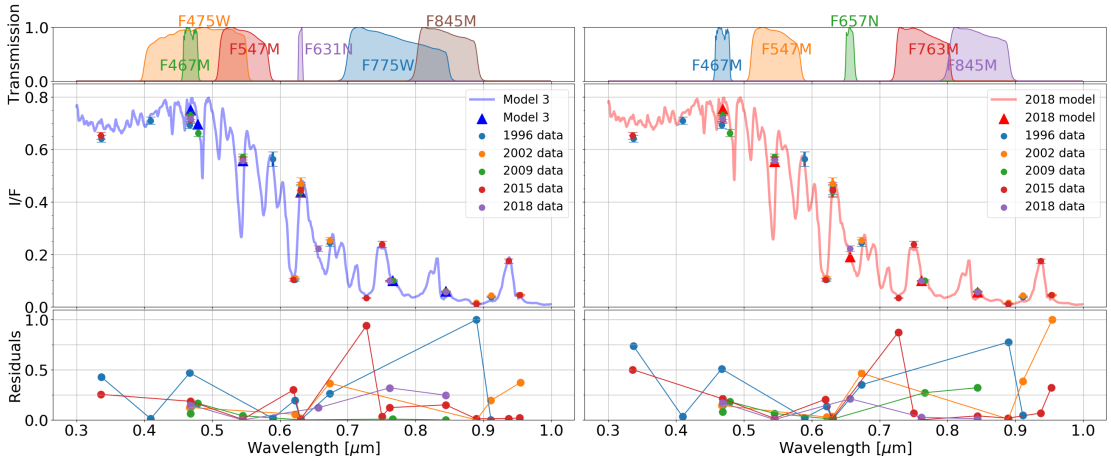

Figure 7.4: **Modeled spectra for band 90°S-75°S.** The 2009 base model is plotted in the blue line (left). The best fitting model for 2018 is plotted in red (right). Circles are the data points extracted from the reference years, each color corresponds to the year specified in the legend. The triangles represent the model values in filters that imaged Neptune in the model's year, obtained by convolution of the model with the filter bandpasses, plotted above the spectrum. Uncertainties include both random and photometric errors (Section 3). Beneath each spectrum, residuals $\left(r_i/\sigma_{\text{obs}}\right)^2$ between convolved and data points are normalized with respect to the largest residual value found in all years with respect to the considered model and they are displayed for each year, following the same color map of the data points legend.

For 1996, the large χ^2 value is mostly caused by the discrepancies for filters at $\lambda = 0.336$ μm and $\lambda = 0.467$ μm, qualitatively evident from the spectrum plot, but also at $\lambda = 0.620$ μm, $\lambda = 0.673$ μm and $\lambda = 0.889$ μm, visually more subtle, with the longest wavelength reflectivity discrepancy being the largest by a factor of 2.5 or more with respect to the others, as seen in the residuals plot. A slightly better model was found when we changed the lower haze maximum pressure level ($P_{\text{max},\beta} = 3.2^{+0.1}_{-0.1}$ bar) and the tropospheric methane mixing ratio ($X_{CH_4,t} = 0.050^{+0.003}_{-0.003}$). However, the χ^2 value is still significant for $p < 0.05$, i.e. the model does not fully capture our data. In addition, the found error bar overlaps with the uncertainty of the base model's pressure, hence not ruling out the possibility that no change occurred between the two years on the vertical position of the lower haze base. A generally worse fit is seen for all other years with respect to 2009, with the exception of 2018, in which the model is still not consistent with observations. The 1996 model is reported in the top right plot of Figure 7.5.

For 2018, the negative impact on the χ^2 value is largely given by the differences in the blue ($\lambda = 0.467$ μm) and F763M ($\lambda = 0.763$ μm) filters. If the lower haze is pulled down to deeper pressures ($P_{\text{max},\beta} = 3.6^{+0.2}_{-0.2}$ bar) with respect to the base model, the output model agrees with data, as assessed by the new set of χ^2 values. Nonetheless, as noticed for 1996, the error bar extent does not guarantee a change in the vertical location of the lower haze. With respect to the 2009, this model returns an overall worse fit for years other than 2018, but it is still consistent with 2009 and 2015. It is pointed out that the goodness of fit test for 2018 loses efficacy due to the low number of degrees of freedom (3). The 2018 model is reported in the bottom right plot of Figure 7.5.

In looking for an appropriate model for 1996, we found a better fit for 2002 (bottom left of Figure 7.5), even if those are also fitted with the 2009 model. Indeed, when setting $P_{\text{max},\beta} = 2.9^{+0.2}_{-0.2}$ bar, the χ^2 value is more than halved with respect to the one referred to the base model. The 2009 base model does not capture reflectivity at $\lambda > 0.9$ μm, as well as for $\lambda = 0.657$ μm. With a shallower lower haze, the expected reflectivities at these wavelengths are closer to the observed ones and thus return a better match. Hence, the vertical structure might have changed also in 2002, as the model found for this year is only consistent with 2015.

From the temporal trend of this band, we saw a changing behavior in I/F in 1994-2008 for the blue filter and in 2015-2018 for the methane filter. The fact that 1996, 2002 and 2009 have different pressure bases of the lower haze that agree with data in these years is in line with our findings for the blue filter. Similarly, the different model for 2018 with respect to the base model agrees with the 2015-2018 methane filter trend. Nonetheless, it is noticed that the 2018 model agrees also with data from 2009 and 2015.

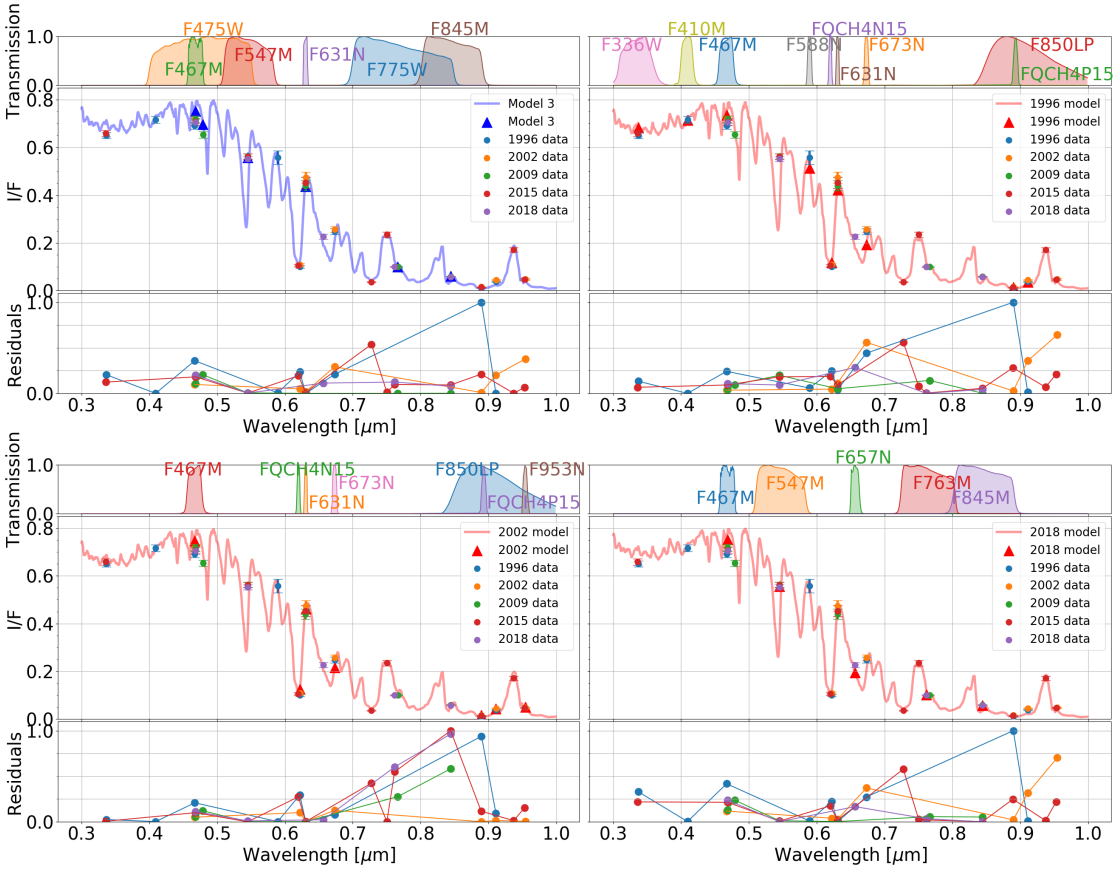

Figure 7.5: **Modeled spectra for band 75°S-65°S.** The 2009 base model is plotted in the blue line (top left). The best fitting models for 1996 (top right), 2002 (bottom left) and 2018 (bottom right) are plotted in red. Circles are the data points extracted from the reference years, each color corresponds to the year specified in the legend. The triangles represent the model values in filters that imaged Neptune in the model's year, obtained by convolution of the model with the filter bandpasses, plotted above the spectrum. Uncertainties include both random and photometric errors (Section 3). Beneath each spectrum, residuals $(r_i/\sigma_{\rm obs})^2$ between convolved and data points are normalized with respect to the largest residual value found in all years with respect to the considered model and they are displayed for each year, following the same color map of the data points legend.

7.2.4. 65°S-50°S

Figure 7.6 displays the best fitting spectra for band 65°S-50°S, with Model 3 in the top left plot. Looking at the χ^2 values, 2002 and 2018 data do not agree with the 2009 model. For 1996, as seen for the other bands, the shortest wavelengths data points, i.e. observations in the F336W and F467M filters, are diverse than the modeled I/F. Moreover, the blue filter is also different with respect to the expected reflectivity: this is the case also for wavelengths seen for band 75°S-65°S, i.e. $\lambda = 0.620$ μm, $\lambda = 0.673$ μm and $\lambda = 0.889$ μm. Nonetheless, the discrepancies are now smaller and make the spectrum a satisfactory fit for 1996.

In 2002, the most affected wavelengths seen for band 75°S-65°S ($\lambda > 0.9$ μm and $\lambda = 0.657$ μm) are also the ones that have the largest difference with respect to the 2009 modeled spectrum for the current band. Lifting up the lower haze base to a shallower pressure level gives an overall better fit, with these wavelengths' differences reduced. The best fit is obtained with $P_{\max,\beta} = 2.8^{+0.2}_{-0.2}$ bar (top right plot of Figure 7.6). With respect to other years, this 2002 model is not consistent with data, except for 1996, though its p-value is very close to 0.05 (namely 0.052).

In 2018, we observe the largest discrepancies with 2009 model for the blue filter and F763M, as noticed for band 75°S-65°S, but an additional significant contribution is also given in the methane filter. We found

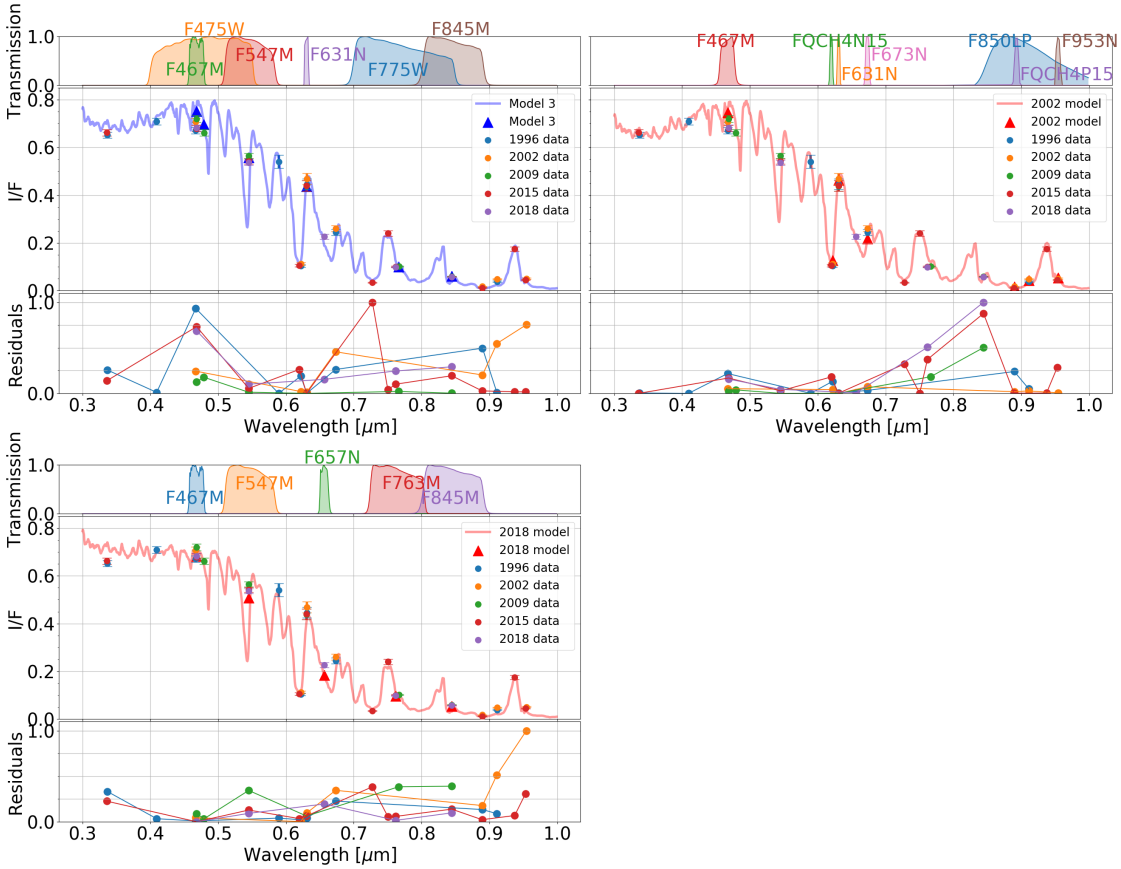

Figure 7.6: **Modeled spectra for band 65°S-50°S.** The 2009 base model is plotted in the blue line (top left). The best fitting models for 2002 (top right) and 2018 (bottom left) are plotted in red. Circles are the data points extracted from the reference years, each color corresponds to the year specified in the legend. The triangles represent the model values in filters that imaged Neptune in the model's year, obtained by convolution of the model with the filter bandpasses, plotted above the spectrum. Uncertainties include both random and photometric errors (Section 3). Beneath each spectrum, residuals $(r_i/\sigma_{\rm obs})^2$ between convolved and data points are normalized with respect to the largest residual value found in all years with respect to the considered model and they are displayed for each year, following the same color map of the data points legend.

a better model (bottom left plot of Figure 7.6) by changing the lower haze base to $P_{\max,\beta} = 4.1^{+0.1}_{-0.1}$ bar and the scatterers single scattering albedo for the lower haze: its formulation is the same (Equation 7.3), but the constant part of ω_β shortward of 0.65 μm is lowered from $0.985^{+0.004}_{-0.006}$ to $0.970^{+0.006}_{-0.007}$. Even if this change lowers the χ^2 value, this is not sufficient to have a model in agreement with data. The obtained spectrum provides a better fit for 1996 with respect to 2009.

This band displayed one of the strongest changes in reflectivity in both the blue and methane filters for 1994-2002, whereas from 2004 it showed a constant behavior. The fact that every model for this band agrees with one between 1996 and 2002 confirms the difference in vertical structure for these years. From the RT analysis, we favored the possibility that in 2018 is also different with respect to the base model in 2009.

7.2.5. 50°S-30°S

The base model from 2009 for this band is depicted in the top left plot in Figure 7.7. With respect to data, the output spectrum captures observations from 1996 and 2015, whereas it does not provide a good fit for 2002 and 2018.

The largest mismatch in reflectivity for 2002 is given for the infrared methane absorption band filters

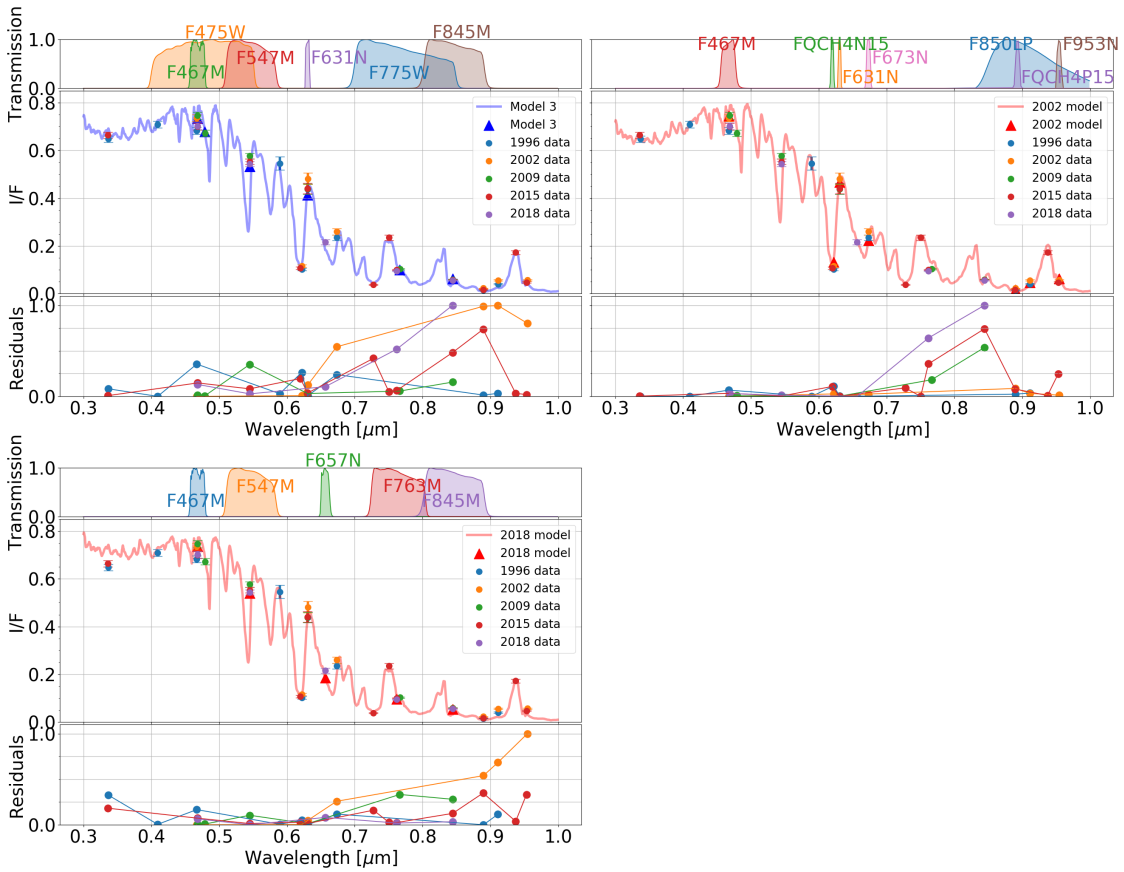

Figure 7.7: **Modeled spectra for band 50°S-30°S.** The 2009 base model is plotted in the blue line (top left). The best fitting models for 2002 (top right) and 2018 (bottom left) are plotted in red. Circles are the data points extracted from the reference years, each color corresponds to the year specified in the legend. The triangles represent the model values in filters that imaged Neptune in the model's year, obtained by convolution of the model with the filter bandpasses, plotted above the spectrum. Uncertainties include both random and photometric errors (Section 3). Beneath each spectrum, residuals $(r_i/\sigma_{\rm obs})^2$ between convolved and data points are normalized with respect to the largest residual value found in all years with respect to the considered model and they are displayed for each year, following the same color map of the data points legend.

(FQCH4P15, F850LP and F953N), whose measured I/F is higher than the modeled one. Shortward of λ = 0.65 μm, the spectrum matches with data. We found a better fitting model (top right of Figure 7.7) by positioning the lower haze layer to $P_{\max,\beta} = 2.6^{+0.2}_{-0.1}$ bar. Nonetheless, the returned χ^2 indicates that the model, though better with respect to 2009, does not match the observed I/F. With respect to measurements from all other years, the spectrum is not appropriate for years later than 2002. In 1996, the fit is worse than the 2009 model, but still in agreement with observations.

For 2018, the largest contribution to the high χ^2 value is due to discrepancies at short (blue filter) and long wavelengths ($\lambda > 0.7$ μm). The central part of the wavelength range returns a good match between model and empirical values. As for band 65°S-50°S, a better fit (bottom left of Figure 7.7) is obtained with the lower aerosol layer based at $P_{\max,\beta} = 4.1^{+0.2}_{-0.4}$ bar and the constant part of the lower haze single scattering albedo formula set to $0.975^{+0.005}_{-0.007}$ for < 0.65 μm. The new spectrum can give reason to measurements from 1996 and 2015, though with a worse fit with respect to the 2009 model, but not for 2002 nor 2009. The error bars extent for ω_β does not ensure the change of this parameter.

This band showed the largest increase in I/F for the blue and methane filters in the 1994-2002 period, and an average decrease in 2015-2018 in the methane filter. The disagreement of models in which 1996 data are

fitted with $p > 0.05$ with 2002 data confirms the changing trend seen in both reference filters. We also might have a different vertical structure in 2018 with respect to 2009, whose data are not fitted from the 2009 model and, vice versa, the 2018 model is not consistent with 2009 data.

7.2.6. 30°S-5°N

For our largest latitudinal band, we returned to the 2009 base model of band 5°N-20°N, reported in the left side of Figure 7.8. As noticed for that band, the model is detached from data points at $\lambda = 0.336$ μm. Nonetheless, the χ^2 values for 1996 and 2015, from which observations at this wavelength are performed, indicates an overall agreement with data in these years. On the contrary, 2002 measurements are not matched by the spectrum.

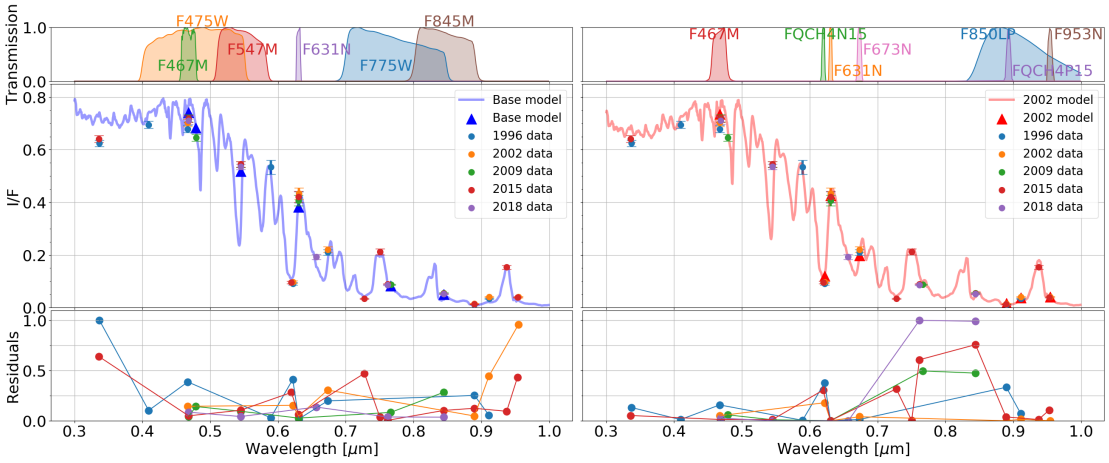

Figure 7.8: **Modeled spectra for band 30°S-5°N.** The 2009 base model is plotted in the blue line (left). The best fitting models for 2002 (right) is plotted in red. Circles are the data points extracted from the reference years, each color corresponds to the year specified in the legend. The triangles represent the model values in filters that imaged Neptune in the model's year, obtained by convolution of the model with the filter bandpasses, plotted above the spectrum. Uncertainties include both random and photometric errors (Section 3). Beneath each spectrum, residuals $\left(r_i/\sigma_{\rm obs}\right)^2$ between convolved and data points are normalized with respect to the largest residual value found in all years with respect to the considered model and they are displayed for each year, following the same color map of the data points legend.

What has been found for band 75°S-65°S in 2002 applies also here. The largest difference with respect to the model are seen in the infrared ($\lambda > 0.9$ μm) and at $\lambda = 0.673$ μm. A better atmospheric model (right of Figure 7.8) is obtained setting a shallower lower haze pressure base at $P_{{\rm max},\beta} = 3.0^{+0.2}_{-0.2}$ bar. This model matches reflectivities in the mentioned wavelengths. It also provides a slightly better fit for 1996, as the spectrum line gets closer to observations at $\lambda < 0.5$ μm. On the opposite, this model does not agree with observations from years after 2002.

From the latitudinal temporal trend analysis, this band showed an increasing reflectivity in 1994-2008, having the smallest linear fit slope for the blue filter. In the methane filter, reflectivities might display a changing behavior in 2015-2018. We found that 2002 has a vertical structure different from successive years, in agreement with the blue filter trend. After 2009, the structure might have been the same, as opposed to what we see in the methane filter, but again in line with the blue filter.

7.2.7. 20°N-50°N

For our northernmost latitudinal band, the 2009 base model, which is the same as for 5°N-20°N, agrees with measurements taken in 1996 and 2015, though not returning a good match with 2002 and 2018, as shown in the top left plot in Figure 7.9.

As for band 30°S-5°N, the 2002 data that produce the major contribution to the χ^2 value are at $\lambda > 0.9$ μm and $\lambda = 0.673$ μm, with the addition of $\lambda = 0.889$ μm. Reflectivities at these wavelengths are closer to the expected I/F of a shallower lower haze layer model: lifting the pressure base of the β layer to $P_{{\rm max},\beta} = 2.7^{+0.2}_{-0.1}$ bar returns a spectrum consistent with data (bottom left of Figure 7.9). The model is also good for 1996,

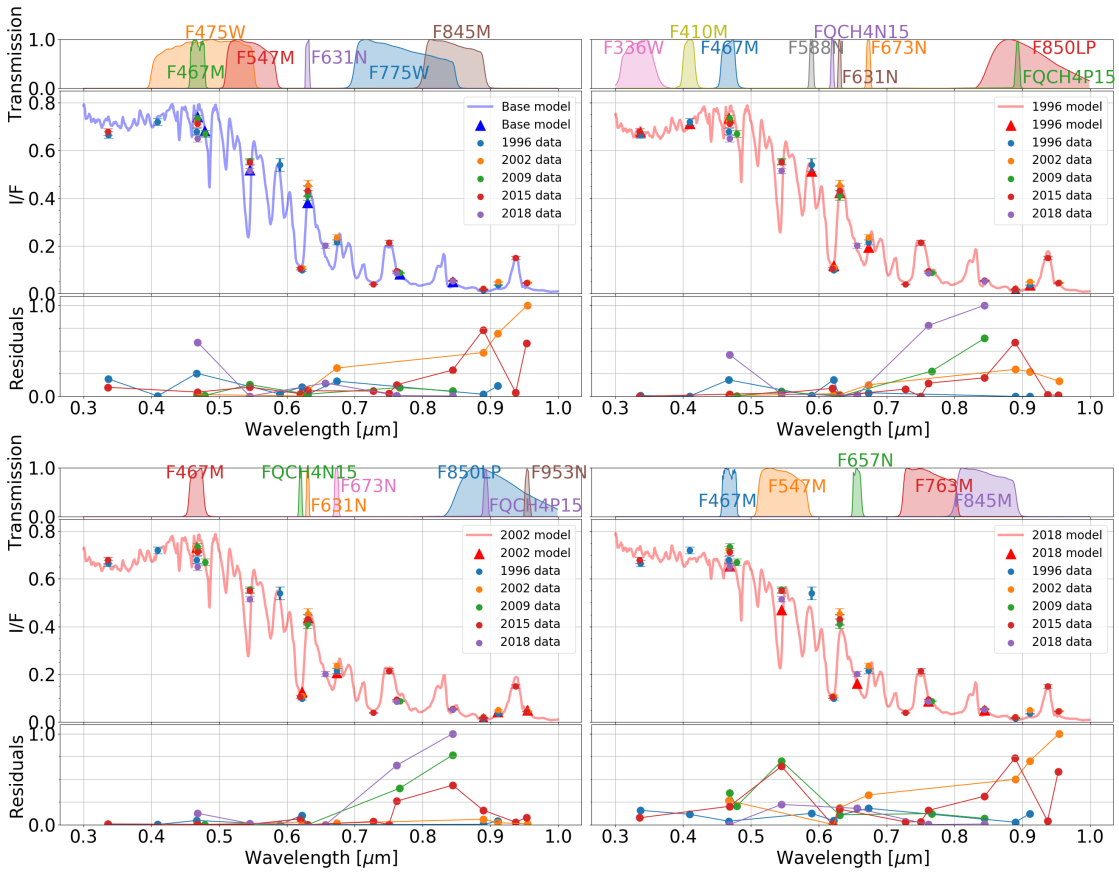

Figure 7.9: **Modeled spectra for band 20°N-50°N.** The 2009 base model is plotted in the blue line (top left). The best fitting models for 1996 (top right), 2002 (bottom left) and 2018 (bottom right) are plotted in red. Circles are the data points extracted from the reference years, each color corresponds to the year specified in the legend. The triangles represent the model values in filters that imaged Neptune in the model's year, obtained by convolution of the model with the filter bandpasses, plotted above the spectrum. Uncertainties include both random and photometric errors (Section 3). Beneath each spectrum, residuals $(r_i/\sigma_{\rm obs})^2$ between convolved and data points are normalized with respect to the largest residual value found in all years with respect to the considered model and they are displayed for each year, following the same color map of the data points legend.

providing essentially the same χ^2 value. This is not the case for years after 2002, in which measurements do not match the expected reflectivities.

While looking for a better fitting model for 2002, we also found one for 1996 (top right of Figure 7.9): $P_{{\rm max},\beta} = 3.0^{+0.6}_{-0.2}$ bar, hence a higher lower haze layer with respect to the 2009 base model, reduces the difference with the observed I/F, particularly large for $\lambda = 0.366$ μm, $\lambda = 0.467$ μm and $\lambda = 0.673$ μm. The fit is also the best for 2015 with respect to the 2009 base model. On the contrary, all other years are not fitted with the 2002 spectrum.

For 2018, the 2009 reference spectrum outputs reflectivities whose discrepancies with data are larger for blue and F657N filters. We found a better model (bottom right of Figure 7.9) by setting the constant part of the lower haze single scattering albedo to $0.965^{+0.009}_{-0.010}$. The obtained model agrees also with 1996 and 2015, though returning worse χ^2 values with respect to the 1996 model.

An average increasing behavior is seen for this band in 1994-2002 for both reference filters. For later years, the linear fit is consistent with a constant trend, again for both filters. 2002, as well as 2018, hints at a different vertical structure with respect to 2009. In addition, the RT modeling does not rule out the possibility of having the same vertical structure in 1996 and 2002.

8

Discussion

This Chapter provides a comparison between the results we achieved through the radiative transfer modeling and previous literature focused on Neptune's vertical structure. We first discuss the differences of our findings with respect to variations between latitudinal bands in Section 8.1. Subsequently, the temporal variation we found is compared with antecedent analogous works in Section 8.2

8.1. Comparison with previous works on spatial variation

The results of our radiative transfer modeling for 2009 spatial variations highlight a different vertical structure between latitudinal bands south of 30°S and north of it. The difference is seen in the lower haze layer maximum pressure level and the tropospheric methane mixing ratio. For the northern part, we found an optically thick ($\tau_\beta = 2.2^{+0.7}_{-0.3}$ at $\lambda = 0.75$ μm) haze, whose particles' retrieved single scattering albedo has a spectral dependence seen in Equation 7.3, constant longward of $\lambda = 0.65$ μm. The haze is based at $P_{\max,\beta} = 4.1^{+0.4}_{-0.2}$ bar and the tropospheric methane mixing ratio amounts to $0.050^{+0.009}_{-0.012}$. For the southern regions, an analogously optically thick haze was found, with the same ω_β. However, the best fitting model favors a shallower pressure base at $P_{\max,\beta} = 3.4^{+0.2}_{-0.2}$ bar and a methane depleted troposphere with $X_{CH_4,t} = 0.030^{+0.005}_{-0.008}$.

The vertical structure for 2009 is sketched in Figure 8.1 in the third panel. The two layers are based at the retrieved respective maximum pressure. As input in the model, the hazes extend up to the upper boundary of our model atmosphere (10^{-5} bar). However, the effective extent of the two layers is set by their respective fractional scale height. We considered the upper boundary of each layer to be the pressure level where τ is reduced by a factor of $1/e$. With this definition, the optically thin upper haze extends up to 0.27 bar, equal for all latitudinal bands. The lower layer can be effectively considered a cloud, meant as an optically thick haze, with its top near 2.95 bar south of 30°S and 3.7 bar north of it. This is most likely the top of the H_2S cloud layer (de Pater et al., 2014).

Our 5°N-20°N band includes the latitudinal band analyzed in the NIR by Luszcz-Cook et al. (2016), who performed radiative transfer modeling with a previous version of SUNBEAR to characterize the aerosol structure at 2°N-12°N from 2009 data. With this work, we share several parameters: fractional scale height, distribution's peak radius, gas abundances, temperature-pressure profile. Their retrieved 2L_DISORT model had an optically thin ($\tau = 0.019$ at 1.6 μm) upper haze layer, comparable to what we found at visible wavelengths (0.03). We located it at the same pressure level (0.6 bar). Nonetheless, the scatterers properties are significantly different. The single scattering albedo of the particles was found to be 0.91 and their phase function was modeled through the single Henyey-Greenstein parameter g. Using the single parameter, we would have found a similar ω_α (0.9). Nonetheless, unlike them, we adopted a double parameter phase function, based on the work at visible wavelengths done by Karkoschka and Tomasko (2011), leading to the best fit with $\omega_\alpha = 0.4^{+0.2}_{-0.2}$. Regarding the lower haze, Luszcz-Cook et al. (2016) placed its base at 3.3 bar, shallower than ours, and found it to be optically thicker than the upper layer, in agreement with what we found. The numerical value of τ is not comparable as different wavelengths are investigated. Again, major discrepancies are seen for the scatterers, whose $\omega_\beta = 0.45$ is lower with respect to ours. The 2L_DISORT model is based on limb-darkening regions. Our analysis geometry and dark region location is closest to their location D (5°N) dark region, whose retrieved parameters are close to the discussed 2L_DISORT model. However, for this region, in addition to the agreement with respect to the upper haze, located at the same pressure level,

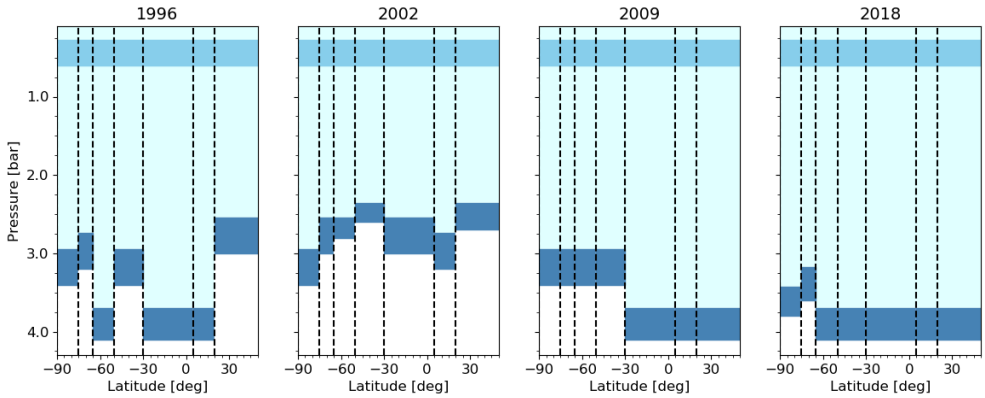

Figure 8.1: **Latitudinal vertical structure for all bands in 1996, 2002, 2009 and 2018.** The optically thick lower haze layer (dark blue) can be effectively considered a cloud. The upper boundary corresponds to the pressure value where the value of τ at the base of the layer is reduced by a factor of e. The same applies for the upper haze layer (light blue). The faint blue background indicates that the haze layers' upper boundary is not fixed, but extends up to the end of the atmosphere.

the pressure base upper boundary of the lower haze (4.0 bar) corresponds essentially to ours (4.1 bar) within error bars.

The aerosol analysis of Luszcz-Cook et al. (2016) is not limited to their 2°N-12°N band, but it is extended to latitudes from the South Pole to 20°N, as displayed in their Table 5. However, the pressure levels numerical values are affected by the wavelength region investigated, so that we cannot make a strong comparison with our findings. Looking at the pressure trend with latitude, the upper haze layer was found to be placed at deeper pressures (1.7-2.2 bar) at latitudes south of 21°S with respect to northern regions (0.3-1.2 bar). We did not find this trend, though this is not evidence of disagreement. Indeed, wavelengths at which OSIRIS provided observations (1.47-2.38 μm) are more sensitive to larger particles in the atmosphere with respect to HST measurements (0.3-1.0 μm), affecting the observed trend: being more sensitive to upper hazes leads to see changes in these. The differences seen for the upper haze inevitably affects the retrieval of the lower haze, so that a comparison is prevented.

The other major latitudinal spatial variability study is provided by Karkoschka and Tomasko (2011), based on HST-STIS data from 2003. The vertical structure proposed by the authors is different, as they model the atmosphere with a stratospheric discrete aerosol layer, extending from 0.13 bar to higher altitudes, and a tropospheric semi-infinite haze, whose upper boundary is set to 1.4 bar. The latitudinal variation is seen in parameters such as the optical depth per bar, seen to be largest where insolation is stronger. We retrieved a constant optical depth for all latitudes. This might be due to the fact that we favored a two-discrete-layer structure and we found better fits with the change of aerosols pressure bases, rather than with optical depth. Karkoschka and Tomasko (2011) also found methane abundance to be constant in its mixing ratio with latitude, but changing in its relative humidity in the 1.2-3.3 bar pressure region. We found instead a deep tropospheric methane mixing ratio to be larger for bands north of 30°S, namely 0.05 instead of 0.03. Both values are included in the range indicated by the authors (0.04 ± 0.01). Nonetheless, we did not account for changes in relative humidity, so that our findings are difficult to compare with Karkoschka and Tomasko (2011)'s.

Along with pressure, we saw latitudinal variations for the tropospheric methane mixing ratio, as mentioned above. Tollefson et al. (2019) provides an analysis of spatial trend in methane abundance from temperature models based on Atacama Large Millimeter Array (ALMA) infrared, visible and centimeter wavelength observations in 2016-2017. They found an increased CH_4 presence in the deep troposphere in their 32°S-12°S and 5°S-20°N bands, depleted for 90°S-50°S, 12°S-2°N and north of 20°N, and intermediate for 50°S-32°S. We found an enhanced methane abundance for latitudes north of 30°S and depleted for the remaining southern latitudes. We thus agree with depletion south of 50°S and enrichment at near-equatorial northern regions (5°N-20°N). The mismatch with the other locations is due to two factors. Firstly, a different band definition is there, so that we saw an enriched methane abundance at 30°S-5°N, which encloses both what Tollefson et al. (2019) saw as an enriched (32°S-12°S) and a depleted (12°S-2°N) band. We then captured an average behavior, resulting in enriched methane, as the largest contribution is given by the more extended enriched band. Secondly, our analysis focuses on background hazes, demanding the removal of bright methane-rich clouds.

Neglecting the contribution to methane abundance of these clouds most likely leads to different conclusions regarding the CH_4 presence.

8.2. Comparison with previous works on temporal variation

The results of our radiative transfer modeling for temporal variations in our latitudinal bands are sketched in Figure 8.1, where the vertical structures we retrieved are displayed for years in which differences are found with respect to the 2009 base model. In years prior to 2009, we saw a more complex structure for the lower haze, whereas the upper haze did not change with time.

We compare our results from 1996 with what Sromovsky et al. (2001b) found by fitting HST data. Their best fitting model implied the presence of a three-layer structure: a stratospheric reflecting layer at 0.1 bar, to account for discrete bright features; an optically thin layer at 1.4 bar; and an optically thicker and reflective layer with the top fixed at 3.8 bar, extending to deeper pressures (~ 7 bar). Cloud-free regions do not have the stratospheric layer. The model was built from disk-averaged reflectivities. Their results might be in line with ours: our latitudinal refined structure allows for pressure tops around 3.7 bar for bands 65°S-50°S, 30°S-5°N and 5°N-20°N, whereas the other bands have pressure tops of $P_{\min,\beta} < 3.0$ bar. However, our pressure tops depend on the definition we gave them, i.e. where the optical depth is a factor of $1/e$ lower, as we assumed an upper boundary equal to the minimum pressure level of our model atmosphere. In addition, the disk-averaged model was built taking into account bright clouds we excluded and pertained to areas not restricted to dark cloud-free regions.

Between 1996 and 2002, we found a general upheaval of the lower cloud to shallower pressure levels, with the exception of the southern polar region. The largest changes ($P_{\max,\beta,1996} - P_{\max,\beta,2002} > 0.8$ bar) are seen for southern mid- and low latitudes (65°S-50°S and 30°S-5°N), as well as low latitudes for the northern (5°N-20°N). These bands are the ones characterized by a low bright cloud impact (see Figure 5.1). On the contrary, latitudes where bright clouds were mainly seen, i.e. 75°S-65°S, 50°S-30°S and 20°N-50°N, have lower hazes lifted no more than 0.2 bar.

The motion of this haze layer might be correlated to the strong cloud activity we saw in 2002: a more vigorous convective motion could have taken place at that time, driving clouds to higher tropospheric altitudes. To corroborate this scenario, we noted that the location of the lower haze returns to deeper pressure levels in 2009 for all latitudes. In this year, bright clouds are reduced to a minimum with respect to all other years, as it can also be seen in Figure 3.2, panel 4. The largest drops ($P_{\max,\beta,2009} - P_{\max,\beta,2002} > 0.9$ bar) in altitude are seen for bands north of 30°S.

The changes from 2009 to 2018 are less dramatic than for other years. In fact, we saw no changes for bands 30°S-5°N and 5°N-20°N. The pressure base is also maintained for band 20°N-50°N, but a different lower haze's single scattering albedo spectral dependence is found, with an overall decrease of 0.02. This is the case also for bands 65°S-50°S and 50°S-30°S, where ω_β is lowered by 0.015 and 0.01, respectively, along with a deeper pressure base of the haze itself. The polar regions' (90°S-75°S and 75°S-65°S) lower haze is also located to lower altitude, $P_{\max,\beta,2018} = 3.8^{+0.2}_{-0.2}$ bar and $P_{\max,\beta,2018} = 3.6^{+0.1}_{-0.1}$ bar, respectively. From Figure 3.2, we noticed that in this year, as seen in 2009, cloud activity is limited and could be the cause of limited changes in the atmosphere. Nonetheless, the relatively large decrease of the scatterers albedo might be related to the appearance of the 2018 Northern Dark Spot at 23°N (Simon et al., 2019).

Karkoschka (2011) did a temporal analysis of changes in background reflectivity, which he referred to as slow variation. He fitted observations from WFPC2 between 1994 and 2008 with radiative transfer modeling, using the vertical structure from Karkoschka and Tomasko (2011). With his semi-infinite dark lower haze layer, he hypothesized a downward motion of the dark haze boundary with respect to the stratospheric bright layer at a rate of 1 bar per year. We agree on the fact that the lower haze is settling to deeper pressures, even if we adopted a different vertical structure. This discrepancy affects the found descending rate, which would be too fast with respect to our conclusions. In addition, we saw an inverse motion from 1996 to 2002, then reversed toward 2018. We confirm the settling behavior for the 10 years we add with respect to Karkoschka (2011). The trend ought to be better constrained with future observations of dark regions and their RT modeling.

9

Conclusions and recommendations

The last Chapter of this work is dedicated to the conclusions drawn from the presented analysis. Section 9.1 reports the research questions formulated in Section 2.2 and the answers deduced from the conducted study. Section 9.2 points out caveats and possible future work on the matter, in order to further deepen our knowledge about Neptune's hazes.

9.1. Conclusions

In this Section, the research questions are repeated for convenience. For each of them, the answer is provided, following the results achieved with the analysis presented in the previous Chapters.

1. How does Neptune's hazes brightness trend at visible wavelengths change in the last 10 years with respect to previous years?

   (a) How has reflectivity changed over time globally, i.e. in a disk-averaged sense?

   Chapter 4 was entirely dedicated to the analysis of temporal trend for global disk-averaged reflectivities, computed in terms of I/F (see Equation 3.1). Two filters were chosen, specifically F467M and F850LP/F845M, so that changes in both blue and methane absorption wavelengths, respectively, are assessed.

   For the blue filter, an increasing behavior of reflectivity is seen between 1994 and 2002, in which a maximum is reached, with a growth of 4.6%. After that, a constant trend is maintained up to 2009. A gap in the data prevents the investigation of the temporal trend between 2010 and 2014. In 2015, the behavior is inverted with respect to earlier observations, and it displays a decreasing slope, with the I/F values dropping by 0.011. These trends can be easily assessed visually (Figure 4.1) and they are further corroborated by the slopes of linear fits made for the 1994-2002, 2004-2008 and 2015-2018 time intervals. Comparing the obtained results to the long-term measurements in Lockwood (2019), converted to I/F, an excellent match is found, taking into account the difference in sensitivity of the filters used for the two datasets. This agreement suggests that what we see is most likely real.

   For the methane filters, brightness was computed both including and not including bright clouds, as these filters cover the strong methane absorption wavelength region, making them sensitive to the methane bright clouds. The two cases led to different results in time. When clouds are taken into account, a steep increasing trend is found from 1996 to 2002, with a 39% growth in I/F. As for the blue filter, 2002 marks a maximum in the investigated time period, and this is caused by the strong cloud activity registered in this year. In 2009-2011, datapoints and linear fits indicate a constant behavior, which is not ruled out also for the successive 2015-2018 period, due to large error bars. The extent of error bars is caused by the short-timescale evolution of cloud features. Indeed, when excluding the contribution of clouds, error bars are reduced. The removal of bright features was implemented through a routine (see Appendix A) that excludes pixels in the planetary images for the computation of the mean reflectivity value. Clouds can affect this value up to a factor of 1.5. When neglected, the increasing behavior found for 1996-2002 is not there anymore.

Data for the 2009-2011 period show constancy as well, whereas the most recent period (2015-2018) is consistent with decreasing reflectivity.

(b) How has reflectivity changed over time locally, i.e. looking at specific latitudinal bands?

The topic of Chapter 5 concerns the temporal trend of reflectivities in its latitudinal variations. The same two filters were adopted as in Chapter 4. Necessary condition for this analysis is a thoughtful subdivision of the planetary disk in latitudinal bands. The bands were chosen on the basis of the impact that bright clouds have on reflectivity, in order to resemble the banded structure of the planet itself. We divided the surface in 7 latitudinal bands, spanning from the South Pole to 50°N. For each of them, the average I/F was computed.

The latitudinal results for the blue filter show three distinct trends that allowed to divide the whole period into three time intervals. In 1994-2002, all bands display an increasing trend, with the largest changes in reflectivity seen for southern mid-latitudes (bands 65°S-50°S and 50°S-30°S), whereas the lowest variability is noticed for near-equatorial latitudes (bands 30°S-5°N and 5°N-20°N), in line with previous studies (Sromovsky et al., 2001d; Karkoschka, 2011). In 2004-2008, most of the latitudinal bands' behaviors are consistent with a constant I/F value, with the exception of near-equatorial latitudes, in which a slight increase is seen, as well as for 75°S-65°S, that, on the contrary, displayed a decreasing trend. Confirmations come from the works of Karkoschka (2011) and Karkoschka and Tomasko (2011). In 2015-2018, the trend stays constant for most of the bands, though the northernmost latitudes (20°N-50°N) agree with a decreasing behavior. This period is added to previous similar analysis, which were limited to 2008.

In the methane filter, reflectivities were computed after having removed bright clouds. A similar subdivision in time intervals was implemented. In 1996-2002, similar conclusions as for the blue filter apply: southern mid-latitudes are the ones where the I/F values change the most, along with the northern band (20°N-50°N). These findings agree with Sromovsky et al. (2001d), but are somewhat different from Karkoschka (2011), who found constancy at all latitudes, perhaps due to different cloud removal technique and band definition. In 2009-2011, all bands are consistent with a constant reflectivity, and this is a new result as the time period covered by previous studies (Karkoschka, 2011) is limited to 2008. In 2015-2018, a decreasing behavior is seen in the I/F values for southern near-polar (bands 90°S-75°S and 75°S-65°S) and mid- to low latitudes (bands 50°S-30°S and 30°S-5°N). The other bands show a constant trend. Conclusions for these years are also new.

Focusing on the last 10 years, the planet has shown a global decreasing brightness at blue wavelengths, which is the average of the trend seen in the disk breakdown in latitudinal bands. Indeed, the majority of them display a trend consistent with constancy, with the exception of the northernmost band 20°N-50°N, which in turn shows a drop in I/F values. With respect to years prior to 2015, the behavior seems to have inverted, as a steady growth was seen until 2002, followed by a constant I/F both in a global sense and in most bands. Concerning methane absorption wavelengths, from 2008 onward, an initial constancy is seen up to 2015 at the latest, when a drop is noticed for global cloud-free reflectivities. The latitudinal behavior is in line with what is seen globally, as a constant brightness is also maintained for all bands up to 2015, when southern near-polar and mid- to low latitudes display a drop in I/F values.

2. What is the best fitting vertical structure model that agrees with visible data we collect from the whole HST mission time period?

(a) How does the vertical structure change at different latitudes?

Section 7.1 is dedicated to the radiative transfer modeling results aiming at the spatial variation of the atmosphere's vertical structure. 2009 was chosen as reference year in which to characterize the structure, as it is the same year in which Luszcz-Cook et al. (2016) analyzed infrared data to infer their vertical model, thus providing a meaningful comparison between structures deduced from different wavelengths. Analogously, band 5°N-20°N was chosen as reference latitudinal band, from which to build the model and then compare it to other bands, as it showed an average trend in terms of temporal reflectivity variations.

The input parameters for the radiative transfer model are several and the majority of them was retrieved from literature (Sromovsky, 2005; Karkoschka and Tomasko, 2009, 2010, 2011; Sromovsky et al., 2012; Fletcher et al., 2014; Luszcz-Cook et al., 2016; Molter et al., 2019). The two-layer model was adopted, considering the pressure levels, single scattering albedo of particles and total optical depth of each haze, along with the tropospheric and stratospheric methane mixing ratio, as free parameters allowed to be changed in finding the best fitting model, since these parameters were also used by previous radiative transfer analyses (Karkoschka and Tomasko, 2011; Luszcz-Cook et al., 2016). The evaluation of the goodness of fit between output spectrum and empirical reflectivity values was done through the reduced χ^2 test (see Equation 7.1).

The vertical structure retrieved reveals a division of the planetary disk in two parts. For all bands, an upper haze is placed at 0.6 bar, and found to be optically thin ($\tau_\alpha = 0.03^{+0.02}_{-0.02}$ at 0.75 μm) and formed by low scattering albedo ($\omega_\alpha = 0.4^{+0.2}_{-0.2}$) particles. Also, a constant stratospheric maximum methane mixing ratio ($X_{CH_4,s} = 0.0006^{+0.0394}_{-0.0006}$) fits all latitudes. Changes are seen for the lower haze layer. Latitudes south of 30°S are best described with an optically thick ($\tau_\beta = 2.2^{+0.7}_{-0.3}$) lower layer located at $P_{\max,\beta} = 3.4^{+0.2}_{-0.2}$ bar, with aerosols having a single scattering albedo ω_β dependent on wavelength shortward of 0.65 μm (see Equation 7.3) and constantly equal to 0.85 for longer wavelengths. In addition, the deep tropospheric methane mixing ratio is found to be $X_{CH_4,t} = 0.030^{+0.005}_{-0.008}$. This structure does not agree with data from latitudes north of 30°S, where the best fitting model preserves the same optical depth and single scattering albedo, but demands a deeper lower haze, with base at $P_{\max,\beta} = 4.1^{+0.4}_{-0.2}$ bar, and an enriched deep tropospheric methane mixing ratio ($X_{CH_4,t} = 0.05^{+0.009}_{-0.012}$).

(b) For each latitudinal band, how does the structure change in time?

The temporal change in vertical structure is investigated in Section 7.2. The models found for the various latitudinal bands in Section 7.1 were adopted as reference models for the considered latitude. Only the aforementioned free parameters were allowed to change in finding the best fitting model.

Between 1996 and 2002, all latitudes saw an uprising of the lower haze layer, with the largest changes (more than 0.8 bar) seen in bands where we found a low presence of bright clouds, i.e. southern mid- and low latitudes (bands 65°S-50°S and 30°S-5°N), and northern low latitudes (band 5°N-20°N). Other bands in which a stronger cloud activity was seen in these years are fitted with lower hazes lifted up by no more than 0.2 bar. This upheaval of the lower haze might be related to the strong cloud activity seen in 2002.

Between 2002 and 2009, an overall settlement of the lower haze took place, bringing down the haze to the pressure values seen in the previous research question. The largest drop is registered for bands north of 30°S, amounting to more than 0.9 bar.

Less dramatic changes are found between 2009 and 2018. No changes at all are seen for bands north of 30°S in terms of pressure base. Nonetheless, the northernmost band requires a different single scattering albedo spectral dependence, shifted by 0.02 shortward of 0.65 μm. A similar change is seen for the southern mid-latitudes (bands 65°S-50°S and 50°S-30°S), with a drop in ω_β of 0.015 and 0.01, respectively, again shortward of 0.65 μm. The subsidence of the lower haze has continued for near-polar regions (bands 90°S-75°S and 75°S-65°S), where the drop in altitude corresponds to a pressure base at $P_{\max,\beta} = 3.8^{+0.2}_{-0.2}$ bar and $P_{\max,\beta} = 3.6^{+0.2}_{-0.2}$ bar, respectively.

From the temporal trend analysis and the radiative transfer modeling results, it is clear that 2002 is an outlier year. The peak seen in both reference filters in disk-averaged measurements, as well as the local maxima seen in most latitudinal bands, again in both filters, all correspond to this year. This is likely to be correlated to the strong atmospheric activity noticed, which seems to affect also the background lower haze, lifting it up to shallower pressure levels.

The reflectivity trend over time is modeled by changing the pressure base of the lower haze and its single scattering albedo spectral dependence. In fact, the increasing reflectivity in 1996-2002 is accounted for with an upward motion of the lower haze lower boundary. On the contrary, the drop in I/F in 2002-2009

is best explained with the subsidence of the lower haze. The slower drop in brightness seen for 2009-2018 is also modeled with a slight settlement of southern polar regions lower hazes, coupled with the decrease of scattering albedo of particles forming the lower aerosol layer.

A provisional conclusion could be that the change in brightness is ascribed to changes in location and scattering properties of the lower haze, in a two-layer vertical structure. In particular, increases in reflectivity are the consequence of a vertical motion to shallower pressure levels of the lower layer, whereas decreases in I/F are due to an opposite motion, either coupled or not with the decrease in scattering albedo of lower aerosol's scatterers.

The results of this work confirm that a best fitting model of Neptune's dark regions vertical structure is not unique, neither in space nor in time. In fact, in our spatial variation, different models in agreement with data are found, comprising of lower haze layers displaced with respect to each other and with different tropospheric methane abundances. Similarly, the structure is not maintained throughout the analyzed time interval, but it is subject to significant changes, pertaining to the lower haze vertical location and scatterers properties.

In conclusion, Neptune's dark regions vertical structure is space and time dependent and it is driven by the physical properties of the lower haze layer, namely pressure levels of its base and single scattering albedo of the particles it is made of, as well as the tropospheric methane mixing ratio.

9.2. Recommendations

As final Section of this study, several recommendations are made in order to correctly interpret the results and conclusions presented, pointing out possibilities for future work for the scientific community.

1. *Additional observations of Neptune are needed to continue the long-term analysis.*

   The work done is only the beginning of what should be a proper long-term monitoring of Neptune. The nearly 25 years we analyzed are only a small part of the 165-years planet's orbital period, so that its seasonal changes are not fully understood yet, as only a small part of the Neptunian year has been monitored. A continuous measurements collection in the future should be guaranteed, in order to elaborate on new observations and verify previous conclusions. For example, what will happen in the next years? For how many years will the planet darken and when will this trend stop and/or reverse? These questions can only be answered by waiting and carefully observing and noting down these changes throughout the years, to understand the underlying mechanism driving the phenomena we see in the long-term picture.

   In addition to future observations, it would be beneficial to have a more frequent cadence of these measurements. It was pointed out that in 2011-2014 no data was recorded by HST and, as a consequence, it is unknown what happened in these years. It cannot be assessed whether the constant trend in reflectivity seen e.g. in the methane filters is prolonged until 2015, or an immediate drop occurred right after the last available date, followed by a subsequent increase.

2. *A larger number of wavelengths should be investigated to better constrain the planetary spectrum.*

   The years investigated for the radiative transfer modeling had at least 5 different filters that imaged Neptune. The higher the number of wavelengths at which the planet is seen, the better constrained the planetary spectrum is. In fact, more numerous and more spread empirical values would help to find a better fitting model. For example, 2009 did not provide observations for $\lambda < 0.4$ μm, so that no reference data could be used to have a more accurate spectrum in this region. Indeed, the base models found for 2009 have larger expected reflectivities with respect to the observed I/F at F336W registered in 1996 and 2015. If all years had the same, widespread number of filters, the modeling would have been more accurate due to the more stringent requirements. 2015 is a good example in this sense, not only because of the 12 filters that provided observations, but also thanks to the specific wavelengths investigated, corresponding to absorption features and peaks.

The larger number of wavelengths would be ideal not only referred to the visible wavelengths region investigated, but also in a wider range. From literature, it was noticed that the vertical structure models were inferred from different wavelengths, e.g. infrared or visible. A possible future work would be to analyze a wider range, spanning two or more of these regions. This would allow to construct a single vertical model from a larger number of wavelengths that are sensitive to different pressure levels. Therefore, a broad coordinated multi-wavelength study would help to better characterize the atmospheric structure.

3. *A more accurate wavelength dependence of the single scattering albedo is needed to better represent the real scattering properties of deep aerosol particles.*

   To find a good fitting spectrum for our visible data, a new empirical parameterization for the single scattering albedo of the lower haze's scatterers was introduced. This approach was also adopted in the past (Karkoschka and Tomasko, 2009, 2011). The fact that the analytical formulation proposed provides a satisfactory match with our data does not imply that the newfound spectral dependence is correct. Previous studies (Baines and Hammel, 1994; Sromovsky et al., 2001b; Karkoschka and Tomasko, 2011) confirm that for wavelength longward of 0.6 μm, the single scattering albedo should drop from its unity value assessed for shorter wavelengths. However, the proposed numbers are tentative quantities referred to specific wavelengths.

   In addition, the purpose of the new formulation was solely to fit data in the easiest way. We noticed that the mismatch started around 0.65 μm and, by trial and error, a constant value of $\omega_\beta = 0.85$ allowed for a better solution, so that we adopted this value. It was subsequently verified that this value is close to the proposed ones from former studies (e.g. Sromovsky et al., 2001b). A further refinement of the dependence should be done, based also on physical properties of aerosol particles and laboratory analyses, not only on a mere good fit with planetary brightness data, in order to obtain a smoother transition of the ω value throughout the wavelengths. Indeed, our formulation shows an abrupt discontinuity at 0.65 μm, which might not be its real behavior.

4. *Radiative transfer parameter degeneracy should be investigated.*

   In the radiative transfer modeling part, the issue of parameter degeneracy was treated. Essentially, similar results in expected reflectivity are achieved with changes either in one or another input parameter. Currently, the problem is still open and the best way to avoid it is to build on previous works in which higher spectroscopic resolution have been used. For example, the fact that Karkoschka (2011) prioritized the change in methane mixing ratio and single scattering albedo led us to first look for the best fitting modeling varying these parameters. Nonetheless, this is no guarantee that Neptune's hazes are actually undergoing a change in their methane abundance or scattering properties. Therefore, our findings are bound to the subjective choice of modeling pressure levels and methane abundance, which is perhaps one of the possible scenarios occurring and does not rule out other possible explanations. This is the reason why the vertical structure is still debated and multiple proposal have been made on the basis of remote sensing data.

   More detailed observations would be provided by an orbiter around Neptune, thanks to the more numerous viewing geometries and illumination conditions with respect to remote sensing from Earth. Moreover, *in situ* measurements from a probe through the atmosphere would help to have more information on the clouds particles, temperature-pressure profile and species abundances, better constraining the vertical structure of the planet.

Acknowledgements

Data were obtained from the Data Archive of the NASA/ESA Hubble Space Telescope at the Space Telescope Science Institute, which is operated by the Association of Universities for Research in Astronomy, Inc., under NASA contract NAS 5-26555. This research was supported in part by NASA Grant NNX16AK14G through the Solar System Observations (SSO) program to the University of California, Berkeley. We would like to thank Edward Molter, whose crucial help made this work possible. Invaluable help came also from Michael H. Wong, Joshua Tollefson and Statia Luszcz Cook, for the HST images processing and RT modeling with SUNBEAR.

A

Cloud removal technique

As seen in Figure 3.2, the reflectivity in methane filters is sensitive to bright clouds. To isolate the contribution to the photometric measurements of the dark background hazes we are interested in, we applied the following cloud removal routine, in order to automatize the identification of bright clouds, given the large number of available images.

For each year, we constructed a map of the median values of pixels in each (x,y) coordinates location on the visible planetary disk, as the one in Figure A.1. We then selected specific dark regions for each year and compute the longitudinal average, in order to obtain a threshold δ_φ for each latitude integer value φ. When the value of a certain pixel at latitude φ is larger than $\delta_\varphi + 2\sigma_\varphi$ for its latitude, it is considered as part of a bright cloud, and thus neglected in the I/F cloud-free computation. σ_φ is the standard deviation of the pixels at latitude φ, longitudinally averaged to extract δ_φ.

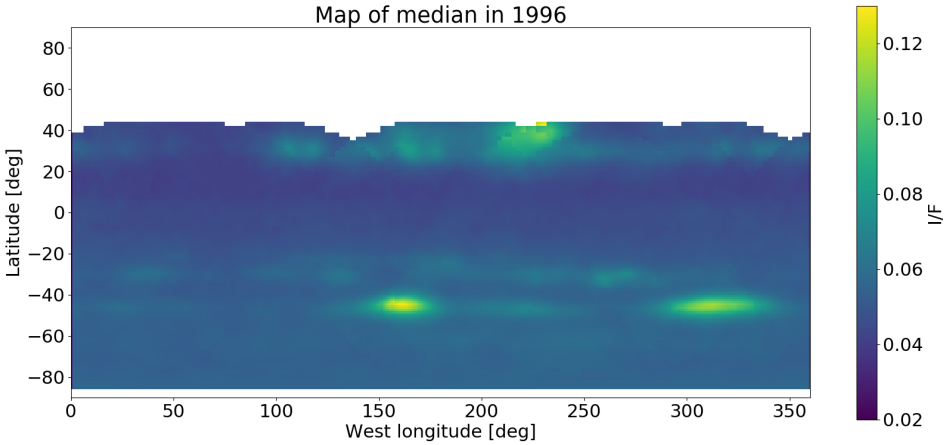

Figure A.1: **Planetary map of median I/F values for each planetographic longitude-latitude location in 1996.** The map is constructed through the computation of the median value at given coordinates (pixels) from all 1996 images having the specified coordinates visible on the planetary disk. In this year, we have a complete longitudinal coverage. Artefacts are noticed, namely the curve lines resembling the edge of the deprojected planetary disk (e.g. in 30°N-50°N latitude and 220°W-240°W longitude).

As an example, consider 1996, whose median map is plotted in Figure A.1. Two fact are underlined. Firstly, the map displays artefacts caused by the edges of the deprojected planetary maps, stitched to obtain the map itself. Secondly, clouds are visible, marking regions of prolonged strong cloud activity, i.e. where clouds are seen in most images of this year. These two issues do not allow to use the median value for each pixel as

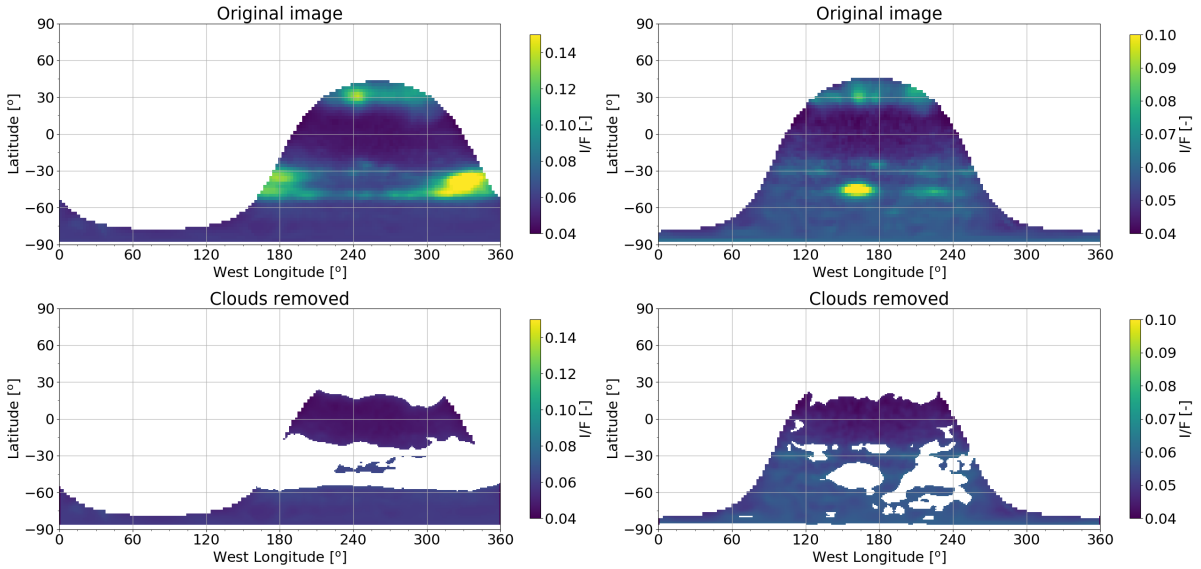

(a) **High cloud presence scenario.** The Minnaert-corrected image before (top right) and after (bottom right) the removal shows the effect of the routine. The clouds seen in the mid-latitudinal region of the southern hemisphere (60°S-30°S), as well as the bright feature at 30°N, are replaced with blank spaces and ignored in the brightness computation. The image was taken on 10th August 2002.

(b) **Low cloud presence scenario.** The Minnaert-corrected image before (top right) and after (bottom right) the removal shows the effect of the routine. The prominent bright cloud, as well as the fainter and thinner feature at 45°S, along with the bright bands at 20°S and 30°N, are replaced with blank spaces and ignored in the brightness computation. The image was taken on 13th August 1996.

Figure A.2: **Cloud removal technique implementation for high and low cloud presence.**

threshold between bright clouds and dark background hazes. The visible edges in the map have a median value that is artificially lower than the surroundings. As a result, if we were to use medians as thresholds, we would eliminate pixels that are effectively representative of the dark background hazes. On the other hand, bright regions have the opposite problem: their median is larger than values from dark regions, so that pixels might be incorrectly considered as part of the dark background, while belonging to a cloud instead. This can occur when the bright region is subject to short-term brightness variations: a pixel whose value is smaller than the median I/F in its location can be part of a cloud darker edge. To avoid this occurrence, dark regions are selected from the median map. In the 1996 case, the selected region is between 0°W and 75°W, spanning all (visible) latitudes. For each latitude, an average value is computed from the pixels in the dark region's longitudes at the considered latitude: this is what was previously called δ_φ. The standard deviation of these pixels is what was referred to as σ_φ. In conclusion, the routine checks all pixels on the map: if a pixel's value is greater than $\delta_\varphi + 2\sigma_\varphi$, the pixel is considered part of a bright clouds. On the opposite, if $I/F \leq \delta_\varphi + 2\sigma_\varphi$, the pixel is included in the reflectivity computation, as it is considered to belong to the dark background hazes.

Figures A.2a-A.2b display two representative cases in which the routine was implemented. Figure A.2a shows the removal applied to a high cloud presence image. The image is taken from 2002, a year marked by an anomalously strong cloud activity, especially in southern mid-latitudes (60°S-30°S). The abundance of bright clouds can be assessed qualitatively from the top image, displaying the Minnaert-corrected (Equation 3.2) planetary surface deprojection. As expected, the southern mid-latitudinal region is dominated by bright clouds. There is also a bright feature at 30°N, accompanied by a fainter and more extended cloud. The bottom image is the result after the removal of clouds, substituted with blank pixels, ignored in the computation of mean cloud-free and latitudinal reflectivities. The dark regions left are 90°S-60°S and 15°S-15°N, with a small zone around 40°S not covered by clouds.

Figure A.2b is similar to Figure A.2a but for an image with less bright discrete clouds in it. The lower presence of clouds is visible in the original (top) image. The planetary disk displays a prominent bright cloud roughly centered at 150°W longitude and 45°S latitude. With it, on the same latitude, we have a fainter and thinner feature (~ 225°W longitude). A northern band with sparse small clouds is also noticed at ~ 20°S latitude. Lastly, on the northernmost location (30°N), we see another bright region. Differently from Figure

A.2a, the number of bright pixels is lower, so that the processed map displays less extended removed-pixels regions.

The effect of the cloud removal is apparent in Figure 4.2. The black data, corresponding to the cloud-free average I/F, are lower than the disk-averaged reflectivity cyan data (inclusive of clouds) by a factor of up to 1.5.

The cloud removal technique is also used to remove clouds in all measurements coming from high background/clouds contrast images, corresponding to images taken in filters whose peak wavelength was larger than 0.6 μm, with the exception of F631N and F657N, where clouds are not visible. These measurements are used in the radiative transfer modeling part of the work.

B

Filters' bandpasses

WFPC2 and WFC3 have different filters. Whereas the blue filter is present on both cameras, with essentially the same peak wavelength ($\lambda_{\text{peak}} = 0.467$ μm), there is no common filter in the methane absorption band. The closest similarity is found between F850LP and F845M, since their sensitivity falls into the 0.84-0.93 μm window of methane absorption. Nonetheless, the performances of these methane filters differ significantly. Figure B.1 displays the transmission curves of the two filters, plotted on top of the 2009 base model for 5°N-20°N (black line), as a function of wavelength. The orange curve refers to F850LP (WFPC2), the blue curve represents F845M's (WFC3) transmission. For the two filters, the peak transmission is reached at different wavelengths, specifically at $\lambda = 0.911$ μm and $\lambda = 0.845$ μm, respectively. Moreover, the spectral range covered has just a limited overlap, between 0.84 μm and 0.90 μm. As a result, the filters are sensitive to different parts of the spectrum.

In order to correct for the discrepancy between the two methane filters, and thus to allow for a direct comparison between the measurement sets, we computed the ratio in the convolved model values. The spectrum convolution allows for a one-to-one comparison between the measurement taken from a broadband filter and the value expected from the model. The filter observation is the result of a range of wavelengths, thus not only pertaining to a single λ. It is a weighted mean of the reflectivities seen in this range, where the weights are given by the transmission curve values corresponding to each wavelength: the largest transmission corresponds to the peak wavelength of the filter. The wavelength corresponding to the convolved reflectivity is called the effective wavelength of the filter λ_{eff}, i.e. the weighted average of the wavelengths covered by the filter, again with transmission values as weights. Analytically:

$$\text{I/F}_{\text{conv}} = \frac{\sum_{i=0}^{N} \text{I/F}_i \cdot t_i}{\sum_{i=0}^{N} t_i} \tag{B.1}$$

$$\lambda_{\text{eff}} = \frac{\sum_{i=0}^{N} \lambda_i \cdot t_i}{\sum_{i=0}^{N} t_i} \tag{B.2}$$

where I/F_{conv} is the convolved reflectivity, I/F_i and t_i are the reflectivity and filter's transmission for λ_i in the wavelength range covered by the filter itself. Convolving the spectrum from 2009 found with our radiative transfer modeling (base model, see Section 7.1) for the two filters brings to a ratio $\frac{\text{I/F}_{\text{conv,F850LP}}}{\text{I/F}_{\text{conv,F845M}}} \approx 1.65$. This means that, in the 2009 model, the reflectivity seen by F850LP is a factor of ~ 1.65 lower with respect to F845M. Hence, we corrected measurements prior to 2009 (i.e. taken from WFPC2's F850LP) by multiplying them by this factor. When computed with respect to models of other years and latitudinal bands, the corrective factor is within a 2.5% range.

An analogous approach is used to motivate the discrepancy between Lockwood (2019)'s *b*-magnitude data and our HST's F467M measurements. Looking at the transmission curves of the considered filters (Figure B.2), i.e. WFPC2's F467M and Lowell's *b*-magnitude, the convolved point for the *b*-magnitude filter at Lowell Observatory used by Lockwood (2019) is a factor of ~ 1.01 larger than HST, so that it is sensitive to higher I/F values with respect to HST. Hence, his results are larger than ours, as seen in Figure 4.1 and the ~ 0.005 difference in between the two data sets is accounted for.

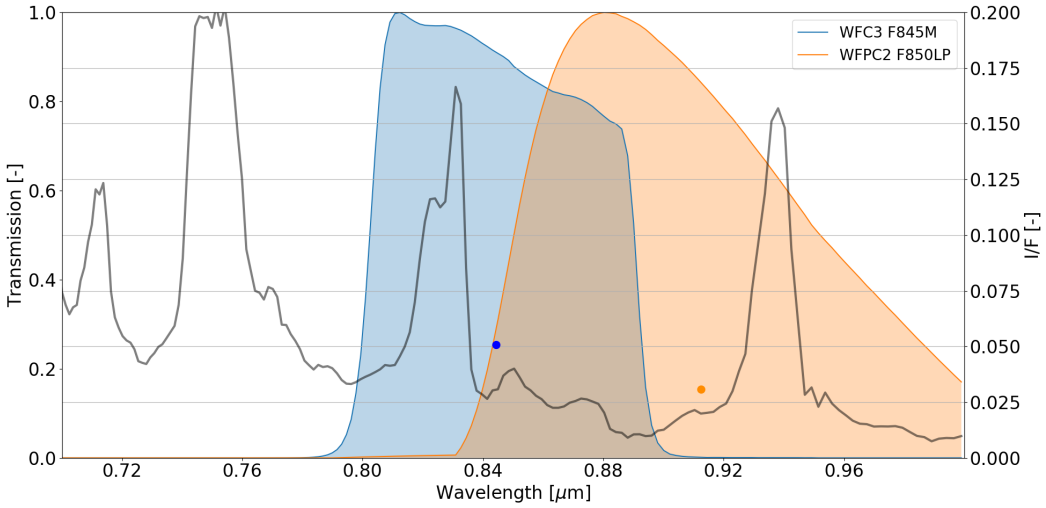

Figure B.1: **F850LP and F845M filters transmission curves.** Transmission curves of both methane filters are plotted: F850LP (orange) and F845M (blue). On top of them, the band 5°N-20°N 2009 model spectrum of Neptune (black line) is reported. The points represent the convolved model values. The left y-axis represents the transmission values of the filters. The right y-axis indicates the reflectivity for the spectrum and convolved points.

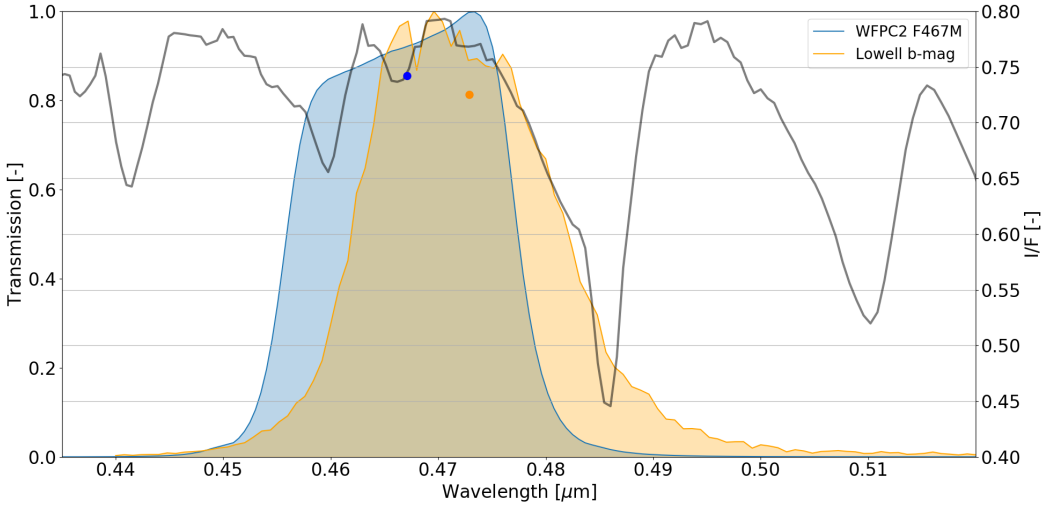

Figure B.2: ***b*-magnitude and F467M filters transmission curves.** The image format is the same as Figure B.1: WFPC2 blue filter's (blue) and Lowell's *b*-magnitude filter (orange) transmission curves are plotted on top of the band 5°N-20°N 2009 model spectrum (black line). The points represent the convolved model values. The left y-axis represents the transmission values of the filters. The right y-axis indicates the reflectivity for the spectrum and convolved points.

Bibliography

Ádámkovics, M., Mitchell, J. L., Hayes, A. G., Rojo, P. M., Corlies, P., Barnes, J. W., Ivanov, V. D., Brown, R. H., Baines, K. H., Buratti, B. J., Clark, R. N., Nicholson, P. D., and Sotin, C., 2016. Meridional variation in tropospheric methane on Titan observed with AO spectroscopy at Keck and VLT. *Icarus* 270, 376-388.

Baines, K. H., and Hammel, H. B., 1994. Clouds, Hazes, and the Stratospheric Methane Abundance In Neptune. *Icarus* 109, 20-39.

Bucholtz, A., 1995. Rayleigh-scattering calculations for the terrestrial atmosphere. *Applied Optics* 34, 2765-2773.

Canny, J., 1986. A Computational Approach to Edge Detection. *IEEE Transactions on Pattern Analysis and Machine Intelligence*, PAMI-8, 6.

Chamberlain, J. W., and Hunten, D. M., 1989. *Theory of Planetary Atmospheres*. Academic Press.

Colina L., Bohlin, R. C., and Castelli, F., 1996. The 0.12-2.5 μm absolute flux distribution of the Sun for comparison with solar analog stars. *The Astronomical Journal* 112, 307-315.

Conrath, B. J., Gautier, D., Owen, T. C., and Samuelson, R. E., 1993. Constraints on N2 in Neptune's Atmosphere from Voyager Measurements. *Icarus* 101, 168-171.

de Kleer, K., Luszcz-Cook, S. H., de Pater, I., Ádámkovics, M., and Hammel, H. B., 2015. Clouds and aerosols on Uranus: Radiative transfer modeling of spatially-resolved near-infrared Keck spectra. *Icarus* 256, 120–137.

de Pater, I., Fletcher, L. N., Luszcz-Cook, S., de Boer, D., Butler, B., Hammel, H., Sitko, M. L., Orton, G. S., and Marcus, P. S., 2014. Neptune's global circulation deduced from multi-wavelength observations. *Icarus* 237, 211-238.

de Pater, I., and Lissauer, J. J., 2011. *Planetary Sciences - Physics, Chemistry and Habitability*, New York: Cambridge University Press.

Dressel, L., 2019. *Wide Field Camera 3 Instrument Handbook*, Version 11.0. STScI: Baltimore.

Fletcher, L. N., de Pater, I., Orton, G. S., Hammel, H. B., Sitko, M. L., and Irwin, P. G. J., 2014. Neptune at summer solstice: Zonal mean temperatures from ground-based observations, 2003–2007. *Icarus* 231, 146-167.

Fletcher, L. N., Drossart, P., Burgdorf, M., Orton, G. S., and Encrenaz, T., 2010. Neptune's Atmospheric Composition from AKARI Infrared Spectroscopy. *Astronomy and Astrophysics* 514, A17.

Fruchter, A. S., and Hook, R. N., 2002. Drizzle: A Method for the Linear Reconstruction of Undersampled Images. *The Publications of the Astronomical Society of the Pacific* 114, 144-152.

Gennaro, M., Anderson, J., Baggett, S., Bajaj, V., Brammer, G., Bourque, M., Calamida, A., Deustua, S., Dressel, L., Fowler, J., Khandrika, H., Khozurina-Platais, V., Kurtz, H., Long, K., Mack, J., Martlin, C., McCullough, P., McKay, M., Medina, J., de la Pena, M., Pirzkal, N., Russell, R., Sahu, K., Shanahan, C., Sosey, M., Riess, A., Sabbi, E., Stevenson, K., and Sunnquist, B., 2018. *WFC3 Data Handbook*, Version 4.0. STScI: Baltimore.

Goody, R. M., and Yung, Y. L., 1995. *Atmospheric Radiation: Theoretical Basis*, New York: Oxford University Press.

Gonzaga, S., and Biretta, J., 2010. *HST WFPC2 Data Handbook*, Version 5.0. STScI: Baltimore.

Hammel, H. B., Baines, K. H., and Bergstralh, J. T., 1989a. Vertical Aerosol Structure of Neptune: Constraints from Center-to-Limb Profiles. *Icarus* 80, 416-438.

Hammel, H. B., Beebe, R. F., De Jong, E. M., Hansen, C. J., Howell, C. D., Ingersoll, A. P., Johnson, T. V., Limaye, S. S., Magalhaes, J. A., Pollack, J. B., Sromovsky, L. A., Suomi, V. E., and Swift, C. E., 1989b. Neptune's Wind Speeds Obtained by Tracking Clouds in Voyager Images. *Science* 245, 1367-1369.

Hansen, J. E., and Pollack, J. B., 1970. Near-Infrared Light Scattering by Terrestrial clouds. *Journal of the Atmospheric Sciences* 27, 264-281.

Henyey, L. G., and Greenstein, J. L., 1941. Diffuse Radiation in the Galaxy. *The Astrophysical Journal* 93, 70-83.

Irvine, W. M., 1968. Multiple Scattering by Large Particles. II. Optically Thick Layers. *Astrophysical Journal* 152, 823-834.

Irwin, P. G. J., Fletcher, L. N., Tice, D., Owen, S. J., Orton, G. S., Teanby, N. A., Davis, G. R., 2016. Time variability of Neptune's horizontal and vertical cloud structure revealed by VLT/SINFONI and Gemini/NIFS from 2009 to 2013. *Icarus* 271, 418-437.

Karkoschka, E., 1994. Spectrophotometry of the Jovian Planets and Titan at 300- to 1000-nm Wavelength: The Methane Spectrum. *Icarus* 111, 174-192.

Karkoschka, E., 1998. Methane, Ammonia, and Temperature Measurements of the Jovian Planets and Titan from CCD-Spectrophotometry. *Icarus* 133, 134-146.

Karkoschka, E., 2011. Neptune's cloud and haze variations 1994–2008 from 500 HST–WFPC2 images. *Icarus* 215, 759-773.

Karkoschka, E., and Tomasko, M. G., 2010. Methane absorption coefficients for the jovian planets from laboratory, Huygens, and HST data. *Icarus* 205, 674-694.

Karkoschka, E., and Tomasko, M. G., 2011. The haze and methane distributions on Neptune from HST–STIS spectroscopy. *Icarus* 211, 780-797.

Karkoschka, E., and Tomasko, M. G., 2009. The haze and methane distributions on Uranus from HST–STIS spectroscopy. *Icarus* 202, 287–309.

Laidler, V., Boffi, F., Barlow, T., Brown, T., Friedman, S., Jester, S., Apellaniz, J. M., and Proffitt, C., 2008. *Synphot Data User's Guide*, Version 1.2. STScI: Baltimore.

Lockwood, G. W., and Thompson, D. T., 2002. Photometric variability of Neptune 1972–2000. *Icarus* 156, 37-51.

Lockwood, G. W., and Jerzykiewicz, M., 2006. Photometric variability of Uranus and Neptune 1950–2004. *Icarus* 180, 442–452.

Lockwood, G. W., 2019. Final Compilation of Photometry of Uranus and Neptune, 1972-2016. *Icarus* 324, 77-85.

Luszcz-Cook, S. H., de Kleer, K., de Pater, I., Adamkovics, M., and Hammel, H. B., 2016. Retrieving Neptune's aerosol properties from Keck OSIRIS observations. I. Dark regions. *Icarus* 276, 52-87.

McMaster, M., 2009. *The PHOTFLAM advisory*, memo on STScI website.

McMaster, M., and Biretta, J., 2008. *WFPC2 Instrument Handbook*, Version 10.0. Baltimore: STScI.

Mishchenko, M., Travis, L., and Laces, A., 2015. Scattering. In: *Encyclopedia of Atmospheric Sciences 2*, Elsevier.

Molter, E., de Pater, I., Luszcz-Cook, S., Hueso, R., Tollefson, J., Alvarez, C., Sánchez-Lavega, A., Wong, M., Hsu, A., Sromovsky, L. A., Fry, P. M., Delcroix, M., Campbell, R., de Kleer, K., Gates, E., Lynam, P. D., Ammons, S. M., Park Coy, B., Ducheneal, G., Gonzales, E. J., Hirscha, L., Magnier, E. A., Ragland, S., Rich, R. M., and Wang, F., 2019. Analysis of Neptune's 2017 Bright Equatorial Storm. *Icarus* 321, 324-345.

Newburn Jr., R. L., and Gulkis, S., 1973. A survey of the outer planets Jupiter, Saturn, Uranus, Neptune, Pluto, and their satellites. *Space Science Reviews*, Vol. 14(2), pp. 179–271.

Pryor, W. R., West, R. A., Simmons, K. E., and Delitsky, M., 1992. High-phase-angle observations of Neptune at 2650 and 7500 Å: Haze structure and particle properties. *Icarus* 99, 302-317.

Rybicki, G. B., and Lightman, A. P., 2004. *Radiative Processes in Astrophysics*. Weinheim: Wiley-VHC Verlag GmbH & Co.

Simon, A. A., Wong, M. H., and Hsu, A., 2019. Formation of a New Great Dark Spot on Neptune in 2018. *Geophysical Research Letters* 46, 3108–3113.

Smith, B. A., Soderblom, L. A., Banfield, D., Barnet, C., Basilevsky, A. T., Beebe, R. F., Bollinger, K., Boyce, J. M., Brahic, A., Briggs, G. A., Brown, R. H., Chyba, C., Collins, S. A., Colvin, T., Cook, A. F., Crisp, D., Croft, S. K., Cruikshank, D., Cuzzi, J. N., Danielson, G. E., Davies, M. E., De Jong, E., Dones, L., Godfrey, D., Goguen, J., Grenier, I., Haemmerle, V. R., Hammel, H., Hansen, C. J., Helfenstein, C. P., Howell, C., Hunt, G. E., Ingersoll, A. P., Johnson, T. V., Kargel, J., Kirk, R., Kuehn, D. I., Limaye, S., Masursky, H., McEwen, A., Morrison, D., Owen, T., Owen, W., Pollack, J. B., Porco, C. C., Rages, K., Rogers, P., Rudy, D., Sagan, C., Schwartz, J., Shoemaker, E. M., Showalter, M., Sicardy, B., Simonelli, D., Spencer, J., Sromovsky, L. A., Stoker, C., Strom, R. G., Suomi, V. E., Synott, S. P., Terrile, R. J., Thomas, P., Thompson, W. R., Verbiscer, A. and Veverka, J., 1989. Voyager 2 at Neptune: Imaging Science Results. *Science* 246, 1422-1449.

Sromovsky, L. A., 2005. Effects of Rayleigh-scattering polarization on reflected intensity: a fast and accurate approximation method for atmospheres with aerosols. *Icarus* 173, 284-294.

Sromovsky, L. A., Fry, P. M., Boudon, V., Campargue, A., and Nikitin, A., 2012. Comparison of line-by-line and band models of near-IR methane absorption applied to outer planet atmospheres. *Icarus* 218, 1–23.

Sromovsky, L. A., Fry, P. M., Limaye, S. S., Baines, K. H., and Dowling, T. E., 2001a. Coordinated 1996 HST and IRTF Imaging of Neptune and Triton: I. Observations, Navigation, and Differential Deconvolution. *Icarus* 149, 416-434.

Sromovsky, L. A., Fry, P. M., Limaye, S. S., Baines, K. H., and Dowling, T. E., 2001b. Coordinated 1996 HST and IRTF Imaging of Neptune and Triton: II. Implications of Disk-averaged Photometry. *Icarus* 149, 435-458.

Sromovsky, L. A., Fry, P. M., Limaye, S. S., Baines, K. H., and Dowling, T. E., 2001c. Coordinated 1996 HST and IRTF Imaging of Neptune and Triton: III. Neptune's Atmospheric Circulation and Cloud Structure. *Icarus* 149, 459-488.

Sromovsky, L. A., Fry, P. M., Dowling, T. E., Baines, K. H., and Limaye, S. S., 2001d. Neptune's Atmospheric Circulation and Cloud Morphology: Changes Revealed by 1998 HST Imaging. *Icarus* 150, 244-260.

Sromovsky, L. A., Fry, P. M., Limaye, S. S., and Baines, K. H., 2003. The nature of Neptune's increasing brightness: evidence for a seasonal response. *Icarus* 163, 256-261.

Stamnes, K., Tsay, S. C., Wiscombe, W., and Jayaweera, K., 1988. Numerically stable algorithm for discrete-ordinate-method radiative transfer in multiple scattering and emitting layered media. *Applied Optics* 27, 2502-2509.

Tollefson, J., de Pater, I., Luszcz-Cook, S., and de Boer, D., 2019. Neptune's Latitudinal Variations as Viewed with ALMA. In revision.

Wong, M. H., Tollefson J., Hsu, A. I., de Pater, I., Simon, A. A., Hueso, R., Sánchez-Lavega, A., Sromovsky, L. A., Fry, P., Luszcz-Cook, S., Hammel, H., Delcroix, M., de Kleer, K., Orton, G. S., and Baranec, C., 2018. A New Dark Vortex on Neptune. *The Astronomical Journal* 155, 117-125.

Yoder, C.F., 1995. Astrometric and geodetic properties of Earth and the Solar System. In *Global Earth Physics: A Handbook of Physical Constants*. AGU Reference Shelf 1, American Geophysical Union, pp. 1–31.